



저작자표시-비영리-변경금지 2.0 대한민국

이용자는 아래의 조건을 따르는 경우에 한하여 자유롭게

- 이 저작물을 복제, 배포, 전송, 전시, 공연 및 방송할 수 있습니다.

다음과 같은 조건을 따라야 합니다:



저작자표시. 귀하는 원 저작자를 표시하여야 합니다.



비영리. 귀하는 이 저작물을 영리 목적으로 이용할 수 없습니다.



변경금지. 귀하는 이 저작물을 개작, 변형 또는 가공할 수 없습니다.

- 귀하는, 이 저작물의 재이용이나 배포의 경우, 이 저작물에 적용된 이용허락조건을 명확하게 나타내어야 합니다.
- 저작권자로부터 별도의 허가를 받으면 이러한 조건들은 적용되지 않습니다.

저작권법에 따른 이용자의 권리와 책임은 위의 내용에 의하여 영향을 받지 않습니다.

이것은 [이용허락규약\(Legal Code\)](#)을 이해하기 쉽게 요약한 것입니다.

[Disclaimer](#)



Thesis for a Ph.D. Degree

**Cloud-longwave feedback processes
over the tropical and Arctic regions**

열대 및 북극 지역 구름의 장파복사 되먹임 작용

February 2020

**Computational Science and Technology
Graduate School
Seoul National University**

Heeje Cho

Cloud-longwave feedback processes over the tropical and Arctic regions

By
Heeje Cho

Dissertation Submitted to the Faculty of the Graduate School of
the Seoul National University in Partial Fulfillment of the
Requirement for the Degree of Doctor of Philosophy

Degree Awarded:
February 2020

Advisory committee:

Professor	Kwang-Yul Kim, Chair
Professor	Chang-Hoi Ho, Advisor
Professor	Jhoon Kim
Professor	Myung-Hwan Ahn
Professor	Yong-Sang Choi

Abstract

Clouds can strongly warm or cool the planet by regulating the radiations at top-of-atmosphere (TOA) and surface. The behavior of clouds in response to increasing anthropogenic forcing is crucial for understanding the characteristics of global warming. However, even the global mean response of clouds has not been decided observationally yet, but also varies greatly among numerical model simulations. This difficulty in quantifying “cloud feedback” occurs generally in observational estimations of the Earth’s radiative feedback. In the present dissertation, possible conditions for a successful feedback estimation are explored using simulations of an ideal energy balance model. As the climate feedback parameter is defined as the “response” of global mean TOA radiative flux to changes in global mean surface temperature in $\text{W m}^{-2} \text{ K}^{-1}$, the variations in TOA radiative flux are divided into the “signal” which is dependent on surface temperature, and the “noise” which is not. It is suggested that the a feedback estimation may be possible with a noise ratio smaller than 5% which is hardly be satisfied in a real ($>13\%$) or simulated (11–28%) climate. However, a linear analysis using satellite measurements of the TOA longwave radiation reveals that the tropical (20°S – 20°N) longwave feedback can be diagnosed from observations, and the estimated feedback parameter is $3.9 \text{ W m}^{-2} \text{ K}^{-1}$ indicating a strong thermal cooling effect of tropical clouds.

The result implies that feedbacks are more likely to be diagnosed in tropics due to the strong convective activities allowing enhanced surface effects to clouds, and also that the longwave radiation can have a larger feedback signal than the shortwave radiation because the radiative transfer of shortwave radiation is much more complicated due to its strong dependencies on latitude, local time, cloudiness, surface type, and so on. Accordingly, this dissertation examines two regional climates which likely to provide opportunities to improve the understanding of the longwave cloud feedback: (1) the Pacific warm pool region (20°N – 20°S , 130°E – 170°W) where clouds are known to be most sensitive to local sea-surface temperature changes, and (2) the winter season Arctic region which experiences polar night so that the cloud radiative effect can have only the longwave component.

The longwave cloud feedback over the Pacific warm pool area are examined using the outgoing longwave radiation (OLR) obtained from geostationary satellite observations because of the time resolution short enough to resolve processes associated with tropical convective clouds. A linear regression analysis with the domain-averaged OLR and SST anomalies shows that the regression slope can indicate a radiative feedback only with SST least-affected by cloud radiative forcing, for which SST needs to be obtained as daily average over cloud-free regions. The estimated value of the longwave feedback parameter is $15.72 \text{ W m}^{-2} \text{ K}^{-1}$, indicating the presence of strong longwave radiation in response to surface warming. This atmospheric

cooling effect is found to be primarily associated with reduced areal coverage of clouds ($-14.4\% \text{ K}^{-1}$).

Arctic Ocean has lost significant amount of sea-ice in past decades. This is possibly related to the recent increase in the Arctic winter season cloudiness. If so, it acts as a longwave cloud feedback to the Arctic surface thus exerts further surface warming. Modelling experiments are required for understating how the sea-ice change affect winter clouds, however, the accuracy of model clouds has not been sufficiently examined especially during Arctic winters experiencing polar nights. Accordingly, cloud simulations of the polar-optimized version of the Weather Research and Forecasting (Polar WRF) model are compared with retrievals from active sensor observations from satellites and radiation measurements from ground sites. Based on the accuracy information of modelled clouds, the model is used to investigate how the diminishing winter Arctic sea-ice affects the Arctic clouds. The control simulation was run for 10 winters from 2007/08 to 2016/17. Modelled responses of clouds are examined in the simulations with increased sea-ice concentrations according to the climatological difference to the period 1979/80 to 1988/89. By keeping the other boundary conditions and initial conditions the same with those of the control run, the effects of changes in atmospheric and oceanic circulations could be excluded. The experiment showed significant cloud responses in the areas that have lost winter sea-ice. Over the Barents Sea which has experienced more than 30% reduction of

winter sea-ice, the experiment revealed that the sea-ice reduction could result in 15% increase in the cloud water content and 10 W m^{-2} increase in the surface radiation. This implies that the sea-ice reduction is essential in understanding the winter Arctic cloud changes in the last few decades.

Keyword : Cloud, Climate Change, Longwave Radiation, Feedback

Student Number : 2005-30157

TABLE OF CONTENTS

ABSTRACT	1
LIST OF TABLES	6
LIST OF FIGURES	7
1. INTRODUCTION	13
2. DATA AND METHODOLOGY.....	20
2.1. Data.....	20
2.2. Methodology	22
3. CLOUD FEEDBACK ESTIMATIONS.....	31
3.1. Uncertainty in the observed estimates of radiative feedbacks	31
3.2. Longwave cloud feedback over the Pacific warm pool.....	54
4. LONGWAVE EFFECTS OF ARCTIC CLOUDS	67
4.1. Arctic winter clouds in Polar WRF simulations	67
4.2. Cloud responses to the recent Arctic sea-ice change	105
5. CONCLUDING REMARKS.....	117
REFERENCES	119
국문 초록	132

LIST OF TABLES

Table 1. The estimated $\sigma(F_{\text{non}})$ values for 11 CMIP climate models [From Choi et al. (2014)].

Table 2. The estimated $\sigma(F_{\text{rad}})/\sigma(F_{\text{non}})$ values associated with different choices for the bulk heat capacity of the Earth's climate system C_p , and feedback function λ . Globally averaged, the ocean-averaged, and the land-averaged ΔR values are used [From Choi et al. (2014)].

Table 3. The value \pm standard errors of $\Delta OLR_{\text{entire}}/\Delta SST_{\text{clear}}$ and $\Delta A_{\text{cloud}}/\Delta SST_{\text{clear}}$ from simple linear regression with different BT_{11} thresholds for clear-sky/cloudy pixel detection; all the anomaly values are daily means. The results from the reduced major axis method are shown in parentheses [From Cho et al. (2012)].

Table 4. Mean heights of cloud top in the DARDAR (raDAR/liDAR) cloud data (combined cloud retrievals using CloudSat and CALIPSO) and in the Polar WRF simulations. The values in parentheses denote the correlation coefficients between the DARDAR cloud heights and the modelled cloud heights. The Morrison scheme and the WSM6 scheme were used for the cloud microphysics in the simulations.

Table 5. Correlation coefficients and mean differences (simulation minus satellite retrieval) in the outgoing longwave radiation at the top-of-atmosphere (OLR) and downward longwave radiation at the surface (DLR) between the Polar WRF simulations and the CERES satellite dataset. The Morrison scheme and WSM6 were used for the cloud microphysics in the simulations.

LIST OF FIGURES

Figure 1. The lagged linear correlation coefficient (a) and regression slope (b) of ΔR versus ΔT_s for shortwave (blue) and longwave (red) radiation; The thick solid line indicates global data, and the thick dashed line indicates 20°S–20°N. Positive signs are used for upward fluxes.

Figure 2. The lagged linear correlation coefficient and regression slope of ΔR versus ΔT_s from the zero-dimensional energy balance model simulations. The blue shaded area indicates the range of the simulated values from 1,000 simulated realizations, and the red dashed line indicates their average. The assumed climate feedback $2.7 \text{ W m}^{-2} \text{ K}^{-1}$ is superimposed by the blue dashed line in the lagged slope graph. The thin solid lines are 30 randomly selected examples. The forcings are purely (a) radiative and (b) non-radiative, respectively [From Choi et al. (2014)].

Figure 3. Same as Fig. 2 but for coexisting radiative and non-radiative forcings with $\sigma(F_{\text{rad}})/\sigma(F_{\text{non}}) = 0.05$ (a), 0.14 (b), and 2.33 (c) [From Choi et al. (2014)].

Figure 4. The mean and standard deviation of the errors in estimated feedback parameter (λ) from 100 simulations of the energy balance model. The abscissa indicates the ratio, $\sigma(F_{\text{rad}})/\sigma(F_{\text{non}})$. The pre-described feedback parameter is $1.0 \text{ W m}^{-2} \text{ K}^{-1}$ (a), $3.3 \text{ W m}^{-2} \text{ K}^{-1}$ (b), and $6.0 \text{ W m}^{-2} \text{ K}^{-1}$ (c) [From Choi et al. (2014)].

Figure 5. The correlation coefficient (r) between estimated F_{rad} and F_{non} with respect to feedback parameter λ . from the CERES and SST observations (solid line for globally averaged ΔR_{TOA} , blue dotted

line for the ocean-averaged ΔR_{TOA} , red dotted line for the land-averaged ΔR_{TOA}), and from 11 CMIP climate models (plus marks) with the estimated values of λ by CO₂-doubling equilibrium experiments (IPCC, 2007) [From Choi et al. (2014)].

Figure 6. Same as Figure 5 but for $\sigma(F_{\text{rad}})$ (a) and $\sigma(F_{\text{rad}})/\sigma(F_{\text{non}})$ (b) not r . The ratio, $\sigma(F_{\text{rad}})/\sigma(F_{\text{non}})$ from observations is larger than 4 models, and smaller than 6 models [From Choi et al. (2014)].

Figure 7. Lagged linear correlations (a) and regression slopes (b) between OLR_{entire} and SST . Positive abscissa value indicates that SST leads OLR . SST s are averaged over the entire domain of analysis (thin solid), cloudy area (dashed), and clear-sky area (thick solid) [From Cho et al. (2012)].

Figure 8. Lagged linear correlations (a) and regression slopes (b) between $AREA_{\text{cloud}}$ and SST_{clear} . Positive abscissa value indicates that SST_{clear} leads $AREA_{\text{cloud}}$. SST_{clear} is averaged over the cloud-free area, and $AREA_{\text{cloud}}$ is relative cloud coverage [From Cho et al. (2012)].

Figure 9. Model domain used for the Polar WRF simulations. The domain consisted of 300×300 grid points with a 24-km horizontal resolution. Crosses indicate the locations of the ground sites used for radiation observations.

Figure 10. Mean vertical structures of the cloud amounts in the DARDAR cloud data (solid) and the collocated Polar-WRF simulations (dashed). Different definitions of the cloud amount were used. They were defined as 1 if cloud existed in a WRF grid (a), or as the ratio of cloudy pixels within a collocated WRF grid

for the DARDAR, and the “cloud fraction” value provided by the model output (b). Black dashed lines represent the Polar WRF simulations with the Morrison scheme and red dashed lines for the WSM6 scheme.

Figure 11. Mean vertical structures of the ice water content in the DARDAR cloud data (solid) and the cloud water content for each hydrometeor in the collocated Polar-WRF simulations (dashed). The Morrison scheme (a) and the WSM6 scheme (b) were used for the cloud microphysics in the Polar-WRF simulations.

Figure 12. Cloud water content of snow (a), ice (b), liquid (c), and for all hydrometeors (d) from the Polar WRF simulation with the Morrison scheme, and the ice water content from the DARDAR cloud data (e) along an A-train track around 10 UTC, December 25, 2015. The color scale is the log₁₀ of the cloud water content.

Figure 13. Same as Figure 12 but for the WSM6.

Figure 14. Number of points for each thermodynamic phase of clouds (liquid- or rain-phase: red, frozen-phase: blue, and mixed-phase: black). The dataset is binned into the air temperature intervals of 2 °C. The numbers are counted for each WRF horizontal grids and are scaled to correspond to the 60-m height resolution of the DARDAR retrievals.

Figure 15. Joint probability density function (PDF) of the CloudSat radar reflectivity and height (a). Polar WRF simulations with the Morrison scheme (b) and the WSM6 scheme (c) were converted to “satellite-like” radar reflectivity using the COSP package to obtain the joint PDF. The color scale is the log₁₀ of the joint PDF.

Figure 16. Joint PDF of the CALIPSO lidar scattering ratio and height

(a). Polar WRF simulations with the Morrison scheme (b) and the WSM6 scheme (c) were converted to “satellite-like” lidar scattering radio using the COSP package to obtain the joint PDF. The color scale is the \log_{10} of the joint PDF.

Figure 17. The mean vertical structures of water contents of liquid (red), ice (blue), and snow (black) clouds with the Morrison scheme (a, b, and c) and WSM6 scheme (d, e, and f) at 1 hour and 6 hours Polar WRF model integrations initialized at 00 UTC, 24 December 2015. The areas with latitudes higher than 70° N were used, and divided into land surface (a, d), open water (b, e), and sea-ice area (c, f).

Figure 18. The mean vertical structures of major cloud microphysics process rate terms at 1 hour and 6 hours Polar WRF model integrations initialized at 00 UTC, 24 December 2015 when the Morrison scheme (a, b, and c) and WSM6 scheme (d, e, and f) are used. All the other terms not listed in the legend are plotted in gray lines. The areas with latitudes higher than 70° N were used, and divided into land surface (a, d), open water (b, e), and sea-ice area (c, f).

Figure 19. Time series of the daily mean surface evaporation (black), precipitation (red), and precipitable water (blue) from the Polar WRF simulations. The Morrison scheme (marked thin lines) and the WSM6 scheme (thick lines) were used for the cloud microphysics in the simulations. The values were obtained by averaging over the entire simulation domain.

Figure 20. Mean outgoing longwave radiation at the top-of-atmosphere (OLR) from the CERES observations (a), and the mean differences

in the OLR between the Polar WRF simulations and the CERES observation. The Morrison scheme (b) and the WSM6 scheme (c) were used for the cloud microphysics in the simulations.

Figure 21. Mean downward longwave radiation (DLR) at the surface from the CERES dataset (a), and the mean differences in the OLR between the Polar WRF simulations and the CERES dataset. The Morrison scheme (b) and the WSM6 scheme (c) were used for the cloud microphysics in the simulations.

Figure 22. Time series of the daily mean OLR (black) and DLR (red) from the CERES dataset (thick solid lines), and the Polar WRF simulations with the Morrison scheme (dashed lines) and the WSM6 scheme (thin solid lines). Only values of the Polar WRF at nadir points of the CERES satellite were used.

Figure 23. Daily mean time series of the observed DLR (gray) at six BSRN stations: Tiksi (a), Cape Baranova (b), Ny-Ålesund (c), Barrow (d), Lerwick (e), and Tõravere (f); and the simulated DLR with the Morrison scheme (red) and the WSM6 scheme (blue) at the grid where each station was located.

Figure 24. Mean sea-ice concentration during ten winters (December to February) for the period from 2007/08 to 2016/17 (blue shades) and the climatological difference to the period 1979/80 to 1988/89 (contours).

Figure 25. Differences in winter mean cloud water path between the periods 1979/80–1988/89 and 2007/08–2016/17 in ERA5 reanalysis (a), and between control run and “hice ice” run in the Polar WRF’s winter simulations (b). Green contour denotes the area

that mean sea-ice amount difference is larger than 30% over the Barents Sea.

Figure 26. Same as Figure 25 but for the differences in cloud longwave effect at surface.

Figure 27. Histograms of column-integrated cloud water path over the Barents sea for the control simulations (black lines) and the high-ice runs (blue lines), when the surface pressure is smaller than 990 hPa (a) and larger than 1025 hPa (b).

Figure 28. Histograms of column-integrated cloud water path over the Barents sea in ERA5 reanalysis for the period 1979/80–1988/89 (blue lines) and 2007/08–2016/17 (black lines), when the surface pressure is smaller than 990 hPa (a) and larger than 1025 hPa (b).

1. Introduction

Clouds are an important radiative element in determining the energy balance of the Earth. Usually, their mass is about two orders of magnitudes smaller than that of atmospheric water vapor. However, their radiative effects at the top-of-atmosphere (TOA) or the surface frequently surpass those of atmospheric water vapors (Boucher et al., 2014). While the atmospheric water vapor is a powerful greenhouse gas, its radiative response to a climatic forcing is somewhat predictable in the future climate projections since the strength of combined water vapor and lapse rate feedbacks showed little spread in the current climate model experiments (Colman, 2003). On the other hand, large discrepancies in the cloud feedback effects are found among the models. For carbon dioxide doubling experiments, the simulated response of the global mean cloud radiative effect differs greatly among models. The diversity is partly due to different mean temperature field and to different radiative transfer calculation in the models, nonetheless, it is caused mainly by cloud simulation uncertainty itself.

The generation and growth of cloud particles are highly sensitive to dynamical and thermodynamical conditions of the atmosphere in both nature and model simulation. Clouds are associated with various weather phenomena such as fronts, convective systems, topographic lee waves, etc. For them to form and dissipate, physical factors such as condensation aerosols,

ambient humidity, etc. are very influential too. Consequently, different dynamics/thermodynamics fields in the modelled climate simply lead to different cloud fields. In addition, the cloud microphysics scheme which governs this cloud processes varies from model to model.

Geographically, uncertain feedbacks over the tropical oceans are particularly important because of its global-scale impact (Roe et al., 2015). About half of the inter-model spread of the global climate feedback can be explained by the difference in the tropical convective mixing process which directly affects simulations of tropical low tropospheric clouds (Sherwood et al., 2014). Also, the simulation of the mid-latitude storm track and accompanying clouds is still a challenging problem while its location, strength, and variability are known to vary greatly with modelling setup (Bony et al., 2015). Over the Arctic region, as modelling uncertainties of cloud and its local radiative impact are significantly larger than other regions, the way Arctic clouds interact with underlying sea-ice remains an open question.

Because not only are the microphysical processes of clouds very complicated, but they also occur in short time scales, it has been difficult to obtain a process-based observational dataset which is required for narrowing the cloud modelling uncertainties. Therefore, numerical representations of cloud processes have been often evaluated with indirect measures such as surface rain measurements or satellite-retrieved cloud amounts. Relevant

information can also be obtained from radiative flux observations because clouds can have the largest effect on the temporal and spatial variabilities of TOA radiations than any other physical element because a surface-to-tropopause lapse rate easily exceeds the equator-to-pole temperature gradient.

A climate feedback is an intensifying or dampening of a radiative forcing by adjustments of climate elements. Conventionally, the global feedback strength of a climate, either real or simulated one, is defined as the “response” of global mean TOA radiative flux to changes in global mean surface temperature in $\text{W m}^{-2} \text{ K}^{-1}$. The cloud feedback strength, accordingly, is the cloud radiative flux response at TOA to a unit change in surface temperature. Hence, while clouds depend on many factors other than the surface temperature, only the dependence on surface temperature is directly relevant to cloud feedback.

However, it is argued that a reliable flux observation does not necessarily lead to an accurate feedback diagnosis (Lindzen and Choi, 2009, 2011; Spencer and Braswell, 2008). As this difficulty should be applied generally to observed estimates of the global feedback strength under global warming, the question of how much the earth’s surface temperature is sensitive to an anthropogenic forcing is still hotly debated (Dessler et al., 2018; Gregory et al., 2016; Lewis and Curry, 2015).

The longwave feedback of the earth can be separately defined because it involves only the terrestrial thermal outgoing radiation at TOA while the

shortwave feedback is related to the reflection of solar radiation. A determination of the shortwave component of radiative flux is complicated due to its strong dependencies on latitude, local time, cloudiness, surface type, and so on. In comparison, longwave radiations are simpler in a radiative transfer because its behavior at earth or cloud surfaces can be well approximated under a gray-body assumption. As a result, the ratio of “noise” to the observed radiative feedback “signal” tends to be significantly smaller for the longwave feedback than the shortwave feedback.

A signal-to-noise ratio in estimating a radiative feedback strength is also related to the regional climate. In particular, tropical feedbacks can exhibit stronger feedback signals in the relationship between TOA flux and surface temperature than the other regions. The warm sea-surface temperature and the moist atmosphere increase the convective available potential energy which allows a stronger dependence of TOA radiation on surface temperature. Further, the weaker vertical wind shear and larger Rossby radius of deformation strengthen vertical convective activities so that a surface forcing’s effect on the regional TOA radiation can be stronger. This can provide an invaluable opportunity for a “physics-oriented” but not stochastic estimation of the earth’s feedback strength. Moreover, it might have implications for the global climate feedback strength because uncertainties in tropical feedback can significantly alter the global surface temperature response to a climatic forcing.

Another opportunity for an assessment of the cloud feedback can be provided for the Arctic atmosphere during the winter seasons. Outside the tropics, while regional TOA flux variations can be correlated with temperature variations of the underlying surface, they tend to act as a forcing not a response to the surface. Also, horizontal advects of atmospheric heat or water vapor may reduce the influence of surface temperature to local TOA flux. Thus, one must be cautious when inferring regional feedbacks by analyzing TOA flux and surface temperature because their relationship hardly represents radiative feedbacks. Despite all these limitations, the polar night conditions of the Arctic winters can provide a unique environment inhibiting most of radiative effects related to the sunlight. Therefore, the radiative processes are significant only at thermal wavelengths so that the radiative transfer both at TOA and surface is much simpler than it would be in any other climate condition.

Meanwhile, the recent decline in the Arctic sea-ice cover has acted as a surface forcing to the atmosphere strong enough to influence clouds. The increased extent of open water resulted in enhanced surface turbulent fluxes of sensible and latent heats to the atmosphere in favor of increased cloudiness. Many advantages can be offered by using the winter sea-ice decrease as a forcing agent. First, as the forcing is exerted from the surface, any changes in clouds and radiative fluxes should contain components that are originated from the surface forcing thus indicate atmospheric feedback signals. Next,

during polar nights, there are little shortwave cooling effects by clouds offsetting the warming responses by the atmospheric water vapor and cloud. Also, due to the large thermal inertia of ice, variations in the forcing may operate on time scales long enough for the responses in the cloud and atmosphere to be examined.

Despite these advantages, it is difficult to separate the cloud changes originated from the sea-ice decrease in observational datasets because Arctic clouds could have been influenced by long-term changes in heat and moisture transports from lower latitudes. Numerical experiments using climate model simulations with modified sea-ice can be useful to investigate the Earth's responses to a specified sea-ice change. However, the reliability of simulated responses can be limited to the uncertainty of global climate models. The macro- and microphysical properties of clouds are highly sensitive to mean climate which differs greatly among models especially in high-latitudes, so that the differences in the surface cloud forcing between models can be larger than 15 W m^{-2} (Karlsson and Svensson, 2013). Alternatively, instead of global models, more realistic climatologies of atmospheric variables can be obtained by using regional mesoscale models. This is because, unlike global models, a regional model's simulation is constrained by lateral boundary conditions by which one can control the momentum and heat fluxes from lower latitudes.

The objective of the present dissertation is to improve the knowledge of clouds' roles in the recent climate changes. In particular, responses of clouds

and their thermal radiative effects to surface forcings are analyzed for two representative cases based on the possible opportunities addressed above. In Section 3, methodological aspects of feedback estimations with radiative flux data are explored using an ideal box model to explain why the estimations are necessarily inaccurate when data for the warming climate period is used. Based on this understanding, the longwave radiative effects of clouds over the Pacific warm pool area (PWP; 20°N–20°S, 130°E–170°W) are examined using observations from a geostationary satellite allowing high temporal resolution. In Section 4, in order to assess the usefulness of mesoscale model for Arctic cloud studies, the polar-optimized version of the Weather Research and Forecasting (Polar WRF) model is tested by comparing the simulated clouds with satellite retrievals. Next, based on the accuracy information of modelled clouds, modelled cloud responses to the increased sea-ice concentration are examined. The datasets and methods used in this dissertation are described in the next section, and concluding remarks are provided in Section 5.

2. Data and methodology

2.1. Data

2.1.1. Satellite data

The radiation flux observations from the Clouds and the Earth's Radiant Energy System instruments (CERES; Wielicki et al., 1996) were used in the present dissertation. For the radiative feedback estimations, the level-3 Energy Balanced and Filled (EBAF) Edition 4.1 from March 2000 to June 2019 were used. The time and spatial resolutions are monthly and 1° , respectively. For the evaluation of the Polar WRF simulations, the level-2 Single Scanner Footprint (SSF) product from Aqua satellite (Edition 4A) from 1 December 2015 to 29 February 2016 were used. This product offers not only direct measurements of the TOA longwave flux, but also estimates of the surface longwave flux produced using radiative transfer calculations. The surface flux is parameterized based on a priori information on cloud base heights and atmospheric profiles of air temperature, humidity, and ozone (Kratz et al., 2010). The mean bias and root-mean-square error of the CERES surface longwave flux to the ground observations was about -0.5 and 10.3 W m^{-2} , respectively (https://ceres.larc.nasa.gov/science_information.php?page=computed-fluxes). Note that the CERES footprints are 25 km in diameter near nadir. DARDAR (raDAR/liDAR) cloud products (Delanoë and Hogan, 2008,

2010) are derived from the combined observations from two satellite-borne active instruments, namely, the Cloud Profiling Radar (CPR) onboard the CloudSat satellite (Stephens et al., 2002) and the Cloud-Aerosol Lidar with Orthogonal Polarization (CALIOP) onboard the Cloud-Aerosol Lidar and Infrared Pathfinder Satellite Observations (CALIPSO) satellite (Winker et al., 2009). From DARDAR, a 3-D cloud mask and ice water contents were used that are produced for the same horizontal (about 1 km) and vertical (60 m) resolutions with the CloudSat observations. The data period used are from 1 December 2015 to 29 February 2016.

The window channel (centered at \sim 11 μm) observations from Japanese Multi-functional Transport Satellite (MTSAT-1R) on the geostationary orbit centered at 140°E. were used to produce cloud amounts and OLRs over the PWP area. The data period used is 1 January 2008 to 30 June 2010. The horizontal resolution is about $4 \times 4 \text{ km}^2$ at nadir.

2.1.2. Reanalysis data

The National Oceanic and Atmospheric Administration's 0.25° daily optimum interpolation SST version 2, using satellite observations from the Advanced Microwave Scanning Radiometer and Advanced Very High Resolution Radiometer (Reynolds et al., 2007) were used for feedback estimations.

The Polar WRF simulations were initialized and laterally updated using the

National Center for Environmental Prediction (NCEP) Final Operational Global Analysis data (NCEP, 2000) and the NCEP Real-Time Global Sea Surface Temperature data (Thiébaux et al., 2003)

2.1.3. Surface longwave flux observations

Direct measurements of the downward longwave radiative flux at six Arctic and high-latitudinal ground sites were available within the Baseline Surface Radiation Network (BSRN) dataset (Driemel et al., 2018), namely, Cape Baranova, Russia (79.27°N , 101.75°E), Ny-Ålesund, Norway (78.93°N , 11.93°E), Tiksi, Russia (71.59°N , 128.92°E), Barrow, United States of America (71.32°N , 156.61°W), Lerwick, United Kingdom, (60.14°N , 1.18°W), and Tõravere, Estonia (58.25°N , 26.46°E). They were used for comparison with the Polar WRF simulations from 1 December 2015 to 29 February 2016, except for Cape Baranova observations which have only been available since 1 January 2016.

2.2. Methodology

2.2.1. Idealized energy balance model

The idealized energy balance model in Eq. 1 assumes a hypothetical climate system with uniform temperature and heat capacity (Lin et al., 2011; Manabe et al., 1990; Schwartz, 2007; Spencer and Braswell, 2010).

$$C_p \left[\frac{d\Delta T_s}{dt} \right] = F_{\text{non}}(t) + F_{\text{rad}}(t) - \lambda \cdot \Delta T_s(t) \quad (1)$$

where ΔT_s is the global surface temperature anomalies, ΔR is the flux anomalies of global net radiation (sum of shortwave and longwave radiation flux anomalies), C_p is the constant bulk heat capacity of the system, and λ is the parameter indicating the feedback strength. C_p determines the overall variance of surface temperature in response to a given amount of forcing and feedback. Here C_p was set to 14 year $\text{W m}^{-2} \text{K}^{-1}$ equivalent to 110 m of ocean water corresponding roughly to the ocean mixed layer (Schwartz, 2007). Following Spencer and Braswell (2010) and Lindzen and Choi (2011), forcings in Eq. 1 are divided into two terms: radiative (F_{rad}) and non-radiative (F_{non}) forcings. F_{rad} can be due for example to cloud variations, while F_{non} may be due for example to stochastic component of heat transfer from ocean below the mixed layer. The increasing radiative forcing such as due to increasing CO₂ that is known to cause another problems in estimating climate feedback (Spencer and Braswell, 2010), therefore, it is not considered. Two forcing terms (F_{rad} and F_{non}) are 9-month low pass filtered series of monthly normally distributed random numbers with nearly zero mean, to mimic the time scales of variations seen in the climate models and observations (Spencer and Braswell, 2011). F_{rad} may partly include forcings by cloud variations that are dynamically driven by F_{non} . Even in that case where F_{rad} and F_{non} are strongly correlated, F_{rad} remains to act as a noise source unless the cloud

variations are involved in λ . $\lambda\Delta T_s$ represents radiative feedback effect. λ must have a positive value; otherwise the system is unstable. The larger λ is, the faster the system is restored to equilibrium. Let λ_0 be the Planck response of $3.3 \text{ W m}^{-2} \text{ K}^{-1}$, and then λ values larger (smaller) than λ_0 indicate negative (positive) feedbacks. In order to show that climate feedback can easily be estimated as being positive despite the true feedback being negative, it is assumed that the idealized system to have (negative) climate feedback $2.7 \text{ W m}^{-2} \text{ K}^{-1}$, so λ in Eq. 1 is set to 6 ($=2.7 + 3.3$) $\text{W m}^{-2} \text{ K}^{-1}$.

2.2.2. Retrieval algorithm for outgoing longwave radiation from the geostationary satellite

OLR values on a pixel basis of the MTSAT-1R dataset are obtained as a third-order polynomial function of 11- μm radiance (L_{11} ; Eq. 2):

$$OLR = 44.95 + 50.97 L_{11} - 4.02 L_{11}^2 + 0.15 L_{11}^3, \quad (2)$$

where the four constant coefficients of the polynomial function in Eq. 2 are obtained by a regression least-square fit of OLRs against L_{11} simulated by a radiative transfer model with various environmental conditions; each of the 840 simulations incorporates every combination of 7 satellite zenith angles (0° – 60° , 10° interval), 8 cloud top heights (2–16 km, 2 km interval), and 15 cloud optical thicknesses (20–48, 2 interval). For the radiative transfer simulations, the discrete ordinates radiative transfer (DISORT) model “Santa Barbara DISORT Atmospheric Radiative Transfer” (SBDART; Ricchiazzi et

al., 1998) is used. The root-mean-square difference between L_{11} -inferred OLRs and OLRs measured directly from broadband satellite instruments is known to be less than approximately 10 W m^{-2} (Ba et al., 2003; Ohring et al., 1984). The bias of L_{11} -inferred OLR may stem largely from water vapor because L_{11} does not involve absorption by water vapor, but by cloud particles and surface. Therefore, it should be noted that the OLR only represents longwave variations induced by cloud and surface properties by excluding the other infra-red channels of MTSAT-1R in OLR calculations. Other biases due to instrumentation factors, algorithms, etc. are also relevant for estimation of feedback, and they may eventually reduce the statistical significance of the regression (e.g., coefficient of determination: R^2). In many previous studies, R^2 between SST and OLR was found to be very low in monthly-observed data.

2.2.3. Retrieval algorithm for clear-sky OLR and SST

A single-channel threshold test using $11\text{-}\mu\text{m}$ channel-brightness temperature (BT_{11}) is employed to determine the presence of cloud at each pixel in the MTSAT-1R data. As most opaque clouds represented in the longwave radiation can be distinguished by this BT_{11} test (e.g., Choi et al., 2005; Horváth and Soden, 2008; Rossow and Garder, 1993), many previous cloud studies using geostationary observations have employed the single-channel test for identification of cloudy pixels. Various threshold values for BT_{11} were tested but the major conclusion in this study was found to be robust

and remained unchanged, regardless of the threshold values within a certain range.

Daily SST and OLR time series were generated that are area-averaged over the PWP, but for selective cases of cloud conditions. The detailed methodology for generating the time series is given by Eqs. 3a to 5c:

$$A_{cloud}^{hour}(i) = \frac{\sum_{m \in \text{cloudy} \cap \{i\}} \cos^{-1} \theta_m}{\sum_m \cos^{-1} \theta_m} \quad (3a)$$

$$A_{cloud}^{day}(i) = \sum_{hour=0}^{23} \frac{A_{cloud}^{hour}(i)}{24} \quad (3b)$$

$$\overline{SST}_{entire}^{day} = \sum_i^{PWP} SST^{day}(i) \cdot \cos \phi_i \Bigg/ \sum_i^{PWP} \cos \phi_i \quad (4a)$$

$$\overline{SST}_{cloud}^{day} = \sum_i^{PWP} SST^{day}(i) A_{cloud}^{day}(i) \cdot \cos \phi_i \Bigg/ \sum_i^{PWP} A_{cloud}^{day}(i) \cdot \cos \phi_i \quad (4b)$$

$$\overline{SST}_{clear}^{day} = \sum_i^{PWP} SST^{day}(i) \cdot A_{clear}^{day}(i) \cdot \cos \phi_i \Bigg/ \sum_i^{PWP} A_{clear}^{day}(i) \cdot \cos \phi_i \quad (4c)$$

$$\overline{OLR}_{entire}^{day} = \frac{1}{24} \cdot \sum_{hour=0}^{23} \left\{ \sum_m^{PWP} OLR^{hour}(m) \cdot \cos^{-1} \theta_m \Bigg/ \sum_m^{PWP} \cos^{-1} \theta_m \right\} \quad (5a)$$

$$\overline{OLR}_{cloud}^{day} = \frac{1}{24} \cdot \sum_{hour=0}^{23} \left\{ \sum_{m \in \text{cloudy} \cap \{PWP\}}^{PWP} OLR^{hour}(m) \cdot \cos^{-1} \theta_m \Bigg/ \sum_{m \in \text{cloudy} \cap \{PWP\}} \cos^{-1} \theta_m \right\} \quad (5b)$$

$$\overline{OLR}_{clear}^{day} = \frac{1}{24} \cdot \sum_{hour=0}^{23} \left\{ \sum_m^{clear \cap PWP} OLR^{hour}(m) \cdot \cos^{-1} \theta_m \left/ \sum_m^{clear \cap PWP} \cos^{-1} \theta_m \right. \right\}$$

(5c)

where i indicates the i -th SST grid; m the m -th MTSAT-1R pixel (with spatial resolution of $\sim 4 \times 4 \text{ km}^2$ at nadir); θ the satellite zenith angle; ϕ the latitude; \cap the intersection of two sets. As $\cos^{-1} \theta$ is proportional to the size of MTSAT-1R pixel, an hourly cloud fraction of each i -th 0.25° SST grid

$A_{cloud}^{hour}(i)$ was calculated via Eq. 3a, using cloudy pixels within the grid. A daily

cloud fraction of each SST grid, $A_{cloud}^{day}(i)$ is calculated by simple time averages (Eq. 3b). Note that in the results, different threshold values were used for ‘cloudy’ pixel detection ($BT_{11} < 270 \text{ K}$) and ‘clear’ pixel detection

($BT_{11} \geq 280 \text{ K}$), so that $A_{cloud}^{day}(i) + A_{clear}^{day}(i) < 1$. Over the PWP, BT_{11} values between 270 K and 280 K are generally regarded as the cloudy-sky signal, but the range can be avoided to eliminate ambiguity of cloud masking. During

the study period, $A_{cloud}^{day}(i)$ varies between 5% and 35% (standard deviation

4.9%), and $A_{clear}^{day}(i)$ varies between 41% and 86% (standard deviation 7.7%).

The daily SST and OLR time series are then calculated by Eqs. 4 and 5, respectively. $\overline{SST}_{entire}^{day}$ is the daily average of SSTs in the PWP (Eq. 4a), while $\overline{SST}_{cloud}^{day}$ is the cloud-weighted average of SSTs in the PWP (Eq. 4b). The weighting factors in Eqs. 3b and 3c are proportional to the daily cloud and

clear coverage, respectively. For instance, in Eq. 3b, the weighting factor would be 1 for a grid where all pixels are overcast in a day, and 0.5 where half the pixels are overcast in a day. Calculation of $\overline{SST}_{\text{clear}}^{\text{day}}$ values follows the consistent rule (Eq. 4c). Cosine values are multiplied with due consideration of the size of each MTSAT-1R pixel or SST grid. As the temporal resolution of SST data is lower than that of MTSAT-1R OLR, temporal degradation of OLR is also unavoidable in order to compare with SST data; daily OLR values are averaged from 00:00 UTC to 23:00 UTC (Eq. 5).

To remove low-frequency variations whose timescales are considered to be longer than that of tropical cloud processes, the daily $\overline{OLR}_x^{\text{day}}$ and $\overline{SST}_x^{\text{day}}$ ($x = \text{entire, cloud, or clear}$) anomalies (ΔOLR_x and ΔSST_x) are calculated by subtracting their moving average values with a 90-day centered smoother, which effectively isolates short timescale fluctuations (e.g., Zhang et al., 1995). The smoother also filters out the annual-cycle climatology, which is difficult to obtain from data series of less than three years. 90-day is the longest length to remove seasonality and not to remove meaningful 1–3 month fluctuations, which may be associated with the relevant dynamics. At least, to the filter length of 30–90 days, the main conclusions are almost insensitive. Note that extraction of $\Delta SST_{\text{clear}}$ is allowed only using hourly clear-sky detection from geostationary satellites, such as the MTSAT-1R data used in this study.

2.2.4. Polar WRF simulations

The Polar WRF version 3.7.1 (Skamarock et al., 2008) applying a polar stereographic projection with the center at the North Pole was used with 30 vertical terrain-following sigma levels from the earth's surface to 50 hPa. The vertical resolution is ~50 m near the surface, increasing to ~500 m at 3 km height, and to ~1 km near the tropopause. A domain of 300×300 grids with a 24-km resolution encompassed the area with latitudes higher than 56.5° North. Successive 48-hour simulations were performed beginning at 00 UTC every day from 1 December to 1 March next year. With a series of 2-day simulations, outputs except for the initial 24-hour spin-up segments were used for the analysis following Wilson et al. (2012), and Hines and Bromwich (2017). The domain average times series of precipitation, precipitable water, and radiative fluxes were examined to make sure that the 24-hour spin-up is long enough for the model to reach a stable state.

In order to assess the importance of varying processes on the Arctic clouds, two cloud microphysics schemes that are widely used in Arctic applications, namely the Morrison double moment scheme (Morrison et al., 2005) and the WRF single-moment 6-class scheme (Hong and Lim, 2006), were tested. The choice of other physics schemes in the WRF simulations were as follows: rapid radiative transfer model for the longwave radiative transfer (Mlawer et al., 1997), Goddard shortwave scheme for the shortwave radiative transfer

(Chou et al., 1998), Mellor–Yamada–Janjić scheme for the planetary boundary layer (Janjić, 1994), Unified Noah model for land surfaces (Tewari et al., 2004), Grell–Devenyi ensemble scheme for cumulus parameterizations (Grell and Devenyi, 2002), and the Eta similarity scheme for the surface layer (Janjić, 1994).

In order to simulate winter Arctic cloud responses to the recent sea-ice reduction, the control experiment was run for the ten winters (December to February) for the period from 2007/08 to 2016/17 initialized everyday at 00 UTC. The simulations were run for 48 hours and the initial 24-hour outputs were discarded for spin-up. The “high-ice” run is identical with the control run except for the increased sea-ice concentrations according to the climatological difference to the period 1979/80 to 1988/89. The Morrison double moment scheme was used for the cloud microphysics.

3. Cloud feedback estimations

In this section, possible uncertainties in the observed estimations of the Earth's radiative feedback strength is investigated especially when the time series of TOA radiative flux observations from satellites. While the global radiative feedback is uncertain, it is suggested that the longwave feedback of the tropics can have a cooling effect on the warming climate.

3.1. Uncertainty in the observed estimates of radiative feedbacks

Recent studies have attempted to determine climate feedback from satellite retrievals (Forster and Gregory, 2006; Lindzen and Choi, 2009, 2011; Spencer and Braswell, 2010, 2011). The previous results, however, have shown acute contradiction between the likelihood of positive and negative climate feedbacks. High total positive climate feedback brings in fundamentally more uncertainties in climate sensitivity than negative climate feedback does (Lindzen and Choi 2011; Roe and Baker, 2007). Thus, currently, the huge error range of the estimated magnitude of high climate sensitivity includes all of the values found in current climate models that represent total positive climate feedback (Colman, 2003; Knutti and Hegerl, 2008; Soden and Held, 2006).

Climate feedback processes essentially yield the change in outgoing radiation flux in response to the change in global surface temperature through the changes of cloud, water vapor, etc. Thus the recent observational feedback studies were based mostly on simple linear regression between global surface temperature anomalies (ΔT_s) and the flux anomalies of global net radiation (ΔR ; sum of shortwave and longwave radiation flux anomalies). The basis of examining the relation between ΔR and ΔT_s to estimate a feedback strength is that radiative flux is controlled by temperature over a given time in feedback. Most theoretical and empirical experiments showed that the exact value of feedback appears as the regression slope $\Delta R/\Delta T_s$ at zero time-lag, when the feedback between the two variables dominates over the system (Frankignoul, 1999; Frankignoul et al., 1998). More importantly, this should be followed by significant correlation at zero lag. The total climate feedbacks estimated by this way were usually positive.

However, recent observations show that correlation between ΔR and ΔT_s at zero lag is very weak, and moreover is often located between the opposite signs at negative and positive month lags (Lindzen and Choi, 2011). The weak correlation between the two variables implied that in observations many unknown radiative processes that are not feedbacks to SST (e.g., random cloud variations) exist, and that they strongly confuse the feedback strength in the ΔR - ΔT_s relation. This may also be the case of feedbacks taking several weeks to fully develop; e.g., cirrus detrainment from tropical cumulonimbus.

However, as assumed in most of previous feedback studies, this study rules out such a delayed feedback process. This naturally casts a question about reliability of the feedback estimates from the zero lag simple regression of observational time series.

3.1.1. Definition of the non-feedback variations

In order to resolve the problems associated with the simple regression method, improved methods have been suggested by Lindzen and Choi (2009, 2011) and Spencer and Braswell (2010). All these studies have argued the likelihood of negative feedback, by applying different methods that may better isolate the feedbacks from the effects of continuous equilibration or long-term (i.e., several decades) trend. Lindzen and Choi (2009, 2011) used short (few-month) segments in which the increase (or decrease) in ΔR and ΔT_s occurred. Spencer and Braswell (2010) tracked sequential ΔR and ΔT_s , and found feedback processes are presented by thin stripes in the ΔR - ΔT_s chart. Both methods aim to isolate feedbacks from the confounding factors of equilibration or long-term trend more appropriately than does the simple regression of the whole observed time series. However, these alternatives have also been subject to criticism (Chung et al., 2010; Murphy, 2010; Trenberth et al., 2010).

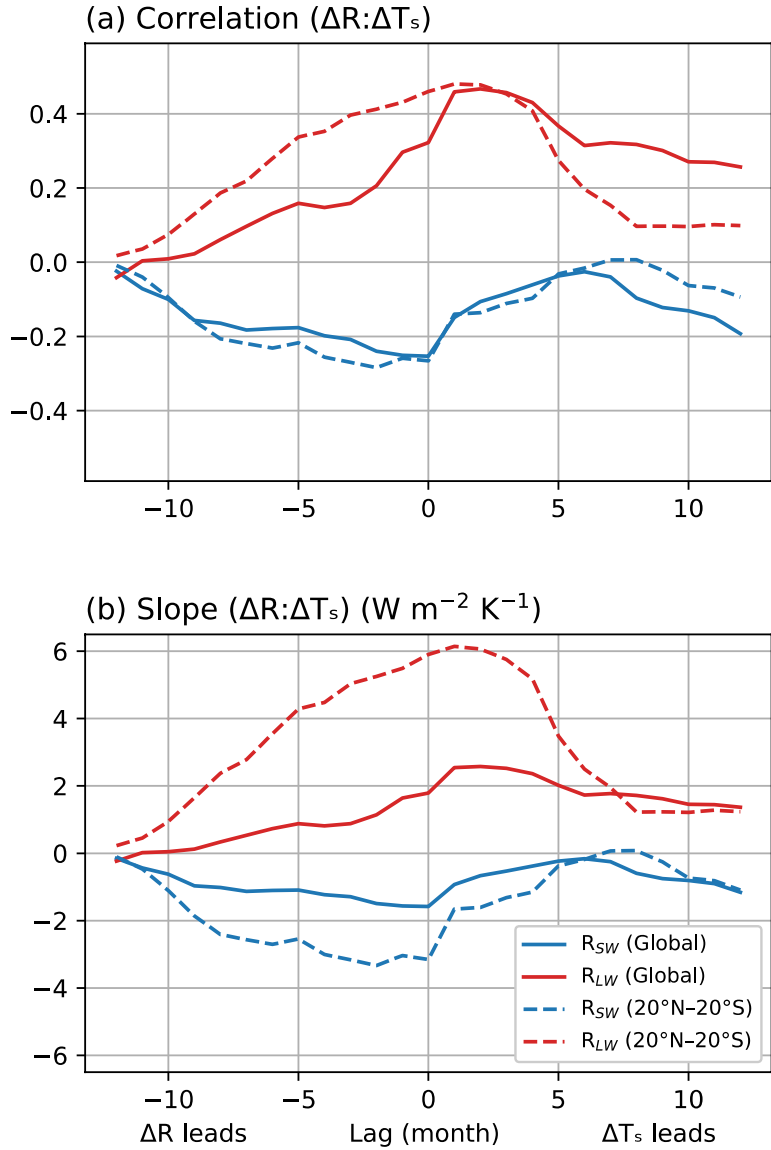


Figure 1. The lagged linear correlation coefficient (a) and regression slope (b) of ΔR versus ΔT_s for shortwave (blue) and longwave (red) radiation; The thick solid line indicates global data, and the thick dashed line indicates 20°S–20°N. Positive signs are used for upward fluxes.

Of course uncertainties in the previous feedback estimates were acknowledged (Spencer and Braswell, 2011), but the reason for the

uncertainties remains unclear. Not-knowing clearly the reason prevents the improved determination of the feedback strength. As will be shown here, the main reason turns out to be significant influence of natural variations of radiation that are not related to feedback processes (called ‘non-feedback’ variations or noise in this study). They are in fact hardly isolated from the observed flux anomalies ΔR in which both feedback and non-feedback variations are blended, even by many currently known methods (including two alternative methods by Spencer and Braswell, 2010 and Lindzen and Choi, 2011).

In order to avoid spurious contribution of the non-feedback variations to feedback, the use of a ‘lagged covariance’ has been suggested (Frankignoul, 1999; Frankignoul et al., 1998). This is because the cause and effect of the change in outgoing radiation fluxes can be identified from lagged covariances. However, only in the case when ΔT_s is mostly remotely generated in time is it likely that the atmospheric response can reflect the true atmospheric feedback in the stochastic determination (Frankignoul, 1999). The influence of non-feedback variations, with the lagged correlation analysis between observed sequential ΔR and ΔT_s will be discussed next.

3.1.2. Cross-correlation between radiation flux and SST

SST instead of global surface temperature was used in the present analysis because land surface temperature is highly variable in observations, providing

large uncertainty in determination of climate feedbacks. The analysis period is from March 2000 to June 2011 (136 months). Both SST and radiative flux data were deseasonalized by monthly climatological means to produce the anomalies of global (both land and ocean) outgoing fluxes and SST, ΔR and ΔT_s . Then the (lagged) cross-correlation analysis is applied to the two anomalies; the correlations and the regression slopes are shown in Figs. 1a and 1b, respectively.

The cross-correlation results with respect to time lag are shown for longwave (LW, red line) and shortwave (SW, blue line) radiation fluxes (Fig. 1a). The thick solid line indicates global average, and the thick dashed line indicates tropical average (20°S – 20°N). Negative lags indicate that ΔR precedes ΔT_s , whereas positive lags indicate that ΔT_s precedes ΔR . The reason for using ΔT_s as the abscissa is because feedbacks are usually defined and reckoned with respect to changes in surface temperature. As a whole, fairly variable correlation coefficients (r) are found according to time lags. Interestingly, only LW in the tropics (20°S – 20°N) shows a distinctively highest correlation at zero lag (thick dashed red line in Fig. 1a).

At the approximate emission temperature of the earth of 255 K and assuming that the emission temperature is linearly related with the surface temperature, the effective Planck longwave cooling is known to be $3.3 \text{ W m}^{-2} \text{ K}^{-1}$ for small perturbations of the surface temperature (e.g., Lin et al., 2011; Lindzen and Choi, 2011; Spencer and Braswell, 2008; Trenberth et al., 2010).

This is so-called Planck response that is proportional to SST, and exclusion of which from LW flux is displayed by thin lines in Fig. 1a. Characteristically, in Fig. 1a, in LW where Planck response is excluded, the sign of correlation around zero lag is very different from LW where Planck response is originally included. Especially for the tropics, when Planck response was excluded from the LW flux anomalies, the convex-shaped correlation (i.e., a maximum at zero lag and lower values at nonzero lags) disappeared. This represents that the Planck response plays a crucial role in stabilizing the lagged correlation to have a highest value at zero lag. However, it should be noted that, for obtaining LW climate feedback associated with specific variables like water vapor or clouds, exclusion of Planck response from LW flux is methodologically unavoidable.

The distorted (usually S-shaped) correlation curves in Fig. 1a shows that the negative correlation at zero lag actually comes from ΔR preceding ΔT_s (i.e., negative lag) and that the correlation changes from negative to positive as ΔR follows ΔT_s (i.e., positive lag). This pattern is also very similar to the regression $\Delta R/\Delta T_s$ slopes in Fig. 1b. Eventually, this opposite sign clearly limits statistical significance of regression slopes at zero lag, although the regression slope is highly fluctuating in the range of -2 to $4 \text{ W m}^{-2} \text{ K}^{-1}$ (Fig. 1b). For example, the coefficient of determination r^2 is only 2% at zero lag for globally averaged SW flux (blue solid line in Fig. 1a); the corresponding $\Delta R/\Delta T_s$ value to this (approximately $-1 \text{ W m}^{-2} \text{ K}^{-1}$ in Fig. 1b) is indeed too

uncertain to represent a general feature of nature, or even to test climate models with the estimated climate feedback from the observation, given that model climate sensitivity is so sensitive to small uncertainty in climate feedbacks (Roe and Baker, 2007). This weak significance at zero lag indicates that the estimation of SW feedback is essentially more difficult than LW feedback.

Figure 1 also clearly compares global averages and tropical averages. The distortion seems more intensified for global averages than tropical averages. The tropical LW data excluding Planck response was much more convexly shaped than the global LW data excluding Planck response (red lines in Figs. 1a and 1b). These results imply that the estimation of global feedback is more difficult than tropical feedback. This is probably associated with major factors inducing ΔR that are mostly the non-feedback cloud changes commonly found to be more frequent in the extratropics and over land.

3.1.3. Distinguishing feedback from non-feedback noise

Only the dependence on surface temperature T_s , however, is directly relevant to cloud feedback. The other factors shall be referred to as ‘noise’ for the sake of distinguishing them from the feedback ‘signal’ in the outgoing radiation flux, though these factors are often more important to cloud formation and composition (note that optical properties of clouds can change – not just cloud amount, Choi et al., 2010). The noise is also called effective

radiative forcing elsewhere, defined as all the instantaneous radiative forcing including fast atmospheric adjustments occurring independently of T_s (Gregory and Webb, 2008). To be clear, the atmospheric factors like water vapor and temperature profiles are directly changed by ΔT_s and in turn indirectly changing clouds are not noise, but are the feedback processes. Note that these too have already been included in the ΔR - ΔT_s analyses.

A key issue here is that the factors occurring independently of T_s (i.e., noise) must be excluded in the estimation of feedback from the ΔR - ΔT_s analysis. This is because doing otherwise generally leads to the distorted lagged correlation with low statistical significance (see Fig. 1). How this noise effect actually works on distorting the correlation is explained in the following. Based on the analysis separating LW and SW, the total ΔR directly observed from the CERES is much more strongly correlated with SW anomalies (coefficient of determination, $r^2 = \sim 60\%$) than LW anomalies ($r^2 = \sim 30\%$), so it is likely that the total ΔR is primarily associated with SW radiation. Simply focusing on SW, for example, instantaneously increased cloud (independently of ΔT_s) would reflect more sunlight (positive ΔR) and thereby cool the surface (negative ΔT_s), which of necessity is a non-feedback contributions to ΔR . This case leads, of course, to negative $\Delta R/\Delta T_s$, overestimating positive cloud feedback from the ΔR - ΔT_s analysis.

In order to distinguish such spurious contributions to feedback from actual

feedbacks, it is necessary to distinguish changes in ΔR that lead changes in ΔT_s (shown as negative lags) from those that lag (shown as positive lags). Only the latter should be considered to be feedbacks. To confirm the necessity of the lagged covariances in the present climate feedback problem, an idealized energy balance model is used here (Eq. 1). Though the model is too simple to simulate the earth's true climate, this model contains enough of the essential nature of climate to determine if the estimation of feedbacks is methodologically appropriate. The nature of climate in the model can be inferred from the known magnitudes and the time scales of climate responses to forcings, without reference to the detailed physical processes that are implemented in complex climate models. The simple model focuses just on the relationship of time series of ΔT_s and ΔR , which is essential for the estimation of feedbacks. By keeping simplicity at the cost of quantitative accuracy, the following simple model provides useful insight without the difficulties associated with complex climate models.

With monthly varying F and constant C_p and λ , it is now possible to simulate time series of temperature anomaly, ΔT_s from Eq. 1. Finite difference integrations of Eq. 1 were carried out for 10 years on monthly time scale (Choi and Song 2012). The radiative forcing plus the feedback process in the model runs appears as the total outgoing radiative flux at the top of the atmosphere ΔR_{TOA} . To correspond to what the CERES instrument actually measures, instrumental or sampling errors (ε) should also be included in ΔR_{TOA} :

$$\Delta R_{\text{TOA}} = -F_{\text{rad}} + \lambda \cdot \Delta T_s + \varepsilon. \quad (6a)$$

Subtracting the Planck response to surface temperature ($\lambda_0 \Delta T_s$) from ΔR_{TOA} , the residual finally indicates outgoing flux anomaly without the Planck response as shown in Fig. 1.

$$\Delta R = \Delta R_{\text{TOA}} - \lambda_0 \cdot \Delta T_s(t) = -F_{\text{rad}}(t) + \lambda \cdot \Delta T_s(t) - \lambda_0 \cdot \Delta T_s(t) + \varepsilon. \quad (6b)$$

It is widely accepted that ΔR is largely associated with cloud variation. However, the extraction of cloud-associated radiation introduces many other problems beyond those considered here. In order to extract cloud forcing from TOA fluxes, one may use information from analyzed data obtained from sophisticated 3-D climate models. Such models are already influenced by the model treatment of clouds which is generally held to be unreliable. The present paper does not attempt to extract cloud forcing. Rather, it is better to use the radiation flux ΔR that is just the total outgoing radiation in which only the Planck response is removed to focus on feedbacks. Moreover, only the methodological problems associated with the use of simple regression are addressed here.

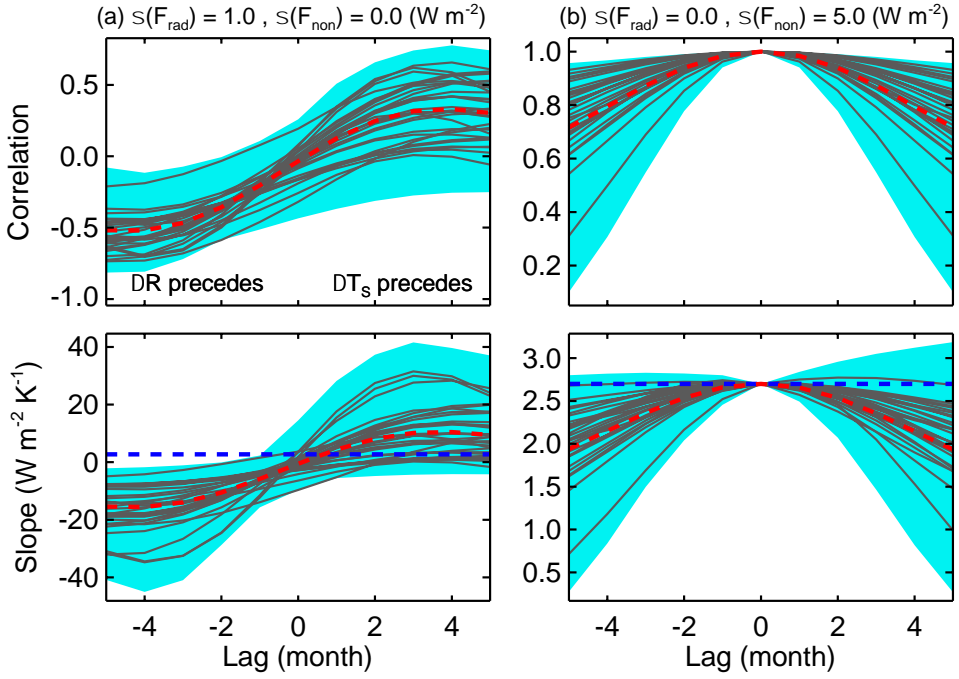


Figure 2. The lagged linear correlation coefficient and regression slope of ΔR versus ΔT_s from the zero-dimensional energy balance model simulations. The blue shaded area indicates the range of the simulated values from 1,000 simulated realizations, and the red dashed line indicates their average. The assumed climate feedback $2.7 \text{ W m}^{-2} \text{ K}^{-1}$ is superimposed by the blue dashed line in the lagged slope graph. The thin solid lines are 30 randomly selected examples. The forcings are purely (a) radiative and (b) non-radiative, respectively [From Choi et al. (2014)].

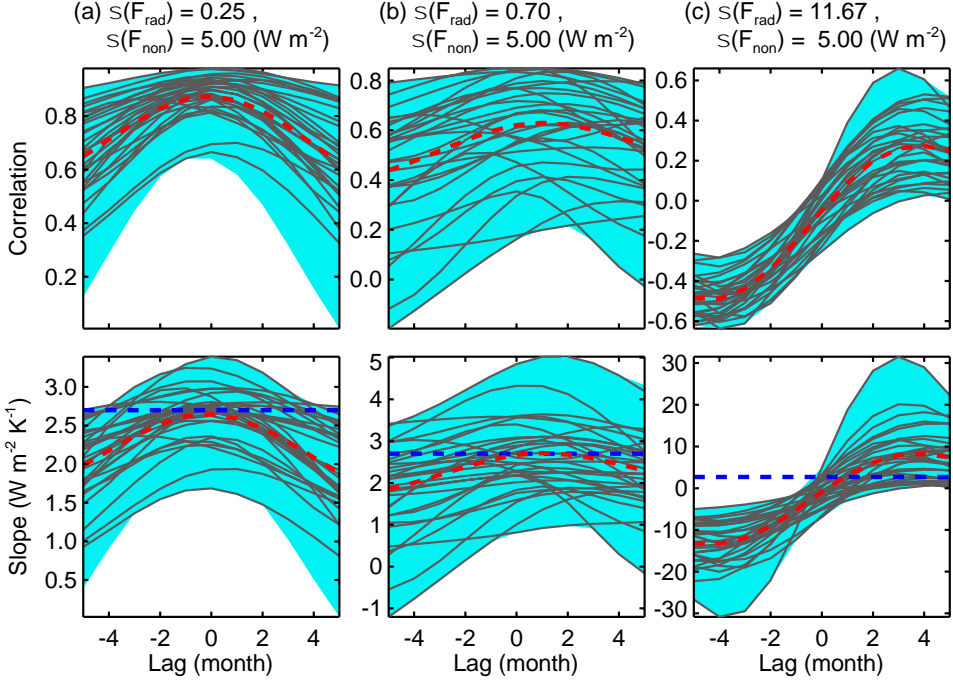


Figure 3. Same as Fig. 2 but for coexisting radiative and non-radiative forcings with $\sigma(F_{\text{rad}})/\sigma(F_{\text{non}}) = 0.05$ (a), 0.14 (b), and 2.33 (c) [From Choi et al. (2014)].

Now one can inquire how the ΔR - ΔT_s lagged correlation is changed by noise. As explained above, both forcings (F_{non} and F_{rad}) in Eq. 1 are basically randomly generated Gaussian numbers with nearly zero mean, but their standard deviations are changed depending on the experiments in Figs. 2 and 3. Figure 2a shows ΔR - ΔT_s correlations with respect to the lagged month of ΔR behind ΔT_s (the abscissa). The blue shaded area is the range of the 1,000 repeated results by the simple model (10 years for each run), and the lines are 30 randomly selected examples. In Fig. 2a, the non-radiative forcing F_{non} was neglected, assuming that all the climatic forcing is purely radiative (observed

at TOA) (i.e., $F_{\text{non}} = 0$ and $F_{\text{rad}} \neq 0$); thus, T_s is changed by noise (like cooling effects of randomly-formed clouds) as well as the feedback process. Randomly generated Gaussian noise is in F_{rad} . The standard deviation of the forcing $\sigma(F_{\text{rad}})$ is set to 1 W m^{-2} . As will be estimated from observations in the next, the present setting of $\sigma(F_{\text{non}})$ turns out to be quite reasonable. In these extensive runs in Fig. 2a, the maxima and minima of correlation coefficients (and regression slopes) were present within finite lead and lag months for most simulations. The detailed shape of the curve varies with randomly generated forcing, but the S-shaped curve is the most common if the forcing is purely radiative.

On the contrary, if the forcing is purely non-radiative (i.e., $F_{\text{rad}} = 0$ and $F_{\text{non}} \neq 0$), most of the results of lagged analyses are similar to Fig. 2b. The standard deviation of the forcing $\sigma(F_{\text{non}})$ is set to 5 W m^{-2} . At larger or smaller lags, correlations are more variable and lower. Correlation was highest and constant at zero lag, resulting in that maxima of regression slopes at zero lag (i.e., the simultaneous regression) is the same as the true feedback $2.7 \text{ W m}^{-2} \text{ K}^{-1}$. Results in Figs. 2a and 2b are completely different. Note that this difference stems from the fact that ΔR_{TOA} in the case of Fig. 2b is determined mainly by feedback processes ($\lambda \Delta T_s$), whereas ΔR_{TOA} in the case of Fig. 2a is determined by both feedback processes and radiative forcing ($-F_{\text{rad}} + \lambda \Delta T_s$) (see Eq. 6a).

In more realistic conditions that both F_{non} and F_{rad} are contributing as

climatic forcings (Fig. 3), the characteristics of ΔR - ΔT_s correlation should be in between the two extreme cases (Figs. 2a, b). Figure 3 shows examples of the lagged correlation (and regression slope) results for various $\sigma(F_{\text{rad}})/\sigma(F_{\text{non}})$ = 0.05 (a), 0.14 (b), and 2.33 (c); these are the values assumed by Dessler (2011), Lindzen and Choi (2011), and Spencer and Braswell (2011), respectively. Here the ε -value is set to zero. Figure 3a shows generally the upward convex shape with highest correlations and slopes around zero lag. Correlations and slopes are, however, more variable and lower than those in Fig. 2b (the extreme case of $\sigma(F_{\text{rad}})/\sigma(F_{\text{non}})$ = 0). Figure 3b shows similar correlations and slopes at all lags or some distorted shape of the lagged correlation and slope. Figure 3c shows mostly the distorted shape, which resembles Fig. 2a. All three cases indicate that $\sigma(F_{\text{rad}})/\sigma(F_{\text{non}})$ smaller than 0.2 can distort the upward convex shape, and complicate the estimation of feedback.

Figure 4 shows more quantitatively the errors in the estimation of feedback with respect to the ratio $\sigma(F_{\text{rad}})/\sigma(F_{\text{non}})$ as well as $\sigma(\varepsilon)$. The error is calculated by the difference between the regression slope at zero lag and the prescribed true feedback parameter (λ). It should be noted that the bar in Fig. 4 represents only the standard deviation of extensive model runs (100 repetitions), which is much smaller than the actual maximal error. Also, the average of the error should not be emphasized too much since it should approach basically to zero if the error distribution is symmetrical. Results clearly demonstrate that the

error increases with increase in the ratio $\sigma(F_{\text{rad}})/\sigma(F_{\text{non}})$ for the same λ . The error also significantly increases with the increase in sampling error (ε). More importantly, the error is considerable even for very small $\sigma(F_{\text{rad}})/\sigma(F_{\text{non}}) \sim 0.05$, particularly in the presence of $\sigma(\varepsilon)$ (Fig. 4a). For smaller $\sigma(F_{\text{rad}})/\sigma(F_{\text{non}})$, the ε -value also plays an important role in increasing the error. Comparing Figs. 4a, 4b, and 4c, the error increases with the increase in λ if all other factors are equal. Interestingly, the error is slightly biased upward for the system with positive feedback ($\lambda = 1 \text{ W m}^{-2} \text{ K}^{-1}$), whereas more greatly downward for the system with negative feedback ($\lambda = 6 \text{ W m}^{-2} \text{ K}^{-1}$). That is to say, feedbacks (positive or negative) tend to be underestimated; more greatly for negative feedback than for positive feedback.

The above simulations clearly show that non-feedback radiative variations strongly affect the lagged covariance between the two observed quantities. The lag serves to determine whether the observed data favors the estimation of feedback or not. It is therefore essential to consider ΔR 's that lead and lag ΔT_s 's; only the top of the upward convex shape according to the lag should be identified with feedbacks.

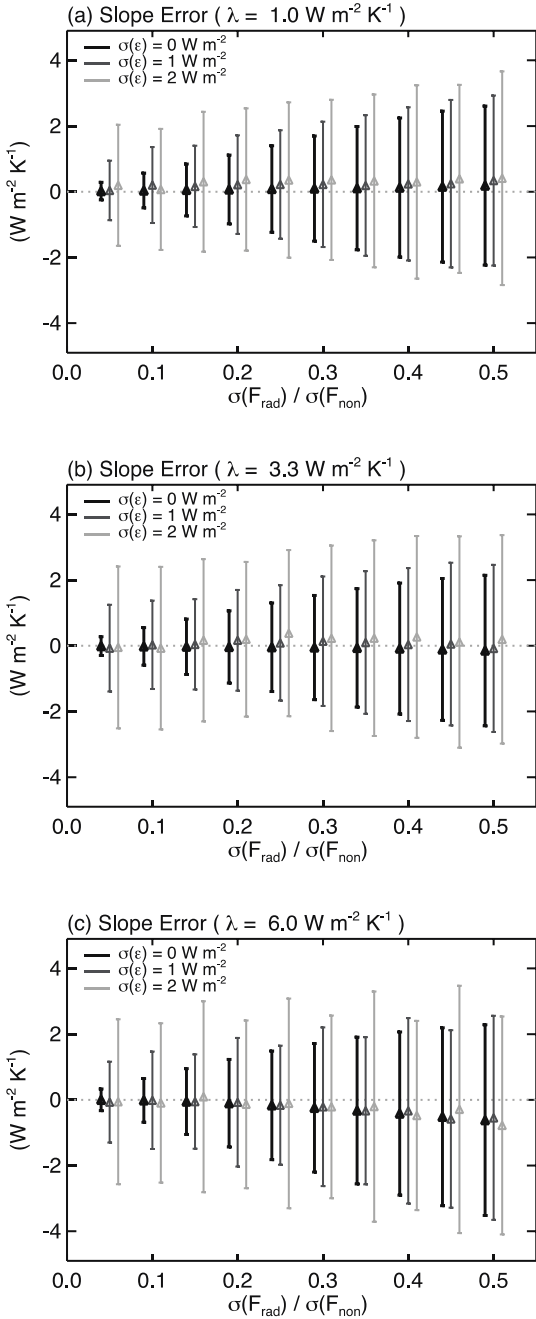


Figure 4. The mean and standard deviation of the errors in estimated feedback parameter (λ) from 100 simulations of the energy balance model. The abscissa indicates the ratio, $\sigma(F_{rad})/\sigma(F_{non})$. The pre-described feedback parameter is $1.0 W m^{-2} K^{-1}$ (a), $3.3 W m^{-2} K^{-1}$ (b), and $6.0 W m^{-2} K^{-1}$ (c) [From Choi et al. (2014)].

3.1.4. Observational assessment of non-feedback variations

The simple model simulations imply that the slope at zero lag cannot be correctly indicative of the climate feedback in the CERES observations if the lagged correlation is distorted according to the lag. This was the case when the temperature change is largely induced by non-feedback radiative variations (or simply noise). To clarify the effect of noise in the currently available data, F_{rad} and F_{non} are calculated. These values can be obtained systematically from the observations in the framework of the simple model.

By separating F_{rad} and F_{non} in Eq. 1 into two independent equations,

$$F_{\text{rad}}(t) = \lambda \cdot \Delta T_s(t) - \Delta R_{\text{TOA}}, \quad (7a)$$

$$F_{\text{non}}(t) = C_p \left[\frac{d\Delta T_s}{dt} \right] + \Delta R_{\text{TOA}} \quad (7b)$$

,

where ΔR_{TOA} and ΔT_s are the same observational data as used in Fig. 1; both are globally averaged monthly anomalous values deseasonalized against the monthly mean for the first 5-year (March 2000–February 2005). Thus F_{rad} and F_{non} are also anomalies relative to the first 5-year means as they are derived from the anomaly data of ΔR_{TOA} and ΔT_s . ΔR_{TOA} is used instead of ΔR for the calculation of F_{rad} and F_{non} , since ΔR_{TOA} is directly measured. F_{rad} is calculated by Eq. 7a for a specified λ . F_{non} is calculated by Eq. 7b independently of λ .

Because ΔR_{TOA} contributes to the calculation of both F_{rad} and F_{non} in Eq. 7,

there is a correlation between F_{rad} and F_{non} , that is dependent on λ : $r = -0.04$ for $\lambda = 0 \text{ W m}^{-2} \text{ K}^{-1}$ to -0.19 for $\lambda = 8 \text{ W m}^{-2} \text{ K}^{-1}$ when using globally averaged CERES ΔR_{TOA} data (solid line in Fig. 5); the stronger the negative feedback (larger λ), the stronger the negative correlation between F_{rad} and F_{non} . In addition, in the case of using ΔR_{TOA} averaged over the ocean only (blue dotted line in Fig. 5), F_{rad} and F_{non} have slightly stronger negative correlation ($r = -0.11$ for $\lambda = 0 \text{ W m}^{-2} \text{ K}^{-1}$ to -0.23 for $\lambda = 8 \text{ W m}^{-2} \text{ K}^{-1}$). However, in the case of using ΔR_{TOA} averaged over the land only (red dotted line in Fig. 5), the correlation is similar to or slightly weaker than that for globally averaged ΔR_{TOA} . In order to compare the observationally based estimates with climate models, Eq. 7 was also applied to the CMIP (Coupled Model Intercomparison Project) runs in IPCC AR4 (2007) (Lindzen and Choi, 2011); λ -values correspond to IPCC AR4 (2007). In terms of correlation between F_{rad} and F_{non} , climate models (plus marks in Fig. 5) have enormously different characteristics from the observation (the solid line in Fig. 5).

As documented previously, variations of F_{rad} and F_{non} indicate the noise effects on estimating climate feedback. Figure 6 shows the estimated magnitudes of $\sigma(F_{\text{rad}})$ and $\sigma(F_{\text{rad}})/\sigma(F_{\text{non}})$. While not shown explicitly in the figure, $\sigma(F_{\text{non}})$ is found to be 5.27 for globally averaged ΔR_{TOA} (5.32 for the ocean-averaged ΔR_{TOA}) in the observation, while CMIP models have a wide range of $\sigma(F_{\text{non}})$ (3 to 9 in Table 1). From the observation in Fig. 6a, $\sigma(F_{\text{rad}})$ with an increase in λ between 0.7 and 0.9 W m^{-2} . Only a few CMIP models

show values comparable to these observational values. Dependence on ΔR_{TOA} should also be mentioned; $\sigma(F_{\text{rad}})$ for $\lambda = 3.3 \text{ W m}^{-2} \text{ K}^{-1}$ is 0.74 for globally averaged ΔR_{TOA} , 0.80 for the ocean-averaged ΔR_{TOA} , and 1.13 W m^{-2} for the land-averaged ΔR_{TOA} . Thus land includes larger non-feedback noise than the ocean or the globe. This supports the earlier finding that the estimation of global feedback is more difficult than the estimation of tropical feedback as seen in Fig. 1.

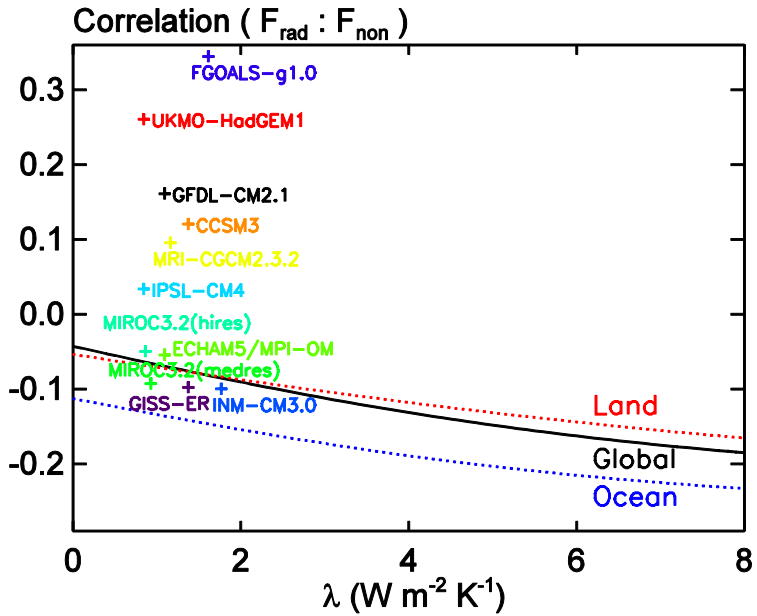


Figure 5. The correlation coefficient (r) between estimated F_{rad} and F_{non} with respect to feedback parameter λ . from the CERES and SST observations (solid line for globally averaged ΔR_{TOA} , blue dotted line for the ocean-averaged ΔR_{TOA} , red dotted line for the land-averaged ΔR_{TOA}), and from 11 CMIP climate models (plus marks) with the estimated values of λ by CO₂-doubling equilibrium experiments (IPCC, 2007) [From Choi et al. (2014)].

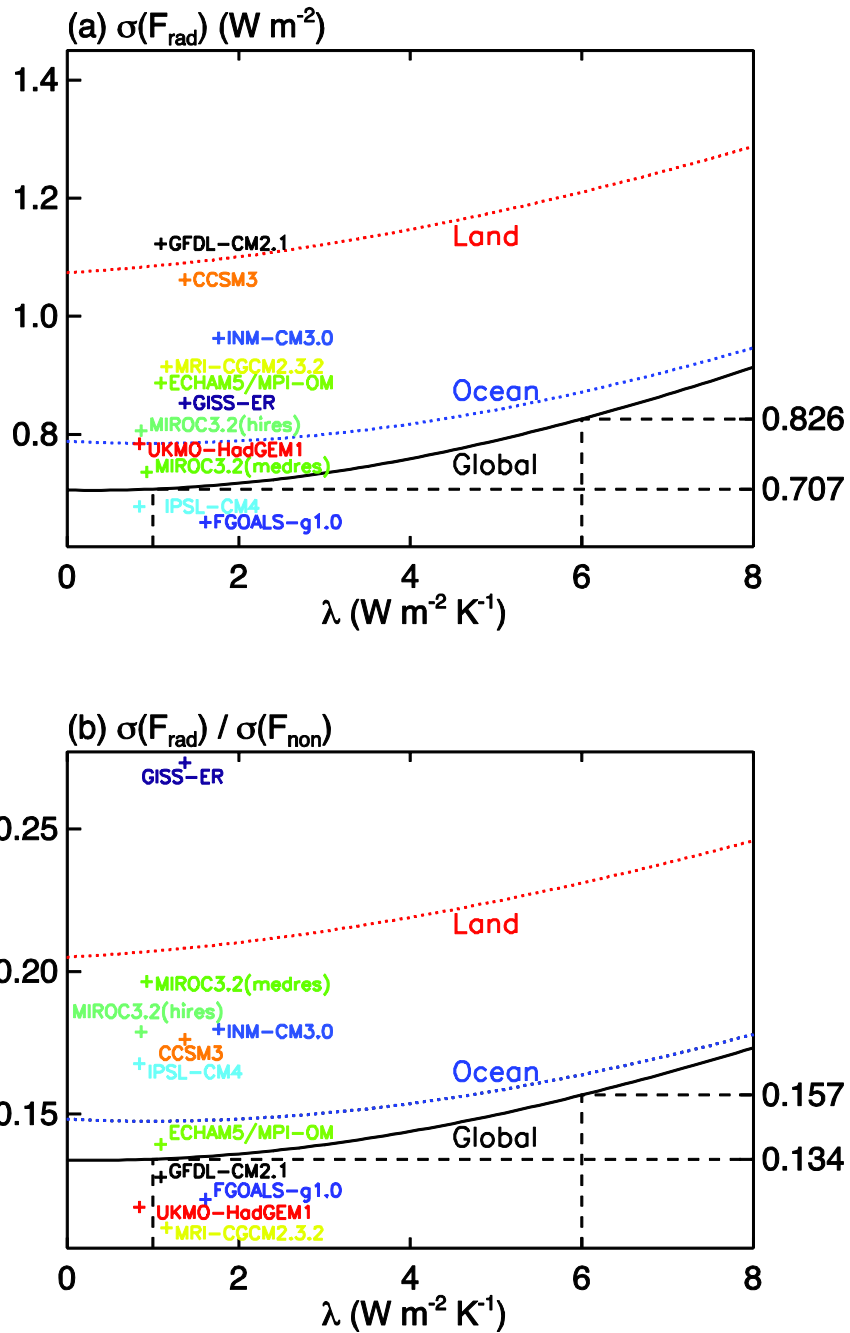


Figure 6. Same as Figure 5 but for $\sigma(F_{\text{rad}})$ (a) and $\sigma(F_{\text{rad}})/\sigma(F_{\text{non}})$ (b) not r . The ratio, $\sigma(F_{\text{rad}})/\sigma(F_{\text{non}})$ from observations is larger than 4 models, and smaller than 6 models [From Choi et al. (2014)].

Table 1. The estimated $\sigma(F_{\text{non}})$ values for 11 CMIP climate models [From Choi et al. (2014)].

Models	$\sigma(F_{\text{non}})$ (W m $^{-2}$)
GFDL-CM2.1	8.78
GISS-ER	3.12
FGOALS-g1.0	5.42
INM-CM3.0	5.36
IPSL-CM4	4.04
MIROC3.2(hires)	4.51
MIROC3.2(medres)	3.75
ECHAM5/MPI-OM	6.36
MRI-CGCM2.3.2	8.31
CCSM3	6.03
UKMO-HadGEM1	6.68

$\sigma(F_{\text{rad}})/\sigma(F_{\text{non}})$ is calculated to be approximately from 0.13 to 0.18 for the global and ocean ΔR_{TOA} (black dashed and blue dotted lines), within the possible range of λ in the observations (Fig. 6b). For the land-averaged ΔR_{TOA} (red dotted line), the $\sigma(F_{\text{rad}})/\sigma(F_{\text{non}})$ value is much larger than that for the global and ocean ΔR_{TOA} . More detailed results on dependence on C_p and λ from the observation are summarized in Table 2. Figure 6b also shows that $\sigma(F_{\text{rad}})/\sigma(F_{\text{non}})$ from CMIP models varies from 0.11 to 0.28, for λ around 1 W m $^{-2}$ K $^{-1}$. This is perhaps the reason why the CMIP models also yield the S-shaped curve in the lagged analyses (Lindzen and Choi, 2011). On the other hand, it is possible that the C_p values used here (14 year W m $^{-2}$ K $^{-1}$) might be too large for the ocean mixed layer of the observed climate or the CMIP

models, especially in monthly time scale. In the present estimations, the dependency of F_{non} on C_p is almost linear, therefore $\sigma(F_{\text{rad}})/\sigma(F_{\text{non}})$ is almost proportional to C_p^{-1} . For instance, when C_p is set to 10 year W m⁻² K⁻¹, the values in Fig. 6b increase by a factor of nearly 1.4 (= 14/10); $\sigma(F_{\text{rad}})/\sigma(F_{\text{non}})$ is approximately from 0.19 to 0.22 in the observations, and from 0.15 to 0.38 in the CMIP models.

Table 2. The estimated $\sigma(F_{\text{rad}})/\sigma(F_{\text{non}})$ values associated with different choices for the bulk heat capacity of the Earth's climate system C_p , and feedback function λ . Globally averaged, the ocean-averaged, and the land-averaged ΔR values are used [From Choi et al. (2014)].

Area	C_p (yr W m ⁻² K ⁻¹)	$\sigma(F_{\text{non}})$ (W m ⁻²)	$\sigma(F_{\text{rad}})/\sigma(F_{\text{non}})$		
			$(\lambda = 1.0$ W m ⁻² K ⁻¹)	$(\lambda = 3.3$ W m ⁻² K ⁻¹)	$(\lambda = 6.0$ W m ⁻² K ⁻¹)
Global	10	3.78	18.7%	19.6%	21.9%
	14	5.27	13.4%	14.1%	15.7%
	21	7.90	9.0%	9.4%	10.5%
	28	10.54	6.7%	7.0%	7.8%
Ocean	10	3.83	20.5%	21.0%	22.7%
	14	5.32	14.7%	15.1%	16.4%
	21	7.95	9.9%	10.1%	11.0%
	28	10.58	7.4%	7.6%	8.2%
Land	10	3.77	28.8%	29.9%	32.1%
	14	5.24	20.7%	21.5%	23.1%
	21	7.85	13.8%	14.4%	15.4%
	28	10.47	10.4%	10.8%	115%

3.2. Longwave cloud feedback over the Pacific warm pool

Based on the understanding of the radiative feedback processes, outgoing longwave radiation (OLR) responses to changes in sea surface temperature (SST) over the Pacific warm pool area (20°N – 20°S , 130°E – 170°W) are investigated. OLR values were obtained from recent (January 2008–June 2010) geostationary window channel imagery at hourly resolution, which resolves processes associated with tropical convective clouds.

3.2.1. Characteristics of clouds over the Pacific warm pool

In response to anomalous radiative forcing, changes in the global mean surface temperature depend largely on the strength of various radiative feedbacks. It is widely accepted that some of the most important, but highly uncertain feedbacks in the global climate system are those involving clouds. Clouds effectively regulate the Earth's top-of-atmosphere (TOA) radiation budget by reflecting solar insolation and trapping planetary infrared emissions; therefore, their response to surface temperature is of primary interest. Previous observational studies of cloud longwave (LW) influences on global warming varied widely (e.g., Lindzen et al., 2001; Rondanelli and Lindzen, 2008; Stephens, 2005; Zelinka and Hartmann, 2010).

One of major reasons for this uncertainty is that the cloud feedback “signal” is not strong enough to be distinguished from the “noise” due to cloud variation in the present observational data. In this context, cloud noise refers

to the variations that occur that are not feedbacks to surface temperature change. Over a short timescale, this noise tends to act as considerable radiative forcing, randomly changing surface temperature, whereas the cloud feedback signal is due to the radiative response of cloud to change in surface temperature. Obviously, this noise effect may bias estimations of the cloud feedback, and yet cannot be eliminated by usual mathematical filtering.

As the cloud's non-feedback noise effect is mixed with cloud feedback processes in the observed records, this study attempts to separate the sea surface temperature (SST) variations caused by clouds and those that change clouds. Only the latter should be categorized as a cloud response to SST change. It will be shown that it may be possible to minimize the noise effect that exists in temporal variations in SST, by using cloud fraction information from high temporal resolution geostationary satellite data. Following previous studies on tropical cloud response to local SST changes (e.g., Horváth and Soden, 2008; Ramanathan and Collins, 1991; Rondanelli and Lindzen, 2008), the analysis are limited to the Pacific warm pool region (PWP; 20°N–20°S, 130°E–170°W). The clouds over the PWP are known to be the most sensitive to local SST change through convective processes (e.g., Zhang, 1993).

Compared to detailed cloud property retrievals from satellites, radiative flux data are more directly associated with the issue of determining “radiative” feedback processes. Moreover, the large differences among the previous

results on tropical cloud feedback may be related to highly uncertain cloud retrievals (e.g., Choi et al., 2005; Choi and Ho, 2009; Ohring et al., 2005). For these reasons, The TOA longwave radiative fluxes that are calculated from satellite-observed radiances were used, as shown below.

Estimation of cloud response to SST change should be supported by observations with a timescale that is short enough to resolve the cloud processes in the atmosphere. For the PWP analysis region, the lifetime of cloud process associated with cumulonimbus is known to range from hours to days. It is difficult to observe fast cloud processes from monthly data for SST and radiative flux. Thus, short-term variations at a timescale of less than a few days will be analyzed.

3.2.2. Observed response of OLR and cloudiness to SST change over the Pacific warm pool

Cloud variations in the PWP have been monitored hourly by the MTSAT-1R on the geostationary orbit centered at 140°E. The window channel (centered at 11 μm) imagery of MTSAT-1R is useful to capture longwave variations due to changes in both clouds and surface temperature, because the effects of other factors, such as column-integrated water vapor and vertical structure of atmospheric temperature, barely interfere with radiance at that wavelength. Linear regression slopes ($\Delta OLR/\Delta SST$) are calculated for each set of anomalous ΔOLR and ΔSST time series. To overcome the limitation of

linear regression slope in determining causality between OLR and SST. The cross-correlation coefficients for different time lags between ΔOLR and ΔSST were also examined. For comparison with results from daily data, the monthly-mean ΔOLR_x and ΔSST_x values are also calculated by simple time-averaging.

Initially, the instantaneous (coincident) relationship between $\Delta OLR_{\text{entire}}$ and $\Delta SST_{\text{entire}}$ was calculated on daily and monthly timescales. The linear regression slope ($\Delta OLR_{\text{entire}}/\Delta SST_{\text{entire}}$) from monthly data was $4.20 \pm 5.84 \text{ W m}^{-2} \text{ K}^{-1}$ (mean \pm standard error). As the regression slope is greater than the Planck response of longwave emission ($3.3 \text{ W m}^{-2} \text{ K}^{-1}$), the obtained slope may imply that the Earth's climate has a slight longwave cooling effect for increased SST. This result is consistent with most previous studies using monthly-mean data (e.g., Lindzen and Choi, 2009), but raises concerns about the wide uncertainty range of the slope, mostly owing to the small sample size. Interestingly, using daily-mean data, it is found that much higher regression slope ($\Delta OLR_{\text{entire}}/\Delta SST_{\text{entire}} = 8.31 \pm 1.76 \text{ W m}^{-2} \text{ K}^{-1}$), implying strong release of longwave radiation for increased SST.

The positive correlation between $\Delta OLR_{\text{entire}}$ and $\Delta SST_{\text{entire}}$ would not only be a consequence of SST-induced OLR change, but also of OLR-induced SST change. That is to say, it is feasible that the strong positive correlation would be induced solely by SST contaminated by non-feedback cloud noise. For instance, it is natural that the decrease in cloud fraction leads to the increase

in SST by allowing greater solar heating of the surface; at the same time, OLR would increase owing to warmer emission temperature (i.e., more infrared emission from the surface). Hence, the process finally gives positive correlation between OLR and SST. However, as mentioned, unless the increased SST eventually affects clouds, this does not represent feedbacks between SST and cloud.

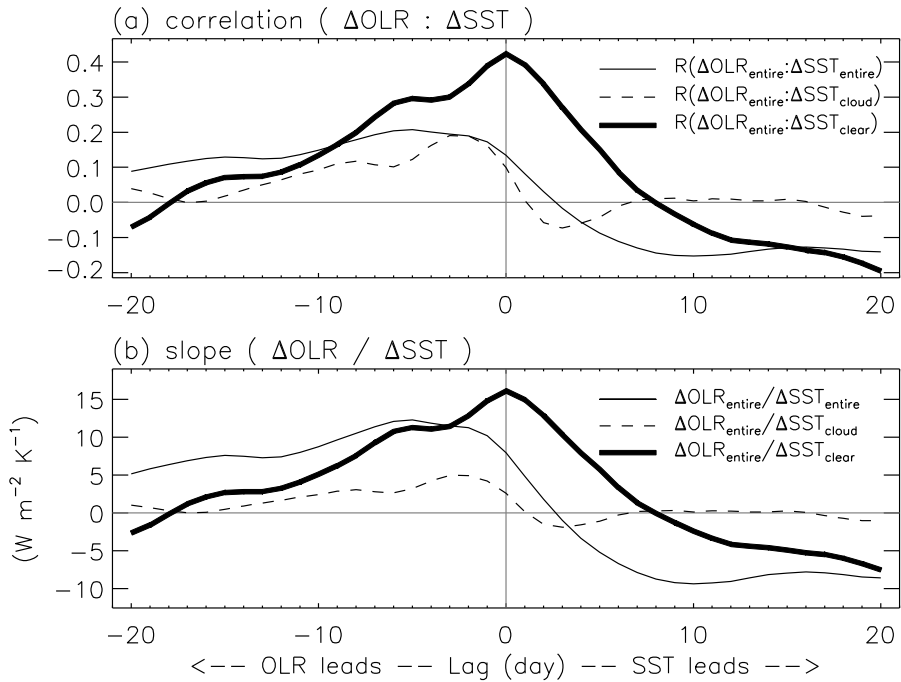


Figure 7. Lagged linear correlations (a) and regression slopes (b) between $\text{OLR}_{\text{entire}}$ and SST. Positive abscissa value indicates that SST leads OLR. SSTs are averaged over the entire domain of analysis (thin solid), cloudy area (dashed), and clear-sky area (thick solid) [From Cho et al. (2012)].

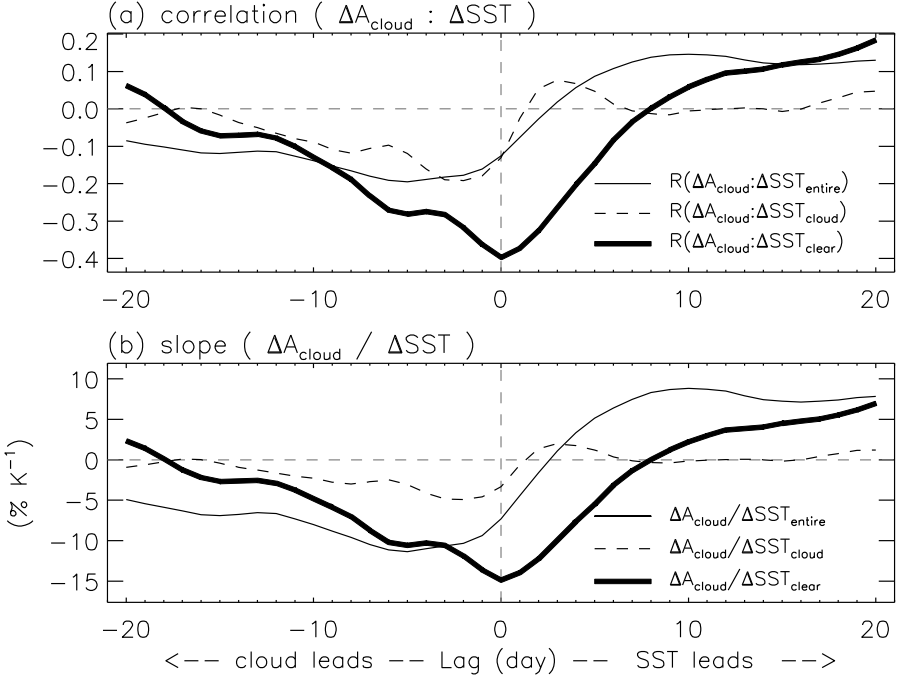


Figure 8. Lagged linear correlations (a) and regression slopes (b) between $AREA_{\text{cloud}}$ and SST_{clear} . Positive abscissa value indicates that SST_{clear} leads $AREA_{\text{cloud}}$. SST_{clear} is averaged over the cloud-free area, and $AREA_{\text{cloud}}$ is relative cloud coverage [From Cho et al. (2012)].

The non-feedback cloud process may often occur over the PWP region, and may readily prevent appropriate interpretation of the regression slope relevant to the radiative feedback strength. Therefore, it is necessary to investigate how the cross-correlation coefficient changes according to the time lag between OLR and SST, in order to get a better idea of whether the regression slope at zero lag is representative of radiative feedback strength, i.e., OLR change induced solely by SST change. Figure 7 shows the cross-regression between daily-mean ΔOLR and ΔSST , where negative lag indicates that OLR leads SST; positive lag indicates that SST leads OLR. It is known that, in the

case that OLR leads SST, the maximum R^2 tends to appear at negative lag, and R^2 at zero lag tends to be non-significant (Spencer and Braswell, 2010). This case is seen in Fig. 7a; the maximum R^2 between $\Delta OLR_{\text{entire}}$ and $\Delta SST_{\text{entire}}$ (thin solid line) is observed for a lag of approximately minus-5 days, and the value of R^2 decreases with increasing time lag, indicating that longwave radiative forcing affects SST. This effect is more evident for the further analysis with $\Delta SST_{\text{cloud}}$, which is expected to be more strongly influenced than $\Delta SST_{\text{entire}}$ by cloud radiative forcing. The corresponding cross-correlation coefficient between $\Delta OLR_{\text{entire}}$ and $\Delta SST_{\text{cloud}}$ is represented by the dashed line in Fig. 7a, showing that the OLR–SST relationship is almost uncorrelated at around zero lag, similarly to the case with $\Delta SST_{\text{entire}}$.

However, OLR variations in response to SST are revealed by comparison of ΔSST with preceding (or at least coincident) ΔOLR (i.e., at zero or positive lags). Interestingly, unlike the analysis with $\Delta OLR_{\text{entire}}$ and $\Delta SST_{\text{cloud}}$, the maximum R^2 between $\Delta OLR_{\text{entire}}$ and $\Delta SST_{\text{clear}}$ at zero lag appears as the top of the convex shape in the graph (thick solid line in Fig. 7a). The value of $\Delta OLR_{\text{entire}}/\Delta SST_{\text{clear}}$ at zero lag is $15.72 \pm 1.02 \text{ W m}^{-2} \text{ K}^{-1}$ (thick solid line in Fig. 7b). It is known that this convex shape in the lead–lag relationship gives the desired signal of the cloud response to SST change from the regression slope at “zero” lag (e.g., Frankignoul et al., 1998; Lindzen and Choi, 2011) once ignoring the possibility that the feedback effect can be delayed by ocean/atmosphere processes. This convex shape, however, would not occur

with strong cloud contamination of the SST variation data (Lindzen and Choi, 2011). It is noted that, for monthly data, the results ($\Delta OLR_{\text{entire}}/\Delta SST_{\text{clear}}$) do not show the convex shape. This may be because monthly $\Delta OLR_{\text{entire}}/\Delta SST_{\text{clear}}$ allows various processes at different timescales that may contaminate the signal of the exact cloud response to SST change.

It is also worth examining whether SST_{clear} is physically meaningful in relation to tropical cloud processes. Strong correlation between $\overline{SST}_{\text{clear}}^{\text{day}}$ and $\overline{SST}_{\text{entire}}^{\text{day}}$ (correlation coefficient is 0.90) assures that $\Delta SST_{\text{clear}}$ can also represent essentially the SST variability over PWP. Despite this strong correlation, however, $\Delta SST_{\text{entire}}$ and $\Delta SST_{\text{clear}}$ (as well as $\Delta SST_{\text{cloud}}$ and $\Delta SST_{\text{clear}}$) have remarkably different lead-lag relationships with $\Delta OLR_{\text{entire}}$. This provides an important reason why the slope $\Delta OLR_{\text{entire}}/\Delta SST_{\text{clear}}$ is not an artifact of uneven horizontal distribution of SST field over the PWP. If the slopes were artifacts from the SST field, then the lead-lag relationship between $\Delta OLR_{\text{entire}}-\Delta SST_{\text{cloud}}$ would be similar to that of $\Delta OLR_{\text{entire}}-\Delta SST_{\text{clear}}$ because SST_{clear} and SST_{cloud} would only reflect the variations in cloud coverage. Thus, SST_{clear} as the noise-reduced SST can correctly indicate the magnitude of forcing that changes clouds.

Physically, the high correlation between $\overline{SST}_{\text{clear}}^{\text{day}}$ and $\overline{SST}_{\text{entire}}^{\text{day}}$ may reflect the role of dynamics to reduce horizontal variations in SST. Convection, by contrast, increases horizontal variations in SST, causing de-

correlation between SST_{clear} and SST_{entire} . The correlation coefficient between 90-day smoothed $\overline{SST}_{\text{clear}}^{\text{day}}$ and $\overline{SST}_{\text{entire}}^{\text{day}}$ is higher ($R = 0.95$) than that of the shorter time scale $\Delta SST_{\text{clear}}$ and $\Delta SST_{\text{entire}}$ ($R = 0.73$). This confirms that, over the PWP, the time scales for the dynamics longer than the time scales for convection.

In order to examine how clouds are involved in OLR variations, the OLR variability were analyzed in association with clouds by separation of cloudy-sky OLR and clear-sky OLR. The OLR variations are regulated mostly by the longwave emission, especially from clouds and the earth's surface, because the OLR is inferred from $11 \mu\text{m}$ radiation only. Beside the contribution of the surface to the variation in OLR via the Planck response, the variation in OLR is regarded as a function of (1) cloud-top temperature (T_{cloud}), and (2) horizontal coverage of clouds (A_{cloud}). The T_{cloud} mainly determines OLR_{cloud} which calculation is confined within cloudy-sky area only, while both T_{cloud} and A_{cloud} determine OLR_{entire} . The cross-correlation analysis between $\Delta OLR_{\text{cloud}}$ and $\Delta SST_{\text{clear}}$ indicates that cloud thermal emission associated with T_{cloud} is uncorrelated with the variation in SST (not shown in the figure). This potentially supports the hypothesis that the cloud top temperature is insensitive to SST (Hartmann and Larson, 2002).

More importantly, ΔA_{cloud} and $\Delta SST_{\text{clear}}$ had significant negative correlation with its minimum peak of cross-correlation coefficient at zero lag (thick solid line in Fig. 8a); the corresponding regression slope, $\Delta A_{\text{cloud}}/\Delta SST_{\text{clear}}$ is -14.4

$\pm 1.0\% \text{ K}^{-1}$ (thick solid line in Fig. 8b). In this case, the convex shape with a peak at zero lag is revealed, confirming the validity of the slope. Of course, this shape does not appear when using cloud-affected SST anomalies, $\Delta SST_{\text{entire}}$ and $\Delta SST_{\text{cloud}}$. $\Delta A_{\text{cloud}}/\Delta SST_{\text{entire}}$ (and $\Delta A_{\text{cloud}}/\Delta SST_{\text{cloud}}$) is negative at negative lag, and becomes positive at positive lag. This probably results because increased A_{cloud} cools the SST owing to the cloud dimming effect. Consequently, the result of ΔA_{cloud} (Fig. 8) is very consistent with that of $\Delta OLR_{\text{entire}}$ (Fig. 7).

As mentioned previously, these results are based on the BT_{11} threshold value of 280 K for clear-sky pixel detection. To check the dependence of the result on the choice of the threshold, various threshold values were applied between 270 K and 290 K for clear-sky pixel detection. Irrespective of the selected threshold, the convex shape of the correlation with respect to time lag was maintained. If this threshold is less than 270 K (allowing excessively larger clear-sky area), the maximum R^2 between $\Delta OLR_{\text{entire}}$ and $\Delta SST_{\text{clear}}$ shifts to negative lags, implying that the influence of OLR on SST_{clear} becomes important. The slopes at zero lag for the thresholds of 270, 280, and 290 K are shown in Table 3. It is shown that, for more rigorous threshold for clear-sky detection, the value of $\Delta OLR_{\text{entire}}/\Delta SST_{\text{clear}}$ is lower. This may result from less sampling of clear-sky SSTs, as well as from excluding more of the influence of cloud on SST.

On the other hand, for thermally colder clouds with $BT_{11} < 260$ K,

$\Delta A_{\text{cloud}}/\Delta SST_{\text{clear}}$ was smaller by $\sim 3\% \text{ K}^{-1}$ compared to the cloud with $BT_{11} < 270 \text{ K}$, irrespective of clear-sky SST. This implies that relatively thin clouds (corresponding to BT_{11} between 260 K and 270 K) would decrease by $\sim 3\% \text{ K}^{-1}$. Table 3 also shows the results from the reduced major axis (RMA) method (the numbers in parentheses), which is known to be more appropriate for relating two co-dependent variables, or for an independent variable that includes errors (Smith, 2009). Note that a slope from simple linear regression may bias toward zero value, in comparison to the RMA method. Although this RMA gives more intensified slopes without changing the sign, the different slopes obtained from different statistical approaches is an issue to be addressed; however, this is beyond the scope of the present study.

Table 3. The value \pm standard errors of $\Delta OLR_{\text{entire}}/\Delta SST_{\text{clear}}$ and $\Delta A_{\text{cloud}}/\Delta SST_{\text{clear}}$ from simple linear regression with different BT_{11} thresholds for clear-sky/cloudy pixel detection; all the anomaly values are daily means. The results from the reduced major axis method are shown in parentheses [From Cho et al. (2012)].

Variables	Clear-sky detection test		
	$BT_{11} \geq 270 \text{ K}$	$BT_{11} \geq 280 \text{ K}$	$BT_{11} \geq 290 \text{ K}$
$\Delta OLR_{\text{entire}}/\Delta SST_{\text{clear}}$ ($\text{W m}^{-2} \text{ K}^{-1}$)	16.63 ± 1.19 (39.37 ± 1.14)	15.72 ± 1.02 (34.53 ± 1.00)	11.76 ± 0.77 (25.80 ± 0.74)
$\Delta A_{\text{cloud}} (BT_{11} < 270 \text{ K})/\Delta SST_{\text{clear}}$ ($\% \text{ K}^{-1}$)	-15.1 ± 1.2 (-38.7 ± 1.1)	-14.4 ± 1.0 (-34.0 ± 1.0)	-11.0 ± 0.8 (-25.4 ± 0.7)
$\Delta A_{\text{cloud}} (BT_{11} < 260 \text{ K})/\Delta SST_{\text{clear}}$ ($\% \text{ K}^{-1}$)	-12.3 ± 0.9 (-30.2 ± 0.9)	-11.6 ± 0.8 (-26.4 ± 0.8)	-8.8 ± 0.6 (-19.8 ± 0.6)

Lindzen et al. (2001) also used geostationary satellite observations, and

demonstrated significant reduction in cloud coverage with increasing SST over the similar analysis region. It is noted that Lindzen et al. hypothesized that proper estimation of the cloud feedback essentially requires normalization by “cumulus area” to distinguish changes in the amount of convection from changes in detrainment per unit convection. The cumulus area, as defined by Lindzen et al., can be extracted by $BT_{11} < 220$ K. Based on this definition, the response of the cumulus area to SST change (i.e., ΔA_{cloud} ($BT_{11} < 220$ K)/ $\Delta SST_{\text{clear}}$) was also examined; but significant changes in cumulus area were not found, therefore, it was not possible to determine a robust quantity owing to the distorted shape of cross-correlation. This is possibly because examining the area of cumulus ($BT_{11} < 220$ K) against a 90-day filtered SST should not give a very clear signal, since cumulus area depends on the absolute value of the SST. It is likely that almost of the PWP is occupied by convection, and the amount of convection remains relatively constant with little influence of moisture convergence into or out of the PWP. Despite all these uncertainties, the cloud shrinkage is evident in this study without any normalization procedure (e.g., Lindzen et al., 2001; Rapp et al., 2005). Beside the issue of the normalization effect, this study suggests that the analysis by Lindzen et al. (2001) and subsequent studies (e.g., Choi et al., 2005; Lin et al., 2002; etc.) would remain unsatisfactory, in that they have examined only coincident relations between cloud and SST. Moreover, their cloud-weighted SST is similar to SST_{cloud} defined in this study, which, as

demonstrated, can bring about differing interpretation of cloud response to SST change.

4. Longwave effects of Arctic clouds

The recent decline in the Arctic sea-ice cover can facilitate an opportunity for an assessment of the cloud feedback because it has acted as a strong surface forcing to the atmosphere enough to influence clouds. In this section, the performance of the Polar WRF model in simulating Arctic winter clouds is tested, and then the modelled cloud responses to the sea-ice reduction are investigated.

4.1. Arctic winter clouds in Polar WRF simulations

Recent Arctic observations have revealed large cloud amounts in the lower troposphere throughout the year (Cesana et al., 2012). This is important because the thermal forcing at the surface is more influenced by low-level clouds than by high-level clouds (Kay et al., 2016). The surface downward longwave radiation (DLR) is known to have a large influence on the Arctic surface climate. The influence is enough to account for half of the winter-mean sea-ice variations that are heavily dependent on the vertical structure of the clouds (Park et al., 2015). On the other hand, the cloud's influence on the sea-ice can feedback to the cloud itself because the horizontal extent of the sea-ice determines the potential amount of surface evaporation from the open ocean that regulates the amount of Arctic cloud water. This two-way interaction between the clouds and the sea-ice constitutes a feedback process

(Klaus et al., 2016). Understanding how this feedback operates is required for a better understanding of the Arctic weather and climate (Curry et al., 1996; Goosse et al., 2018; Overland et al., 2016).

Recently, the winter season has attracted more attention from Arctic researchers due to the accelerated wintertime surface warming since the late 1990s along with the decline of sea-ice concentrations especially over the Atlantic sector of the Arctic Ocean (Comiso, 2006; Francis and Hunter, 2007). Numerous studies have shown that the Arctic sea-ice concentration over the Barents Sea has potential predictability for the near-surface temperatures over the Eurasian continent during the winter season (Kim et al., 2014; Kug et al., 2015). Given the large influence of clouds on the underlying surface radiative budget (Graversen et al., 2008), the characteristics of Arctic winter clouds and their recent changes (Jun et al., 2016; Liu et al., 2007) should be examined in detail. However, relatively few winter Arctic cloud studies have been reported compared to other seasons. This is due to the difficulty in obtaining wintertime Arctic observations owing to the harsh weather conditions, lack of visibility, as well as the sea-ice that covers most of the Arctic Ocean (Arctic Climate Impact Assessment, 2005; Karlsson and Svensson, 2011). Even for a satellite-borne instrument like the Moderate Resolution Imaging Spectroradiometer (MODIS), cloud detection can be less accurate (Chan and Comiso, 2013) and the retrievals of cloud optical properties (such as optical thickness or droplet effective radius) based on solar techniques are impossible

in regions that experience polar night.

4.1.1. Observation and simulation of Arctic winter cloud

Model-based Arctic research has been hampered by the scarcity of observations (Kay et al., 2016). In the polar regions, climate model simulations have larger across-model spread than other regions, and the disagreement is largest during the winter season (Chernokulsky and Mokhov, 2012; Intergovernmental Panel on Climate Change, 2013; Karlsson and Svensson, 2011, 2013). However, the uncertainty of the global climate model in simulating the Arctic winter can be reduced by utilizing a regional model. Regional models are better for representations of the surface climate, as well as the cloud characteristics, due to additional constraints given by prescribing lateral boundary conditions. Further, as they usually allow for a higher spatial resolution, a more accurate simulation might be expected (Jung et al., 2006; Pope and Stratton, 2002). The polar-optimized version of the Weather Research and Forecasting (Polar WRF) model has been used for studies on clouds in polar regions to reveal the cloud's role in the Arctic climate and its interaction with the recent sea-ice changes (Barton and Veron, 2012). The accuracy of cloud properties simulated by the Polar WRF has increased due to the growing coverage of Arctic ground stations and a number of field observation campaigns providing better data for initializing models and process-based understanding required for parameterization development. In

addition, newly developed and improved cloud microphysics schemes make a substantial contribution to the improved simulation (Listowski and Lachlan-Cope, 2017). Still, winter season clouds have yet to be sufficiently examined in either observational or modeling studies.

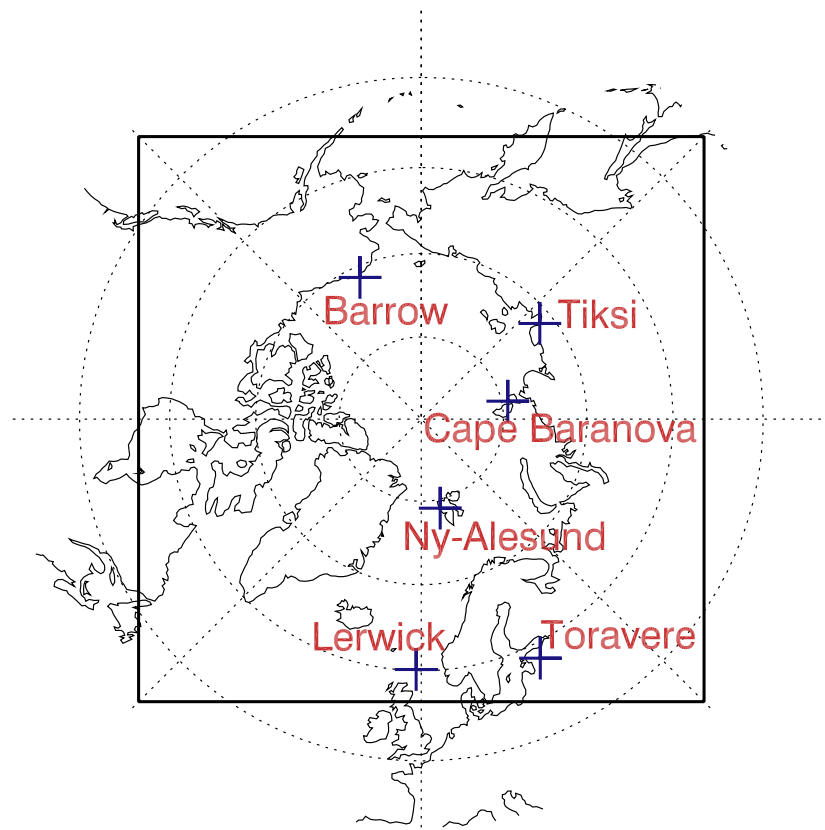


Figure 9. Model domain used for the Polar WRF simulations. The domain consisted of 300×300 grid points with a 24-km horizontal resolution. Crosses indicate the locations of the ground sites used for radiation observations.

Active instruments can provide invaluable Arctic cloud observations

during the winter season because their observations are not restricted by solar light conditions. In addition, vertically resolved cloud structures can be obtained using these observations. This study utilizes cloud observations from two satellite-borne active instruments, namely, the CPR onboard the CloudSat satellite and the CALIOP onboard the CALIPSO satellite. Launched in 2006, these two instruments were placed into the Afternoon Constellation orbit, the so-called “A-train”. By comparing with the cloud observations from MODIS onboard the Aqua satellite that is also a member of the A-train, the benefits of cloud retrievals from the CPR and CALIOP (Chan and Comiso, 2011, 2013; Liu et al., 2012) in detecting wintertime low-level arctic clouds can be shown since MODIS has trouble distinguishing them from underlying sea-ice (Chan and Comiso, 2013).

DARDAR (raDAR/liDAR) cloud products are derived from the combination of CloudSat radar and CALIPSO lidar observations (Delanoë and Hogan, 2008, 2010). This combination is more synergistic for observing winter Arctic clouds with small water contents and large low-level fractions, although the accuracy of the products has not been tested by comparison with independent cloud observations. As active instruments, both CPR and CALIOP, are the best ways to retrieve cloud microphysical variables over regions that experience polar night. The optical thickness of Arctic clouds is expected to be less during the winter season than other seasons because the amount of cloud water is limited by the extremely cold air temperatures and

there would be less fetch from the frozen ocean surface. Thus, CALIOP's lidar observations can help detect clouds with small droplet sizes that are not well detected by the CPR's radar. On the other hand, low-level cloud observations from CALIOP can be blocked by thick clouds above due to the lidar signal attenuation. Thus, any information on these low-level clouds detected by the CPR is beneficial. This complementary retrieval is valuable considering that the vertically contiguous clouds that extend from the lower troposphere to the upper troposphere are frequent during wintertime in the Arctic regions (Oreopoulos et al., 2017). In this study, a 3-D cloud mask and ice water contents were used that are produced for the same horizontal (about 1 km) and vertical (60 m) resolutions with the CloudSat observations. These scales are much smaller than the resolution of the model simulations. Although the comparison might be affected by the discrepancy in scale between the satellite observations and the model simulations, it can provide useful information for future Polar WRF applications with similar configurations. In addition, the sensitivity of clouds to model resolution is known to be mostly related to convection processes (e.g., Bryan and Morrison, 2012) which are less significant in the Arctic environment.

4.1.2. Macrophysical Properties

The winter of 2015–2016 that was characterized by a strong Arctic storm season with an above-average number of organized snow storms (McCarthy

et al., 2016) was simulated. As such, a variety of cloud features were obtained, not only ubiquitous low-level stratus near the surface, but also Arctic storms that extended to the tropopause. During this period, the entry of a strong windstorm into the Arctic Ocean, known to trigger the abrupt shift of the Arctic Oscillation from a positive to a negative phase, occurred around early January 2016 (Kim et al., 2017). This, as a result, allows the evaluation of model performance under a wide variety of environmental conditions.

The statistical comparisons between the satellite observations with the model simulations were mostly performed using the level-2 observations from each satellite. Each satellite observation point was assigned to the WRF grid that enclosed it. Because the grid size of the WRF simulation is larger than the footprint sizes of the satellite observations, a simple average of the satellite observations was compared to the value for the WRF grid that enclosed it. Further, from the hourly WRF outputs, the simulation that was nearest in time to the satellite observation was chosen. Thus, any element of the WRF-satellite-matched datasets was always within at least 12 km in space and 30 min in time. During the two-month period, 125,318 WRF grids were collocated with the DARDAR dataset and 362,306 WRF grids were collocated with the CERES dataset.

The satellite cloud properties are fundamentally different from model-simulated clouds because they are based on retrievals. To enable a more direct comparison between satellite-observed clouds and model-simulated clouds,

the radar simulator (Haynes et al., 2007) and the lidar simulator (Chepfer et al., 2008) integrated into the Cloud Feedback Model Inter-comparison Project Observational Simulator Package (COSP; Bodas-Salcedo et al., 2011) version 1.4 were used. The simulators were applied to the Polar WRF output to mimic satellite-like radar or lidar signals so they could be directly compared to the CloudSat and CALIPSO observations, following the offline calculation approach by Diaz et al. (2015).

Table 4. Mean heights of cloud top in the DARDAR (raDAR/liDAR) cloud data (combined cloud retrievals using CloudSat and CALIPSO) and in the Polar WRF simulations. The values in parentheses denote the correlation coefficients between the DARDAR cloud heights and the modelled cloud heights. The Morrison scheme and the WSM6 scheme were used for the cloud microphysics in the simulations.

	DARDAR	P-WRF (Morrison)	P-WRF (WSM6)
Cloud Top Height (Correlation with DARDAR)	5,590 m (-)	5,880 m (0.72)	5,230 m (0.69)

The macrophysical properties of clouds in the Polar WRF simulations are compared to those of the DARDAR cloud mask in Table 4. The values were obtained for all areas under the satellite paths including cloud-free areas. Note that the existence of a modelled cloud is defined when the total mixing ratio of all cloud hydrometeors exceeds $10^{-9} \text{ kg kg}^{-1}$. In the collocation dataset that combines the Polar WRF simulation and the DARDAR cloud mask (Table 4), the top height of the cloud was higher by 290 m on average when the Morrison double moment scheme was used to represent the cloud microphysics. This is

smaller than the vertical resolution of the model simulations which is larger than 500 m above a 3-km height from the surface. The mean bias was also small using the WSM6 scheme as the cloud top height was lower than the DARDAR dataset by 360 m. The correlation coefficient between the DARDAR's cloud top height and the Polar WRF cloud top height was 0.72 with the Morrison scheme and 0.69 with the WSM6 scheme assuring the model processes were correctly producing the cloud-top heights. When the CALIPSO cloud mask was used instead of the DARDAR dataset, the correlation coefficients were similar but the modelled cloud top was lower than the CALIPSO retrievals by 90 m and 720 m for the Morrison scheme and the WSM6 scheme, respectively. Van Weverberg et al. (2013) found that, with the WSM6 scheme, the fall speed of ice particles in the upper troposphere is faster than with the Morrison scheme, which likely contributes to the higher cloud top with the Morrison scheme.

Cloud amounts were defined differently in Figs. 10a and 10b. In Fig. 10a, “cloud occurrence” is defined as 0 or 1 when a WRF grid is cloud-free or cloudy, respectively. For DARDAR, it is 0 if there is no cloud in the satellite observations within the collocated WRF grid; otherwise, it is 1. In Fig. 10b, the “cloud fraction” for the Polar WRF simulation is the model output variable with the same name diagnosed by the WRF’s radiation code. For DARDAR, it is the ratio of the number of cloudy observations to the number of total observations within the collocated WRF grid. The geometric height

given in the DARDAR for the vertical coordinate was converted into the vertical coordinate of the WRF simulation for the comparisons. At the bottom level, clouds were found at about 60 to 65% of the total collocated grid points in the model simulations (Fig. 10a), similar to the 65% coverage reported by Karlsson and Svensson (2013) and Kay et al. (2016). Figure 10a reveals that clouds are very likely to exist at the model’s bottom level, consistent with the appearance of many low-level boundary clouds in the Arctic. Therefore, temporal or spatial variations in the base height of modelled clouds can be too small to quantify. The discrepancy at levels below 2 km between the satellite retrievals and the model is likely due to the different vertical coordinate between the satellite data and the model simulations. Also, there are possibilities that small cloud particles in low-level clouds cannot be detected by the CloudSat radar, especially when they are located below thick clouds with large particle sizes. Further, the uncertainty of CloudSat radar observations tends to be larger below 1-km height owing to signal reflections from the surface. Note that the “cloud occurrence”, by definition, may increase with grid size, which is the 24-km grid resolution of WRF in this case, not the footprint resolution of the satellite observations. With the WSM6 scheme, the mean cloud amount is smaller than that of the Morrison scheme at every level, for both measures, showing small cloud fractions (Fig. 10b) less than 20% throughout the troposphere, even near the surface.

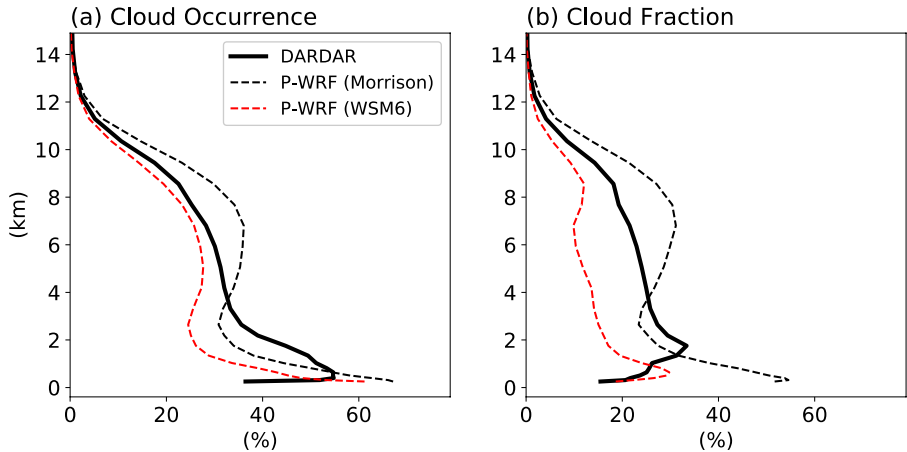


Figure 10. Mean vertical structures of the cloud amounts in the DARDAR cloud data (solid) and the collocated Polar-WRF simulations (dashed). Different definitions of the cloud amount were used. They were defined as 1 if cloud existed in a WRF grid (a), or as the ratio of cloudy pixels within a collocated WRF grid for the DARDAR, and the “cloud fraction” value provided by the model output (b). Black dashed lines represent the Polar WRF simulations with the Morrison scheme and red dashed lines for the WSM6 scheme.

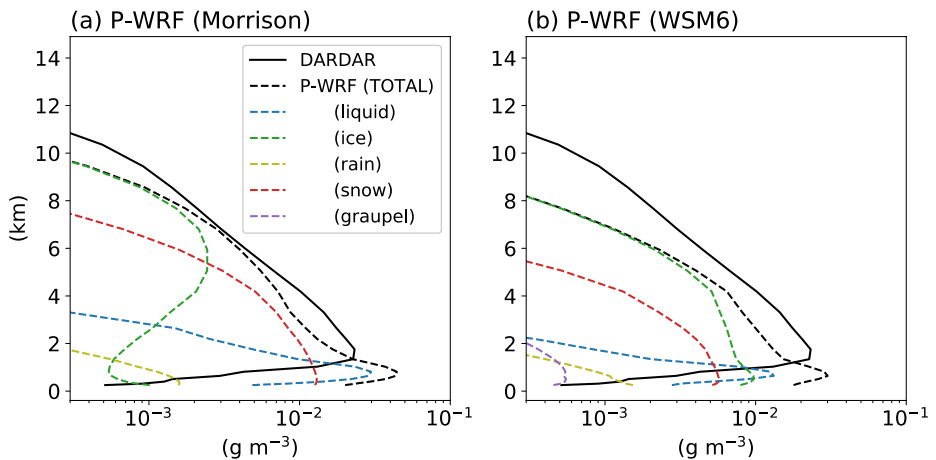


Figure 11. Mean vertical structures of the ice water content in the DARDAR cloud data (solid) and the cloud water content for each hydrometeor in the collocated Polar-WRF simulations (dashed). The Morrison scheme (a) and the WSM6 scheme (b) were used for the cloud microphysics in the Polar-WRF simulations.

4.1.3. Optical properties

Figure 11 shows the vertical structures of the mean cloud water content in the DARDAR cloud dataset (solid line) and the Polar WRF simulations (dashed line). The entire collocated dataset including the data over cloud-free areas was used to quantify the mean structure. Note that only ice-phase cloud particles are considered in the DARDAR retrievals (Delanoë and Hogan, 2008, 2010). The cloud water contents of each hydrometeor in the Polar WRF simulations are illustrated with colored dashed lines; blue for liquid, green for ice, yellow for rain, red for snow, and purple for graupel; the Morrison scheme is shown in Fig. 11a and the WSM6 scheme is shown in Fig. 11b. The magnitude of the total cloud water contents in the Polar WRF simulation shows good agreement with the satellite observations, especially when the Morrison scheme was used. However, the magnitude was slightly smaller above 2 km and larger below 2 km. The major hydrometeor categories in the Polar WRF simulations were ice, snow, and liquid. Despite the cold air temperature, it was noted that liquid-phase clouds were the most dominant type beneath about 1.5 km. Supercooled- or mixed-phase clouds are frequently found in the scene type retrievals in the DARDAR datasets, as many modelling and observational studies have noted the existence of liquid-phase Arctic clouds in the form of a mixed-phase or supercooled liquid water (McFarquhar et al., 2007; Morrison et al., 2003; Pinto, 1998; Shupe et al., 2006). The larger cloud water contents in the Polar WRF simulations than in

the satellite retrievals below 2 km (black solid lines in Figs. 11a and 11b) may be partly because only the ice-phase clouds are considered in the DARDAR retrieval algorithm. While both the ice and the snow are frozen hydrometeors, snow is the dominant category when the Morrison scheme is used (red dashed line in Fig. 11a) and the ice cloud is dominant when the WSM6 scheme is used (green dashed line in Fig. 11b).

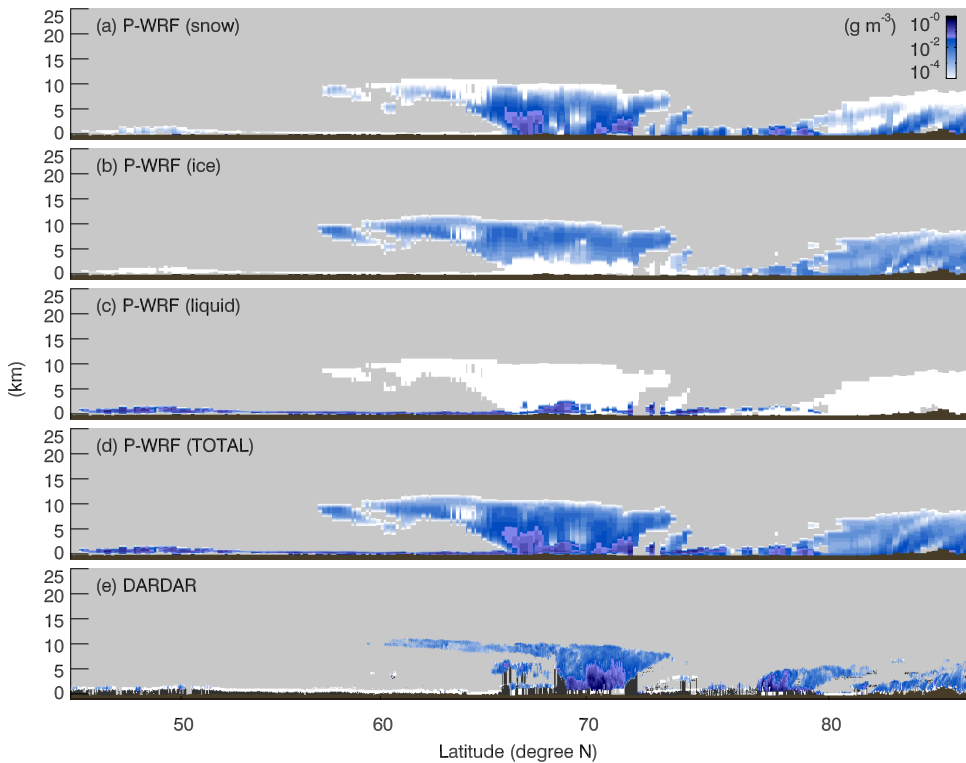


Figure 12. Cloud water content of snow (a), ice (b), liquid (c), and for all hydrometeors (d) from the Polar WRF simulation with the Morrison scheme, and the ice water content from the DARDAR cloud data (e) along an A-train track around 10 UTC, December 25, 2015. The color scale is the log10 of the cloud water content.

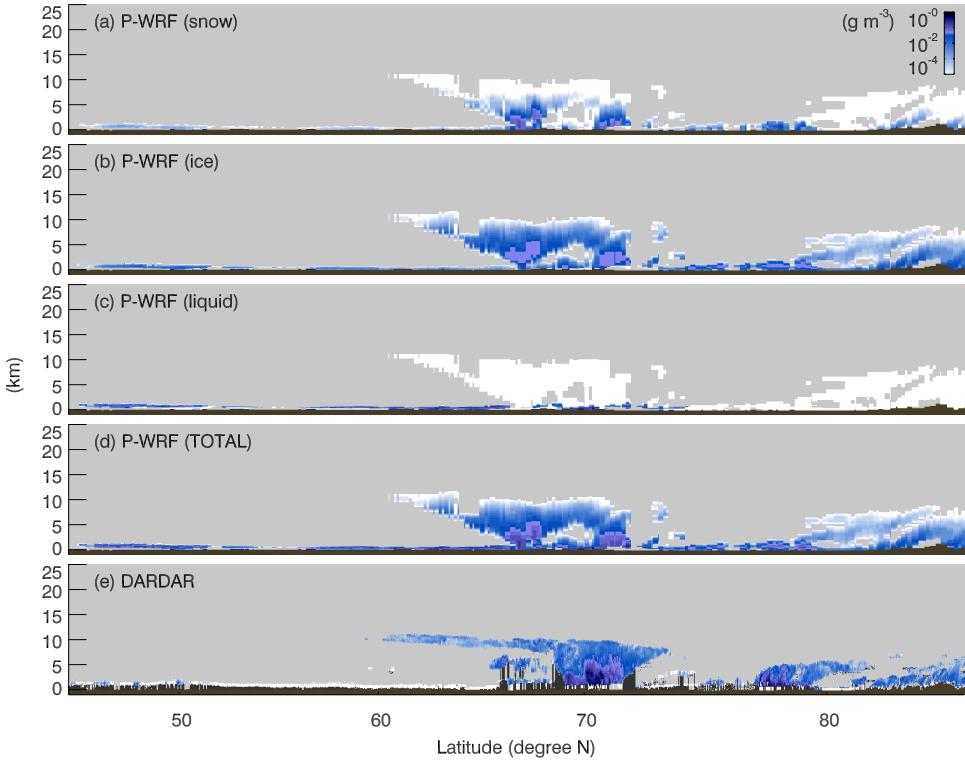


Figure 13. Same as Figure 12 but for the WSM6.

The overall characteristics of the cloud water contents for each hydrometeor can be more closely revealed by examining a representative case. Figures 12 and 13 show the vertical structure of cloud water contents along the satellite track around 10 UTC, December 25, 2015, compared to the collocated Polar WRF simulations with the Morrison scheme (Fig. 12) and the WSM6 scheme (Fig. 13). The upper three sub-figures show the most dominant hydrometeors; snow, ice, and liquid (Figs. 12a–12c and Figs. 13a–13c). The fourth is the summed cloud water content in the Polar WRF simulation (Figs. 12d and 13d) and the last one is the ice water content

retrievals from the DARDAR cloud dataset (Figs. 12e and 13e). The white-to-blue color gradient shows the cloud water contents where clouds are detected. Gray and dark brown colors correspond to cloud-free and surface areas, respectively. Along the entire track, near-surface stratus clouds were found for both the DARDAR observations and the WRF simulation. In the DARDAR observations, the ice water contents of the stratus clouds were very small (white areas) up to the south of around 65° North, as shown in the mean vertical profile in Fig. 11 (black lines below 1 km). This was also true for the WRF simulation showing that the clouds over that area mostly consisted of liquid-phase water (Figs. 12c and 13c). In the vertically extended cloud around 70° North, near-surface level clouds were in liquid-phase (Figs. 12c and 13c), and above that, the deep clouds consist mostly of ice for the Morrison scheme (Fig. 12b) and of snow for the WSM6 scheme (Fig. 13b). The deep clouds around 85° North showed a similar structure but without the near-surface liquid-phase layers. In the low-level clouds around 75° North, the Morrison scheme simulated larger liquid water contents at the tops of the clouds than below (Fig. 12c). This mixed- or supercooled-phase cloud layer on top of the ice-phase cloud is an observed feature of Arctic clouds (e.g., McFarquhar et al., 2007) that is also found in the cloud phase retrievals in the DARDAR dataset (*figure not shown*).

The different cloud characteristics of the WSM6 scheme compared to the Morrison scheme in Fig. 11 can also be seen by comparing Figs. 12 and 13.

Unlike with the Morrison scheme, the water content of the ice cloud in the WSM6 scheme is larger than that of snow in most of the clouds along the satellite track (Figs. 13a and 13b). Liquid-phase water in the WSM6 scheme (Fig. 13c) is not as dominant as with the Morrison scheme in the surface-level stratus and the liquid-phase cloud layer on top of the ice-phase cloud at around 75° North was not simulated in the WSM6 scheme. The high-level ice clouds at a 10-km altitude around 60° North have large horizontal extensions. These cover larger areas with the Morrison scheme (Fig. 12d) than the DARDAR cloud retrievals (Fig. 12e), but are smaller with the WSM6 scheme (Fig. 13d). This difference in high cloud coverage may contribute to the differences in the cloud top height among them. Morrison has the highest, followed by DARDAR, and WSM6 was the lowest (Table 4). In the cloud fraction at the upper troposphere above 4 km, The Morrison scheme was also the largest, followed by DARDAR, and the WSM6 scheme was the smallest (Figs. 10a and 10b).

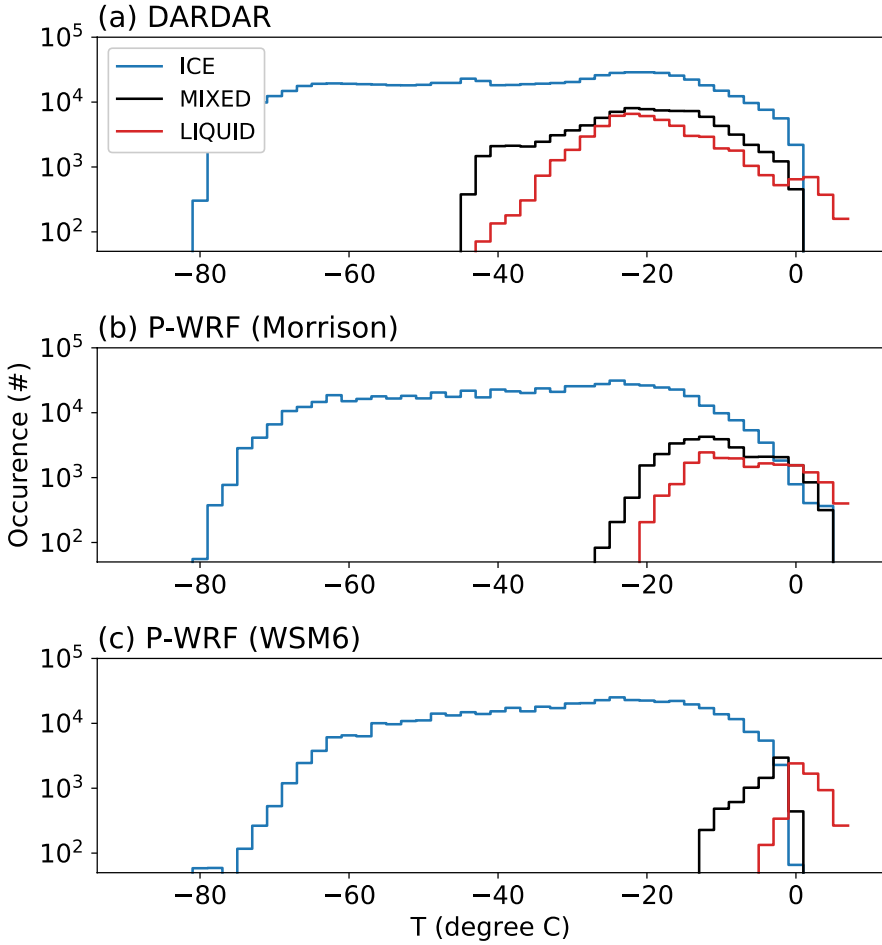


Figure 14. Number of points for each thermodynamic phase of clouds (liquid- or rain-phase: red, frozen-phase: blue, and mixed-phase: black). The dataset is binned into the air temperature intervals of 2°C . The numbers are counted for each WRF horizontal grids and are scaled to correspond to the 60-m height resolution of the DARDAR retrievals.

Information on the particle phase of clouds is illustrated in Fig. 14. As the DARDAR cloud dataset assigns a cloud at each level as one of “ice”, “ice+supercooled”, “liquid warm”, and “supercooled” cloud categories, the number of levels for each category was summed. The “MIXED” in the figure

means the number of observation points of the “ice+supercooled” category. “LIQUID” means the total number of observation points of the “liquid warm” and “supercooled” categories (Fig. 14a). For the Polar WRF simulations (Figs. 14b and 14c), a WRF grid at each level is counted as “LIQUID” if it contains only liquid or rain particles, and as “ICE” if it has only frozen particles. “MIXED” means it contains both clouds phases. Considering the vertical resolution of the simulations, the counts of WRF points are scaled to correspond to the DARDAR height resolution. Using the air temperature compiled in the DARDAR dataset and that from the WRF simulations, the data were binned into air temperature intervals of 2 °C. In the DARDAR cloud retrievals, “LIQUID” or “MIXED” phase clouds (red and black lines in Fig. 14a) were frequently detected and they account for about 40% of cloud observations at –20 °C. Arctic liquid-phase clouds are known to exist at temperatures greater than –40 °C, mostly below 3 km altitude (Shupe, 2011). The Morrison scheme (Fig. 14b) simulated more liquid-phase clouds than the WSM6 scheme (Fig. 14c) which is consistent with the mean cloud water contents profile of each hydrometeor in Fig. 11. For the Morrison scheme, as the temperature increases above –10 °C, the amount of mixed-phase clouds become significant, which is the case for the WSM6 scheme only over the warm atmosphere with a temperature above 0 °C. On the other hand, at temperatures below –20 °C, both the Morrison scheme and WSM6 scheme produced a significantly smaller amount of liquid or rain particles than frozen

particles.

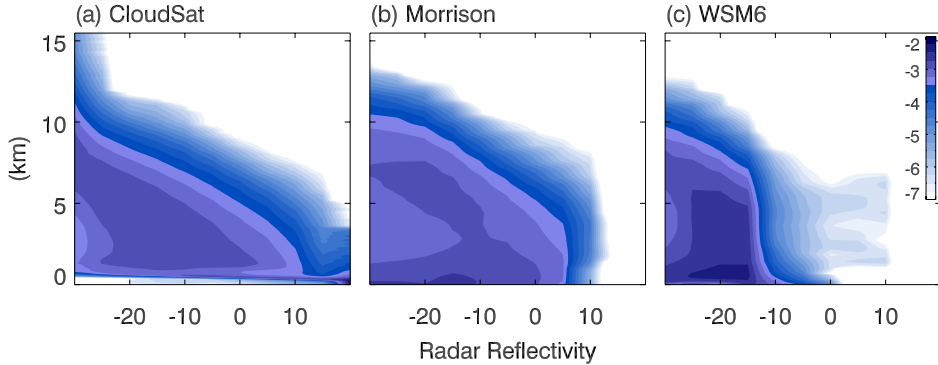


Figure 15. Joint probability density function (PDF) of the CloudSat radar reflectivity and height (a). Polar WRF simulations with the Morrison scheme (b) and the WSM6 scheme (c) were converted to “satellite-like” radar reflectivity using the COSP package to obtain the joint PDF. The color scale is the \log_{10} of the joint PDF.

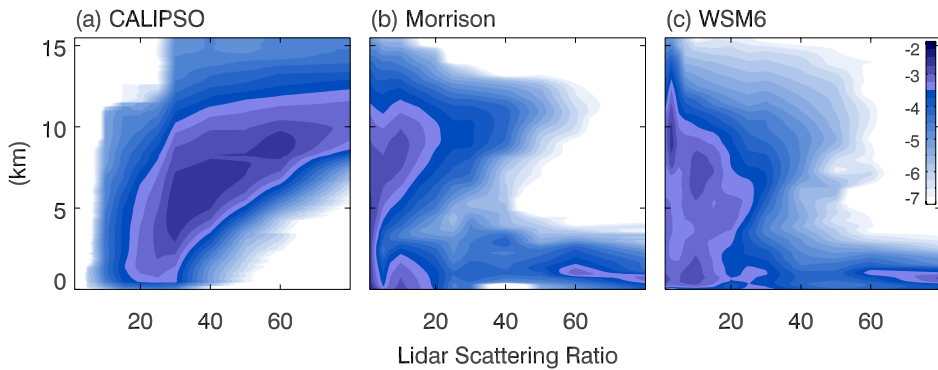


Figure 16. Joint PDF of the CALIPSO lidar scattering ratio and height (a). Polar WRF simulations with the Morrison scheme (b) and the WSM6 scheme (c) were converted to “satellite-like” lidar scattering ratio using the COSP package to obtain the joint PDF. The color scale is the \log_{10} of the joint PDF.

Figure 15a shows the joint histogram of the CloudSat radar reflectivity and height. Figures 15b and 15c were obtained in the same manner, but for the simulated satellite-like radar reflectivity based on the Polar WRF model simulations using the Morrison scheme and the WSM6 scheme, respectively. The simulated radar signals were produced by the radar simulator compiled in the COSP package (Bodas-Salcedo et al., 2011). The observed CloudSat signal histogram (Fig. 15a) shows a monotonic decrease in the reflectivity with altitude that implies that the clouds are thick near the surface and gradually get thinner above. On the other hand, in the COSP simulation results (Figs. 15b and 15c), the occurrence of relatively strong radar signals at about 1 to 3 km also appears near the ground. A notable difference between CloudSat and the Polar WRF is that, below 5 km, strong reflectivity signals larger than 10 dBZ are frequently observed from CloudSat (Fig. 15a), while the radar simulator results based on the Polar WRF simulations are clustered mostly at much weaker reflectivity (Figs. 15b and 15c). When the satellite retrievals of cloud water contents were directly compared to the modelled cloud water contents (Fig. 11), both the Morrison scheme and WSM6 scheme resulted in underestimations of cloud water contents near the surface below about 1 km. This further suggests that the small cloud water content retrievals from CloudSat near the surface could be unreliable, thus Polar WRF's overestimation of cloud water contents below 1 km may not be large as Fig. 11 showed.

The joint histogram of the lidar scattering ratio and height (Fig. 16) highlights the discrepancy between the observation and the Polar WRF simulation. The lidar signal below 5 km is much more prominent in the lidar simulations based on the Polar WRF output than in the CALIPSO observations. For the CALIPSO observations (Fig. 16a), the high occurrence cluster of the joint histogram is centered on the weaker signal at the low-level and the stronger signal at the upper-level. This was not the case for the Polar WRF model simulations where the strong lidar scatterings were simulated near the surface level using both cloud microphysics schemes. The weak low-level signal in the CALIPSO observations occurs because the lidar signal is easily attenuated by the large droplets between the target and the sensor. Since it is highly probable that thick low-level cloud accompanies a thick mid- to high-level cloud (Oreopoulos et al., 2017), the occurrence of strong lidar scattering near the surface tends to be less frequent. In contrast, a stronger near-surface lidar scattering is expected from the Polar WRF simulations (Figs. 16b and 16c). It seems that, unlike the CALIPSO observations, the modelled upper-tropospheric clouds were not thick enough to block out the near-surface signals. Similar characteristics were observed in the vertical structure of the modelled cloud water content (Fig. 11) that is smaller than the satellite retrievals above 9 km for the Morrison scheme by about 1 g m^{-3} , and above 5 km for the WSM6 scheme by about 5 g m^{-3} . Therefore, the satellite lidar may have more opportunity to observe the low-level clouds without the

signals being attenuated. Moreover, near the surface, the cloud water content of the Polar WRF is an order of magnitude larger than that of the satellite retrievals. With the Morrison scheme, strong lidar scattering signals above 8 km were more frequently simulated, and the vertical extension of the strong lidar scattering signal near the surface was higher than with the WSM6 scheme.

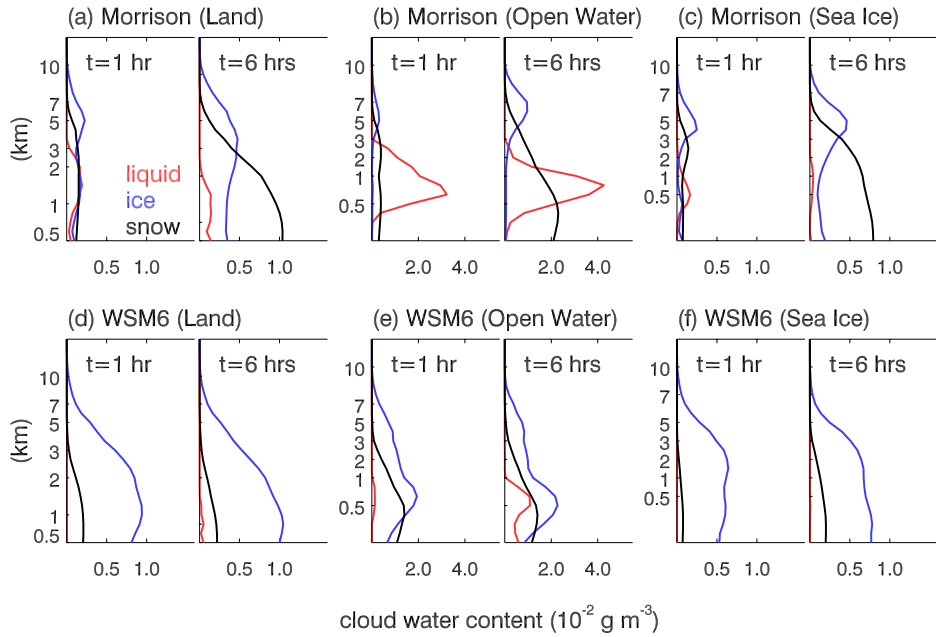


Figure 17. The mean vertical structures of water contents of liquid (red), ice (blue), and snow (black) clouds with the Morrison scheme (a, b, and c) and WSM6 scheme (d, e, and f) at 1 hour and 6 hours Polar WRF model integrations initialized at 00 UTC, 24 December 2015. The areas with latitudes higher than 70° N were used, and divided into land surface (a, d), open water (b, e), and sea-ice area (c, f).

4.1.4. Microphysical processes

In order to examine which microphysical processes are responsible for the differences in the vertical profiles of cloud condensate between the Morrison and WSM6 schemes, the initial developments of the microphysical properties were investigated. Figure 17 displays the mean vertical profiles of cloud water contents for liquid (red), ice (blue), and snow (black) at 1 hour and 6 hours after the model was initialized at 00 UTC, 24 December 2015. Because a cloud data assimilation was not used for the initial conditions, all cloud variables are initialized as zero. As it took about 4 to 5 hours for the surface precipitation to reach a stable value, 6 hours was deemed sufficient to examine the outcome of the initial development and short enough to minimize the effects of changing weather conditions. A marked difference between the two schemes is that the Morrison scheme (Figs. 17a–17c) shows significant changes in the hydrometeor composition during the initial 6-hour integration, while the WSM6 scheme (Figs. 17a–17c) maintains the characteristics of the very early stage with the ice condensate being the dominant category. For the Morrison scheme, liquid clouds quickly developed below about 3 km and continued to build up over open ocean areas (Fig. 17b) but diminished with time over sea-ice areas (Fig. 17c). While ice condensates show small increases (blue lines in Figs. 17a and 17c), snow condensates increased greatly (black lines in Figs. 17a–17c), becoming the dominant category in the lower troposphere. In addition, only over open sea areas (Fig. 17e), the

WSM6 scheme produced enough liquid-phase clouds in the lower troposphere to have cloud water contents comparable with frozen-phase clouds.

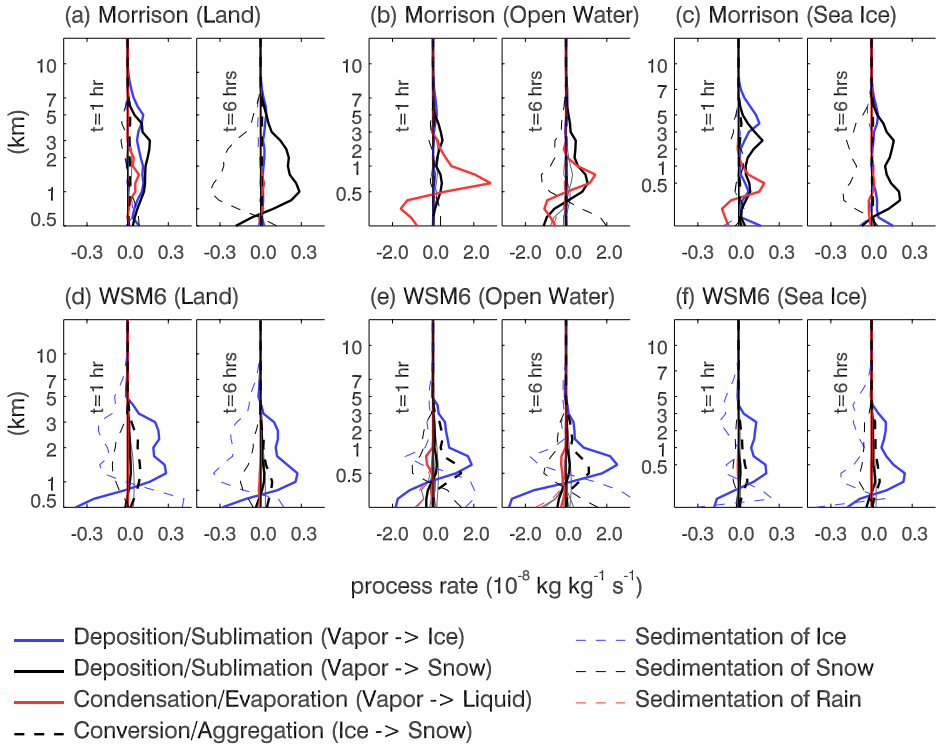


Figure 18. The mean vertical structures of major cloud microphysics process rate terms at 1 hour and 6 hours Polar WRF model integrations initialized at 00 UTC, 24 December 2015 when the Morrison scheme (a, b, and c) and WSM6 scheme (d, e, and f) are used. All the other terms not listed in the legend are plotted in gray lines. The areas with latitudes higher than 70° N were used, and divided into land surface (a, d), open water (b, e), and sea-ice area (c, f).

Figure 18 depicts the process rate terms in the cloud microphysics schemes which contribute to the tendency terms of each hydrometeor. The analyses were done with the same simulation set used for Fig. 17. With the Morrison

scheme (Figs. 18a–18c), the shapes of process terms at 1-hour integration are not similar to those at the 6-hour integration, while the WSM6 scheme (Figs. 18d–18f) maintains features of the early stage during the first 6 hours. This is consistent with the vertical profiles of cloud condensate compositions in Fig. 17. In the mean sense, at the time after 1-hour model integration, the cloud mixing ratio below 1 km is larger with the WSM6 scheme than that with the Morrison scheme (left-sides of Figs. 17a–17f). Then, due to the stronger sedimentation of the WSM6 (thin dashed lines in Figs. 18d–18f), the cloud mixing ratios become smaller than with the Morrison scheme (right-sides of Figs. 17a–17f).

The most dominant processes for cloud particle growth are associated with the atmospheric water vapor. Note that the vertical velocity differences are very small between the simulations with the two cloud microphysics schemes. For the Morrison scheme over the land surface and sea-ice, the deposition of water vapor by ice/snow particles (thick blue/black lines in Figs. 18a and 18c) dominates the process at 6-hour integrations. This explains the abundance of frozen particles in the lower- and mid-level troposphere (blue/black lines in Figs. 17a and 17c). As the Morrison scheme shows large liquid water contents at about 1 km height over the open ocean area (red line in Fig. 17b), the condensation of water vapor to form liquid clouds shows a strong production rate at the same level (red line in Fig. 18b). At levels near the surface, the growth of ice and snow condensates over land surface and open ocean areas

is due mainly to the sedimentations of ice and snow particles (dashed blue/black lines in Figs. 18a, 18b, 18d, and 18e), probably originating from upper levels. On the other hand, over the sea-ice, the water vapor deposition process is strong even at near-surface levels (thick blue line in Fig. 18c), which is not the case for the WSM6 scheme (Fig. 18f). The simulations with the WSM6 shows simple vertical structures of cloud water content for all surface types: the ice category dominates in most situations (Figs. 17d–17f). They showed a strong deposition process, similar to the Morrison scheme, except that it is the deposition by ice condensate in this case (red lines in Figs. 18d–18f). Another notable feature of the WSM6 scheme is the strong aggregation of ice by snow particles at levels below about 3 km (thick black dashed lines in Figs. 18d–18f), while the production of low-level snow particles in the Morrison scheme originates mainly by sedimentations from upper-levels. Below about 1 to 2 km, sedimentations from upper-levels evaporate to influence the atmospheric humidity which, as a result, is slightly (about 1 to 2%) larger with the Morrison scheme (*figure not shown*). Although small, this might further amplify the differences in the cloud hydrometeor masses between the microphysics schemes even in 48-hour simulations. In addition, at the upper-level troposphere over land surface and sea-ice areas, the WSM6 scheme's ice/snow sedimentations were stronger than the deposition processes, which is not the case with the Morrison scheme. The strong sedimentations seem to contribute to the lower cloud-top heights with

the WSM6 scheme than the Morrison scheme. The changed ice sedimentation may be due to the modified ice process proposed by Hong et al. (2004) which is also implemented in the WSM6 scheme.

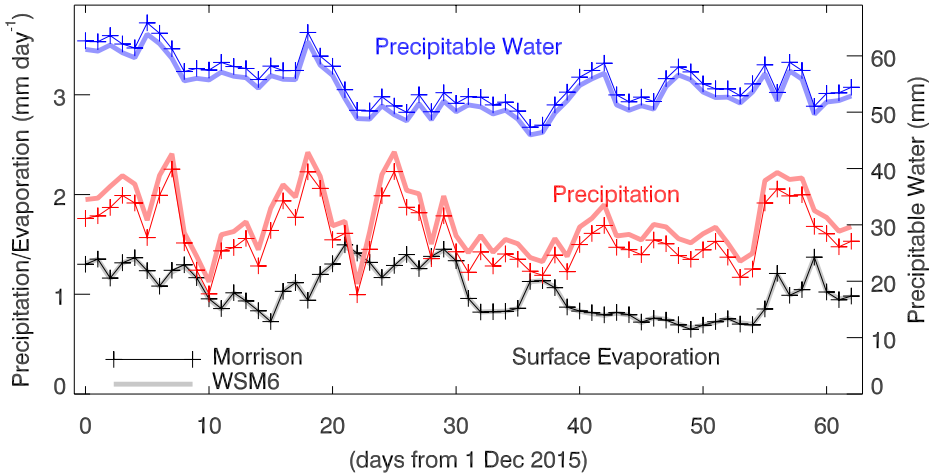


Figure 19. Time series of the daily mean surface evaporation (black), precipitation (red), and precipitable water (blue) from the Polar WRF simulations. The Morrison scheme (marked thin lines) and the WSM6 scheme (thick lines) were used for the cloud microphysics in the simulations. The values were obtained by averaging over the entire simulation domain.

4.1.5. Atmospheric water budget

Because the two Polar WRF simulation setups were identical except only for the cloud microphysics scheme, the differences in the outgoing longwave radiation at the TOA (OLR) and the DLR at the surface should be somewhat related water processes. The water budget within a finite domain is a balance between the water flux at boundaries and surface precipitation once the tendency in the domain can be ignored. Figure 19 shows the time series of the

daily mean surface evaporation (black lines), surface precipitation (red lines), and precipitable water in the atmosphere (blue lines) for the Morrison scheme (marked thin lines) and for the WSM6 scheme (thick lines). The values were obtained by averaging over the entire simulation domain. While the surface evaporation, even when the surface temperature is prescribed, can be different between the two schemes due to the differences in the near-surface humidity or wind speed, the difference turned out to be negligible (black lines in Fig. 19). On the other hand, the domain-averaged precipitation at the surface (red lines in Fig. 19) was significantly stronger with the WSM6 scheme by about 10% of the total precipitation. The blue lines in Fig. 19 are the times series of the domain-averaged total precipitable water. It shows a more humid atmosphere with the Morrison scheme than with the WSM6 scheme. This, along with the larger cloud water contents (Figs. 11, 12, and 13), gave rise to a thicker atmospheric thermal emissivity with the Morrison scheme than with the WSM6 scheme. Intuitively, the stronger precipitation processes in the WSM6 scheme seem to result in a drier atmosphere and less cloudy sky.

In addition, the surface turbulent latent heat flux was slightly larger with the Morrison scheme than with the WSM6, only over the ice-free Atlantic Ocean. This is related to the slightly more humid near-surface atmosphere with the WSM6 over the same region when compared to with the Morrison scheme. The smaller relative humidity from the Morrison scheme may be a result of the warmer near-surface air temperature due to larger surface

warming effects from thicker clouds with the Morrison scheme than with the WSM6 scheme. Similarly, the stronger surface warming effect by the thicker clouds from the Morrison scheme results in the larger turbulent sensible heat flux from the surface than that with the WSM6 scheme. However, over the open-ocean areas, the WSM6 scheme produces slightly larger surface sensible heat flux than the Morrison scheme because the sea surface temperature was predefined as a surface boundary condition so it does not respond to forcings.

4.1.6. Longwave flux

The cloud influence can be exerted most effectively by altering radiative fluxes at the TOA or the surface, especially during the wintertime over the Arctic region where the effects of convection or the precipitation are smaller than any other regions or seasons. Furthermore, the clouds have the largest effect on the temporal and spatial variabilities of the radiative flux at the TOA than any other physical element because the surface-to-tropopause lapse rate easily exceeds the equator-to-pole temperature gradient. Figure 20a shows the averaged OLR field of the CERES observations during the two-month period. Within the Polar WRF simulation domain, the Greenland region exhibited the smallest OLR. The Arctic Ocean area that was covered with sea-ice and the northern part of East Siberia had OLRs smaller than 180 W m^{-2} . There were sharp contrasts in the OLRs along the sea-ice edge north of the Barents-Kara

Seas and north of the Chukchi Sea where the warm water intrusions from the Atlantic Ocean and the Pacific Ocean occur.

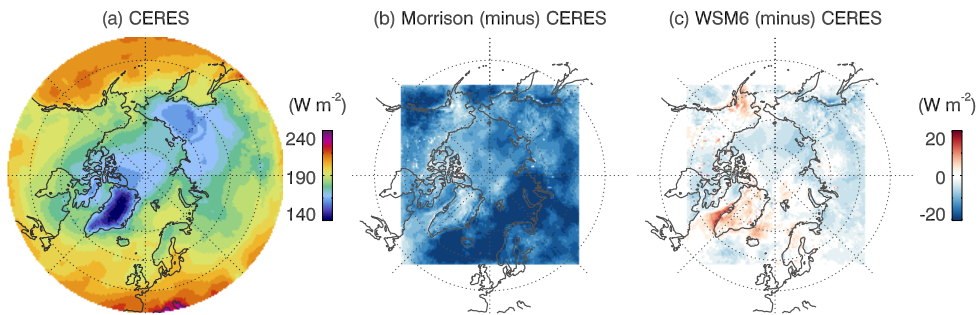


Figure 20. Mean outgoing longwave radiation at the top-of-atmosphere (OLR) from the CERES observations (a), and the mean differences in the OLR between the Polar WRF simulations and the CERES observation. The Morrison scheme (b) and the WSM6 scheme (c) were used for the cloud microphysics in the simulations.

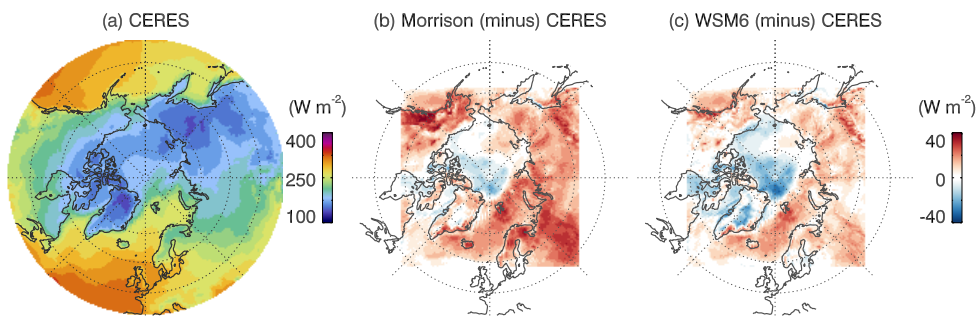


Figure 21. Mean downward longwave radiation (DLR) at the surface from the CERES dataset (a), and the mean differences in the OLR between the Polar WRF simulations and the CERES dataset. The Morrison scheme (b) and the WSM6 scheme (c) were used for the cloud microphysics in the simulations.

Figures 20b and 20c indicate the simulated mean OLR bias fields to the CERES observations (Fig. 20a) when the Morrison scheme (Fig. 20b) and the

WSM6 (Fig. 20c) was used. The remarkable difference is that, with the Morrison scheme, the OLR exhibited a negative bias almost everywhere in the simulation domain that would act to warm the Earth's atmosphere and surface. Since WRF's sea surface temperature is prescribed as an observed value, a larger cloud thickness, a higher cloud top height, and/or a more humid atmosphere than the observations are expected in the simulation with the Morrison scheme. Note that the modelled dynamics fields did not show significant differences between the simulations with the two schemes that might cause the differences in the cloud or radiative flux. The bias was largest over the open ocean areas of the Atlantic and Pacific Oceans where the surface is warmer and the atmosphere is more humid containing more cloud water. On the other hand, with the WSM6 scheme, the overall OLR bias was a lot less than with the Morrison scheme. Like the case of the Morrison scheme, the OLR over the Arctic sea-ice region showed negative bias to observations, but with a smaller magnitude. However, it showed a positive bias over the Atlantic sector of the Arctic Ocean where the Morrison scheme gave rise to a strong negative bias. The region's large OLR difference between the two schemes' simulations is due to the warm surface temperature over the Atlantic open sea that can create large changes in the OLR by relatively small differences in the cloud and/or atmospheric water vapor. Other than that, the mean difference in the OLR between the two schemes was spatially systematic with about a 10 W m^{-2} weaker thermal out-going

radiation in the Morrison scheme. This is consistent with the result that the Morrison scheme produced a more humid atmosphere and clouds with larger thickness and higher cloud top than the WSM6 scheme.

The DLR at the surface is more relevant to the surface weather and climate of the Arctic Ocean and it is directly involved in the cloud radiative effects to the sea-ice variability. Having only the downwelling component, the DLR is determined by the vertical profiles of atmospheric temperature and thermal emissivity which is a strong function of cloud and atmospheric water vapor. Because radiative flux at the Earth's surface cannot be measured from satellites, it is typically parameterized using radiative transfer calculations and available information on the atmospheric profiles. The procedure and accuracy of the longwave model in the CERES SSF surface dataset are reported in Kratz et al. (2010). For both the Morrison and the WSM6 schemes, the simulated DLR was stronger than the CERES parameterization except for the weaker DLR over the Arctic Ocean areas with large sea-ice concentrations (Fig. 21). Figures 21b and 21c show the mean bias fields to the estimated DLR in the CERES dataset (Fig. 21a) when the Morrison scheme (Fig. 21b) and the WSM6 scheme (Fig. 21c) was used. The positive bias in the DLR over the Atlantic sector of the Arctic Ocean is important, especially over the Barents and Kara Seas. This acted to enhance the surface temperature gradient across the sea-ice edge. As the CERES dataset reveals, the mean DLR is larger over the open ocean and smaller over the sea-ice, which reflects that the

different climates of the regions: a warmer and more humid atmosphere with thicker clouds over the open ocean than over the sea-ice. This gradient across the sea-ice edge seems to be overestimated in the model simulations with the two cloud microphysics schemes. Note that the mean DLRs were systematically stronger with the Morrison scheme than with the WSM6 scheme everywhere within the simulation domain, but the magnitude of the difference was smaller over the open ocean but larger over the sea-ice or land surfaces.

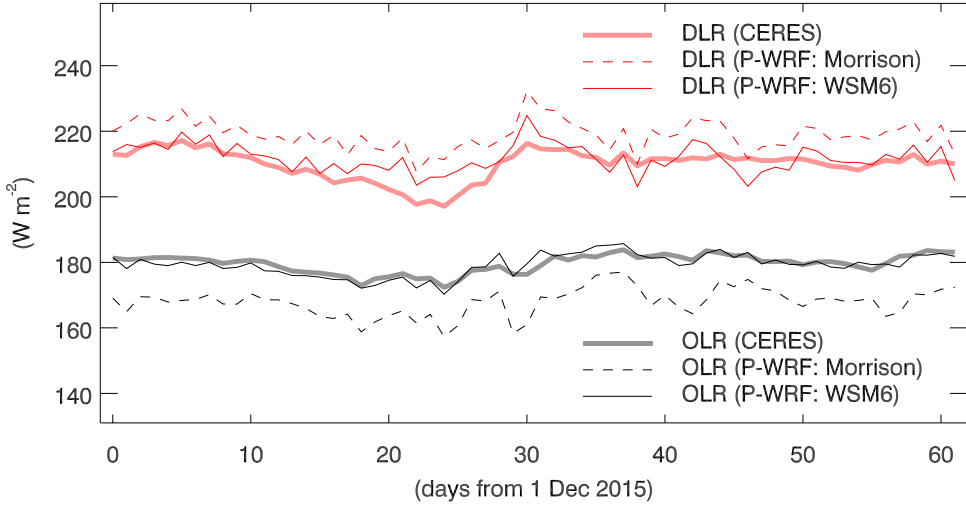


Figure 22. Time series of the daily mean OLR (black) and DLR (red) from the CERES dataset (thick solid lines), and the Polar WRF simulations with the Morrison scheme (dashed lines) and the WSM6 scheme (thin solid lines). Only values of the Polar WRF at nadir points of the CERES satellite were used.

Figure 22 depicts the time series of the daily mean OLR (black) and DLR (red) from the CERES satellite dataset (thick solid lines), and the Polar WRF

simulations with the Morrison scheme (dashed lines) and the WSM6 scheme (thin solid lines). Only values of the Polar WRF grid at nadir points of the CERES satellite were used. While the intra-seasonal variation of the observed longwave flux was well captured in the simulations, the day-to-day variation of the DLR seemed to be muted with the WSM6 scheme, showing a smaller correlation coefficient with the observation than that with the Morrison scheme (Table 5). This suggests an under-estimation in the cloud variations by the WSM6 scheme. On the other hand, the amounts of both the OLR and DLR from the WSM6 scheme were remarkably close to the observations than those of the Morrison scheme (Table 5), making it difficult to determine which scheme best matched observations. It is noted that the mean DLR changes are larger than 7 W m^{-2} with only the cloud microphysics scheme switched. Karlsson and Svensson (2013) reported the inter-model spread in the radiative effect of Arctic clouds among current coupled climate models, and during the winter season, the differences in the surface cloud forcing between models did not exceed 20 W m^{-2} . The results suggest that a significant portion of the climate model uncertainty in simulating the Arctic winter climate could originate from the different cloud representations.

Table 5. Correlation coefficients and mean differences (simulation minus satellite retrieval) in the outgoing longwave radiation at the top-of-atmosphere (OLR) and downward longwave radiation at the surface (DLR) between the Polar WRF simulations and the CERES satellite dataset. The Morrison scheme and WSM6 were used for the cloud microphysics in the simulations.

		P-WRF (Morrison)	P-WRF (WSM6)
OLR	Correlation Coefficient	0.79	0.87
	Mean Difference	-11.7 W m^{-2}	-0.4 W m^{-2}
DLR	Correlation Coefficient	0.73	0.67
	Mean Difference	9.0 W m^{-2}	1.9 W m^{-2}

The DLR measurements from ground sites were compared to the simulated DLR (Fig. 23). Figure 23 shows the daily mean DLR time series of the observations from the six BSRN sites and of the Polar WRF simulations. Each station's measurement was compared to the time series of the grid where the station is located (Fig. 9). Although the BSRN flux data is a direct observation unlike the estimated values of the CERES DLR, their spatial representativeness should be limited to the location of the station. All stations were located near the coast except for the Toravere station. Generally, simulations near coastal regions are expected to be under the strong influence of the sea surface temperature boundary condition. Also, a strong gradient effect can occur on scales smaller than the grid size, especially at coastlines bordering open seas. With the Morrison scheme, the simulated DLR by the Polar WRF tended to be stronger than the observation of each station.

However, the mean biases to the ground observations were smaller than those to the CERES estimations. On the other hand, when the WSM6 scheme was used, the DLR values were smaller than the ground observations except at the Lerwick and Barrow stations. This contrasts with the fact that the DLR was consistently larger than the CERES estimation everywhere except over the ice-covered sea surfaces. Nevertheless, similar to the mean bias fields of the DLR simulations to the CERES dataset, the DLR values were significantly larger with the Morrison scheme than with the WSM6 scheme at all stations.

Note that, at the four of the six stations that are located near the coast bordering the ice-covered Arctic Ocean, the mean DLR bias to the CERES estimation changes from positive to negative (Figs. 21b and 21c). Therefore, it is challenging to judge the reliability of the estimation by the CERES dataset or the representativeness of the ground station observations. However, at the Lerwick station that is surrounded by the open ocean, the DLR values were significantly larger than both the ground observations and the CERES estimations. Considering the strong effect of the sea surface temperature boundary condition at the near-surface level, the bias is likely in part due to an overestimated cloud thickness and the related cloud radiative forcing.

The fact that the OLR was weaker and the DLR was stronger with the Morrison scheme than with the WSM6 scheme over most of the domain implies that the thermal emissivity of the atmosphere is thicker with the Morrison scheme. Not only the larger mixing ratio of clouds (Fig. 11) but also

the increased amount of liquid-phase particles contribute to the different emissivity between the two schemes' simulations. This results in warming effects on the Earth system by both reducing the out-going radiation at the TOA and increasing downwelling flux to the surface. The domain averaged differences in the OLR and the DLR between the two schemes were about -11 W m^{-2} and 7 W m^{-2} , respectively, and the magnitudes did not change much throughout the entire simulation period. However, over open ocean areas, while the magnitude of the OLR difference was larger, the magnitude of the DLR difference was smaller than over the sea-ice or land surface. Considering that the cloud cover is climatologically smaller over open ocean areas than over sea-ice or land surface areas, the effects of changes in the cloud and/or humidity can be amplified in the OLR and rather muted in the DLR. This is because the OLR responds more sensitively to changes in the clouds over the open ocean where the surface temperature is significantly larger, and the near-surface air surface temperature that strongly affects the DLR is bound to the prescribed sea surface temperature over open ocean areas, while this is not the case over sea-ice or land surface areas.

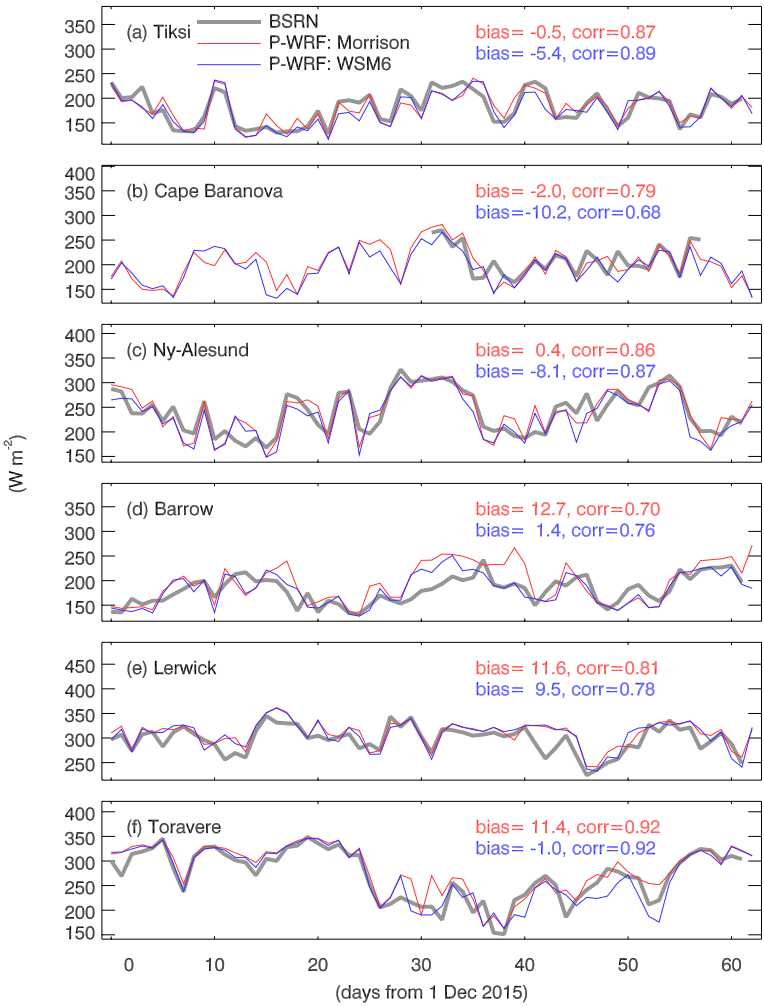


Figure 23. Daily mean time series of the observed DLR (gray) at six BSRN stations: Tiksi (a), Cape Baranova (b), Ny-Ålesund (c), Barrow (d), Lerwick (e), and Tõravere (f); and the simulated DLR with the Morrison scheme (red) and the WSM6 scheme (blue) at the grid where each station was located.

4.2. Cloud responses to the recent Arctic sea-ice change

Based on the accuracy information of modelled clouds, the model is used to investigate how the diminishing winter Arctic sea-ice affects the Arctic clouds. The control simulation was run for 10 winters from 2007/08 to 2016/17. Modelled responses of clouds are examined in the simulations with increased sea-ice concentrations according to the climatological difference to the period 1979/80 to 1988/89.

4.2.1. Recent changes in the Arctic winter season

One of the key differences of the Arctic winter season to other regional climates in the planet is that it experiences polar nights. The lack of solar radiation let the cloud radiative effect have only the longwave warming component (reemitting the terrestrial radiation) but not the shortwave cooling component (scattering solar radiation) both at TOA and surface. Therefore, while the net cloud radiative effect usually has a neutral to a cooling effect to the surface, it can have a surface warming effect during the Arctic winter seasons. The information of cloud can be limited by an availability of sunlight which is necessary for the retrievals of cloud optical properties. Moreover, in situ measurements of cloud particles are rare and expensive during polar night with harsh Arctic environments.

The Arctic surface is warming at a rate more than twice that of the global average (Cohen, 2016; Cohen et al., 2014; Serreze and Barry, 2011; Serreze

et al., 2009). However at least for the Northern Hemisphere winter season (December–February), the Arctic warming is more recent phenomenon: The Arctic winter mean surface temperature has not shown a significant linear trend until the late 1990s, then it started to have a steep warming trend (Comiso, 2012; Comiso et al., 2008; Jun et al., 2016). This is also true for the Arctic sea ice extent which is closely correlated with the surface temperature. From the 1980s through the late 1990s, the Arctic sea ice extent showed a weak increasing or nearly neutral trend, then it began to decline. Similar significant shift also occurred in the long-term trend of Arctic winter cloudiness (Jun et al., 2016), beginning to increase since the late 1990s.

Not only the Arctic sea-ice, but many physical processes involving large-scale atmospheric and oceanic circulations also have experienced significant changes in recent decades. Because of the complex interactions and competitions among these processes, it is difficult to determine how much a physical process is responsible for the cloudiness change. The variations in Arctic sea-ice, oceanic circulations, and atmospheric heat and moisture transports from lower latitudes might affect the winter Arctic clouds, however, their effects can hardly be separated in observational analysis (Kim et al., 2019).

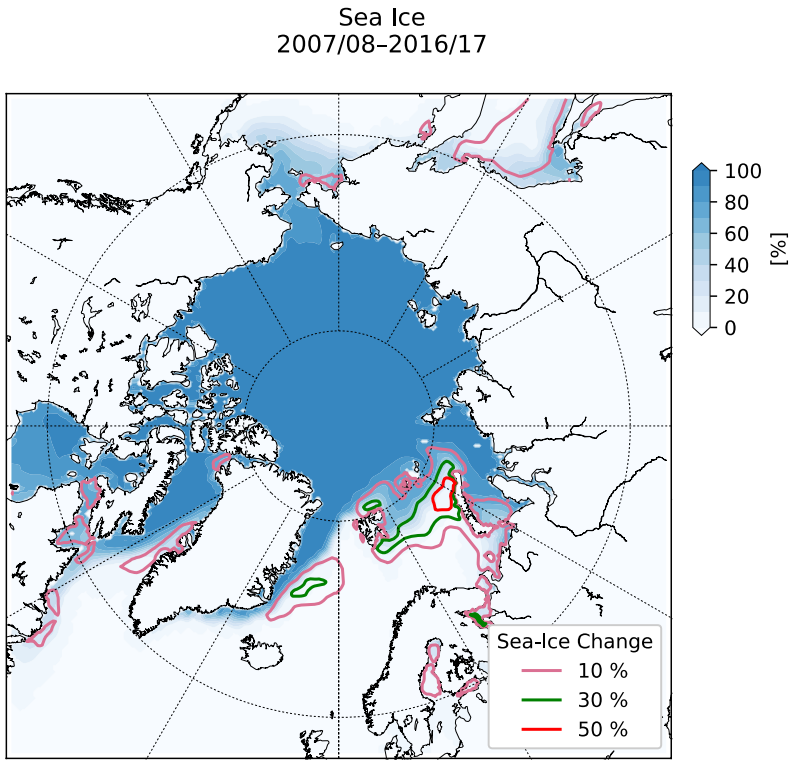


Figure 24. Mean sea-ice concentration during ten winters (December to February) for the period from 2007/08 to 2016/17 (blue shades) and the climatological difference to the period 1979/80 to 1988/89 (contours).

4.2.2. Application of Polar WRF to Arctic cloud research

Numerical model experiments can help to understand the effect from a certain forcing element separately. Simulations with different sea-ice extent information on how the modelled clouds respond to a specific sea-ice change. However, the reliability of a modelling approach can be limited by the model's fidelity in simulating the mean climate especially for problems

involving clouds. Small errors in temperature of surface and atmosphere may result in an unrealistic cloud field because the formation, growth, and thermodynamic phase of clouds are strongly influenced by the altitude of freezing point and the static stability of atmosphere. Uncertainties of cloud simulations by current climate models are known to be larger in polar regions than elsewhere, and the disagreement is largest during the winter season (Chernokulsky and Mokhov, 2012; Karlsson and Svensson, 2011, 2013). This also results in the significant discrepancy of surface longwave radiation among models.

In this part of the dissertation, the Polar WRF model is used to study how the surface forcings that are caused by the recent sea-ice changes affect the Arctic cloud. The same simulation setup with that in Section 4.1 is used which is beneficial because more realistic climatologies of atmospheric variables are expected compared to global model simulations. The control experiment was run for the ten winters (December to February) for the period from 2007/08 to 2016/17 initialized everyday at 00 UTC. The simulations were run for 48 hours and the initial 24-hour outputs were discarded for spin-up. The “high-ice” run is identical with the control run except for the increased sea-ice concentrations according to the climatological difference to the period 1979/80 to 1988/89. In this way, the intraseasonal variabilities in the initial and boundary conditions (including sea-ice) are same for the two experiments so that only the climatological difference in the winter Arctic sea-ice can be

extracted.

4.2.3. Cloud and radiation responses to sea-ice forcing

The “cloud fraction” or “cloud amount” can vary significantly among dataset. Different definitions are used for each satellite, reanalysis, or model dataset. The cloud fraction in models is a diagnostic variable for the purpose of the radiation calculation, thus can be inappropriate for evaluating the model’s performance in comparison with satellite or reanalysis data. Therefore, the column-integrated cloud water content or radiative flux fields are used in the present comparisons. Fig. 25(a) shows the difference in winter mean cloud water path between the periods 1979/80–1988/89 and 2007/08–2016/17 in ERA5 reanalysis. Significant increases in cloud water path are observed in the Arctic Ocean including Barents Sea and Kara Sea, and in high-latitudinal Atlantic Ocean and Pacific Ocean regions namely, Barents Sea, Greenland Sea, Baffin Bay, Hudson Bay, Bering Sea, Okhotsk Sea, and etc. The cloud water has increased most significantly over the area shown large sea-ice reductions such as, Barents Sea, Kara Sea, Greenland Sea, and Okhotsk Sea. Note that in the oceanic regions, a decrease in cloud water path was observed only over the Labrador Sea. Over large areas of Siberia and Alaska, the cloud water has been decreased.

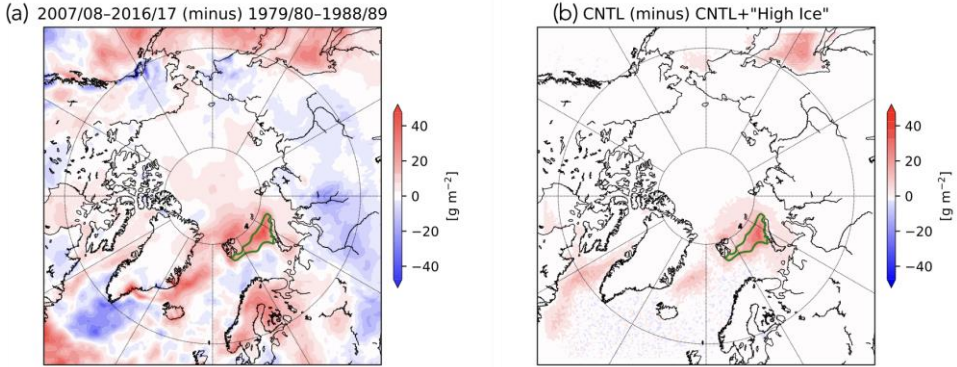


Figure 25. Differences in winter mean cloud water path between the periods 1979/80–1988/89 and 2007/08–2016/17 in ERA5 reanalysis (a), and between control run and “hice ice” run in the Polar WRF’s winter simulations (b). Green contour denotes the area that mean sea-ice amount difference is larger than 30% over the Barents Sea.

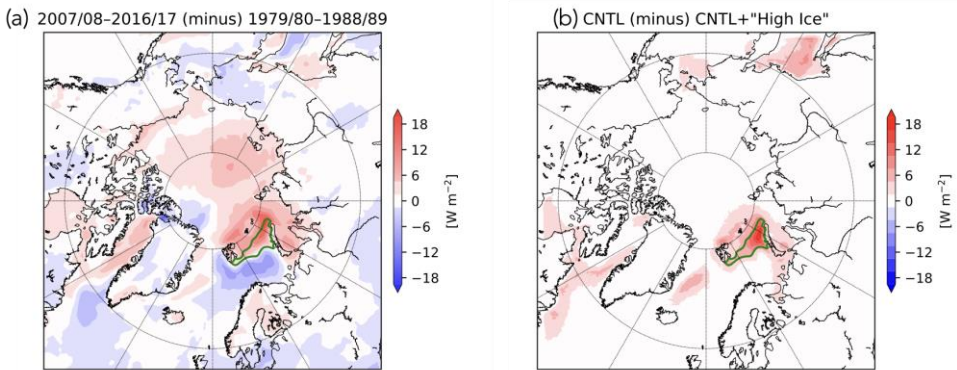


Figure 26. Same as Figure 25 but for the differences in cloud longwave effect at surface.

The cloud water path difference between the control run and high-ice run is shown in Fig. 25(b). The responses of clouds were significant over the regions with large sea-ice changes. Over the Barents Sea that lost more than 30% of sea-ice (green contours in Fig. 24), the mean difference between two

simulations is about 21 g m^{-2} which is 19 g m^{-2} for the difference between two periods in reanalysis field. It is interesting that the small changes in sea-ice ($\sim 10\%$) over the Labrador Sea and Okhotsk Sea resulted in significantly increased local cloud water paths. Unlike the differences in reanalysis field, an increase of cloud water was not simulated. Also, cloud responses were found only over the oceanic areas. This should be noted because 48-hour simulations can be long enough for well-developed cyclones or Arctic snow storms can travel longer than several hundreds kilometers. Although this kind of storms were frequently found during the simulation period, the sea-ice effect on the clouds seem to remain confined to the sea-ice forcing area.

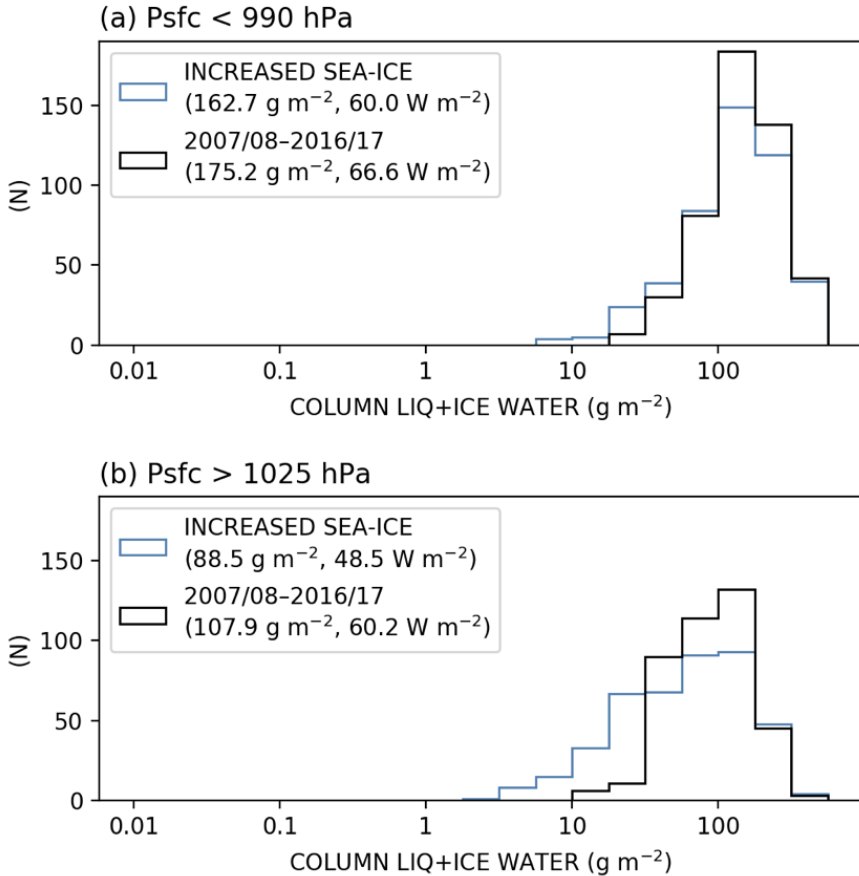


Figure 27. Histograms of column-integrated cloud water path over the Barents sea for the control simulations (black lines) and the high-ice runs (blue lines), when the surface pressure is smaller than 990 hPa (a) and larger than 1025 hPa (b).

Figure 26 depicts the differences in cloud radiative effect at surface. In the reanalysis fields (Fig. 26a), Significant cloud effect changes are found mostly over oceanic areas. The strongest changes are located over the Barents Sea extending further northward. Clouds' surface warming effect has increased over the most of sea-ice covered Arctic Ocean regions. In these areas, clouds

are climatologically thin due to the extremely cold ice surfaces allowing small amount of atmospheric water vapor. Therefore, it seems that the small cloud differences could make large changes in surface longwave radiation. On the other hand, over the Labrador Sea and Okhotsk Sea which have climatological small sea-ice amount and thus large cloud amount, cloud water seems to be sensitive to the underlying sea-ice, however, it did not lead to an large cloud effect change. This is because surface radiative forcing of the thick clouds are already saturated at the thermal wavelengths. Similar responses in cloud radiative effects can be found in the Polar WRF experiments (Fig. 26b), showing stronger differences between the two simulations than between reanalysis fields of two periods. Also, similar to the responses in cloud water path, the strong responses in the cloud radiative effect are also limited near the areas with strong sea-ice changes.

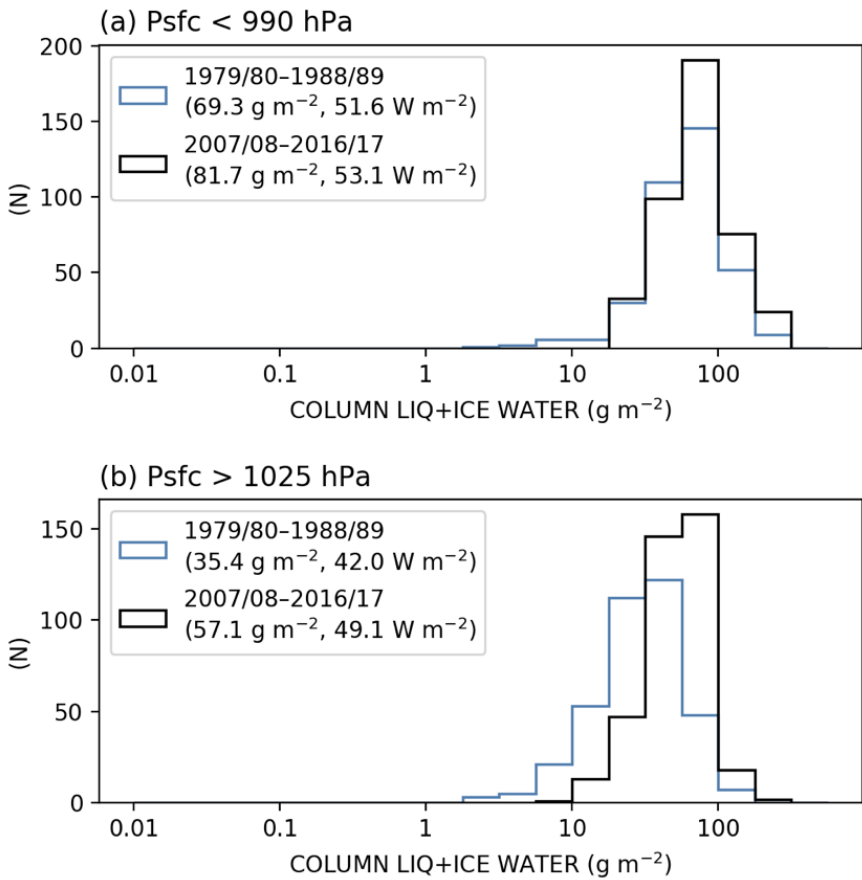


Figure 28. Histograms of column-integrated cloud water path over the Barents sea in ERA5 reanalysis for the period 1979/80–1988/89 (blue lines) and 2007/08–2016/17 (black lines), when the surface pressure is smaller than 990 hPa (a) and larger than 1025 hPa (b).

A closer look into the cloud response to sea-ice change was taken by analyzing time series of area mean values over the Barents Sea area with large sea-ice change ($> 30\%$). Recent observations from the satellite with active sensor reported that (1) low-level clouds and (2) vertically contiguous clouds that extend from the lower troposphere to the upper troposphere are most

frequently observed over the Arctic regions. This is also true for the winter season. The top of low cloud usually located below 1 km from surface. Vertically contiguous clouds show peaks of cloud water contents at about 5 to 7 km and at surface. They also frequently accompanies thin cirrus clouds at about 10 km altitude. The two types of clouds can represent the different surface weather conditions. The low clouds can be observed mostly when the surface is cold and the static stability is large. In contrast, vertically contiguous clouds usually carries warm and moist air from lower latitudes. Therefore, the time series can be decomposed according to surface pressure. Figure 27 depicts the histograms of column-integrated cloud water paths over the Barents sea for the control simulations (black lines) and the high-ice runs (blue lines). When the surface pressure falls (Fig. 27a), clouds tend to extend from the surface to upper-troposphere and the cloud water path is usually large. On the other hand, clouds are located at lower-troposphere and they have smaller amount of water when the surface pressure is high (Fig. 27b). Deep clouds of synoptic-scale storms with low surface pressure showed small responses to the sea-ice changes, while the near-surface clouds with high surface pressure became significantly thinner with the increased sea-ice. It should be noted that the mass of the low-levels clouds are substantially smaller than the vertically contiguous clouds, however, their radiative responses to sea-ice changes are even larger than the vertically contiguous clouds.

The similar analysis with reanalysis data over the Barents Sea is demonstrated in Fig. 28. The cloud differences between the two periods seem to be consistent with those of the modelling experiments. Clouds of low-pressure systems (Fig. 28a) show an increase in cloud water but with a significantly smaller amount than the low-level clouds of high surface pressure conditions (Fig. 28b). Note that the differences in the reanalysis fields between the periods are results of multi-decadal changes in the atmospheric circulation, Atlantic Ocean circulation, and also Arctic sea-ice. On the other hand, although the differences between the two simulations are caused only by sea-ice difference, similar responses in the clouds and their radiative effects were obtained. This implies that the sea-ice reduction is essential in understanding the winter Arctic cloud changes in the last few decades.

5. Concluding remarks

Cloud is one of the largest uncertainty sources in the future climate projection, however, cloud's behavior in response to a changing climate has not been fully understood yet. In the present dissertation, the problems on the cloud feedback were explored. It was demonstrated that, using observations as well as various simulations of the simple energy balance model, the present level of "non-feedback noise" in radiative flux is high enough to prevent reliable estimations of the global radiative feedback. However, a linear analysis of observations revealed that a noise level can be lower in tropics than elsewhere, and that the variations in longwave flux have a larger feedback signal than those in shortwave flux.

Accordingly, longwave radiative flux variations were analyzed over the Pacific warm pool region where the strong convective activities allow an increased radiative feedback signal in OLR variations. As a result, a strong longwave cooling effect of atmosphere was found which is primarily associated with reduced areal coverage of clouds. It should be noted that the longwave feedback in the PWP do not directly indicate climate sensitivity or total cloud feedback on the global scale. As to climate sensitivity, the strong cooling effects of clouds over this region may be reduced once scaled globally. As to total cloud feedback, possible longer-term feedbacks may be present in association with other meteorological elements and large-scale dynamics with

long-term persistence. However, this result can be an observational guideline for the modelling studies of tropical convective clouds.

Another opportunity of understanding regional cloud feedback can be provided by the Arctic polar night condition permitting the clouds have only the longwave warming effect. Although the recent sea-ice decrease has acted as a strong surface forcing, a model experiment is needed for the effect can be separated from others. The performance of the Polar WRF model in simulating Arctic winter cloud was tested in comparison with observations from satellites and ground stations. It was concluded that the Polar WRF can be useful for studying cloud effects on the winter Arctic surface climate as the temporal variation in the simulated surface radiation showed good agreement with surface observations. Accordingly, modelled responses of clouds were examined in the simulations with increased sea-ice concentrations, and it showed significant cloud responses in the areas that have lost winter sea-ice. Also, the responses in the surface longwave flux were large enough to further melt the underlying sea-ice. Because the surface flux entirely feeds back to surface, this has significant implications for understanding and simulating the recent Arctic sea-ice loss. In addition, the mesoscale model approach proposed and evaluated in the dissertation will be an useful tool for climate scale studies on cloud especially when realistic climatologies are necessary.

References

- Arctic Climate Impact Assessment (2005). *Arctic Climate Impact Assessment: Scientific Report*, New York, NY: Cambridge University Press.
- Ba, M. B., Ellingson, R. G., & Gruber, A. (2003). Validation of a technique for estimating OLR with the GOES sounder. *Journal of Atmospheric and Oceanic Technology*, 79–89.
- Barton, N. P., & Veron, D. E. (2012). Response of clouds and surface energy fluxes to changes in sea-ice cover over the Laptev Sea (Arctic Ocean). *Climate Research*, 54, 69–84.
<https://doi.org/10.3354/cr01101>
- Bodas-Salcedo, A., Webb, M. J., Bony, S., Chepfer, H., Dufresne, J.-L., Klein, S. A., et al. (2011). COSP: Satellite simulation software for model assessment. *Bulletin of the American Meteorological Society*, 92, 1023–1043. <https://doi.org/10.1175/2011bams2856.1>
- Bony, S., Stevens, B., Frierson, D. M. W., Jakob, C., Kageyama, M., Pincus, R., et al. (2015). Clouds, circulation and climate sensitivity. *Nature Geoscience*, 8(4), 261–268. <https://doi.org/10.1038/ngeo2398>
- Boucher, O., Randall, D., Artaxo, P., Bretherton, C., Feingold, G., Forster, P., et al. (2014). Clouds and aerosols. In: Climate change 2013: The Physical Science Basis Contribution of Working Group I to the Fifth Assessment Report of the Intergovernmental Panel on Climate Change. Cambridge University.
- Bryan, G. H., & Morrison, H. (2012). Sensitivity of a simulated squall line to horizontal resolution and parameterization of microphysics. *Monthly Weather Review*, 140, 202–225.
<https://doi.org/10.1175/MWR-D-11-00046.1>
- Cesana, G., Kay, J. E., Chepfer, H., English, J. M., & Boer, G. (2012). Ubiquitous low-level liquid-containing Arctic clouds: New observations and climate model constraints from CALIPSO-GOCCP. *Geophysical Research Letters*, 39, L20804.
<https://doi.org/10.1029/2012GL053385>
- Cess, R. D., Zhang, M. H., Ingram, W. J., Potter, G. L., Alekseev, V., Barker, H. W., et al. (1996). Cloud feedback in atmospheric general circulation models: An update. *Journal of Geophysical Research: Atmospheres*, 101(D8), 12791–12794.
<https://doi.org/10.1029/96JD00822>

- Chan, M. A., & Comiso, J. C. (2011). Cloud features detected by MODIS but not by CloudSat and CALIOP. *Geophysical Research Letters*, 38, L24813. <https://doi.org/10.1029/2011GL050063>
- Chan, M. A., & Comiso, J. C. (2013). Arctic cloud characteristics as derived from MODIS, CALIPSO, and CloudSat. *Journal of Climate*, 26(10), 3285–3306. <https://doi.org/10.1175/JCLI-D-12-00204.1>
- Chang, F.-L., and J. A. Coakley (2007), Relationships between marine stratus cloud optical depth and temperature: Inferences from AVHRR observations. *J. Clim.*, 20, 2022–2036.
- Chepfer, H., Bony, S., Winker, D., Chiriaco, M., Dufresne, J.-L., & Sèze, G. (2008). Use of CALIPSO lidar observations to evaluate the cloudiness simulated by a climate model. *Geophysical Research Letters*, 35, L15704. <https://doi.org/10.1029/2008GL034207>
- Chernokulsky, A. V., & Mokhov, I. I. (2012). Climatology of total cloudiness in the Arctic: An intercomparison of observations and reanalyses. *Advances in Meteorology*, 2012, 542093. <https://doi.org/10.1155/2012/542093>
- Cho, H., Ho, C.-H., & Choi, Y.-S. (2012). The observed variation in cloud-induced longwave radiation in response to sea surface temperature over the Pacific warm pool from MTSAT-1R imagery. *Geophysical Research Letters*, 39(18). <https://doi.org/10.1029/2012GL052700>
- Cho, H., Jun, S., Ho, C., & McFarquhar, G. (2020). Simulations of Winter Arctic Clouds and Associated Radiation Fluxes Using Different Cloud Microphysics Schemes in the Polar WRF: Comparisons With CloudSat, CALIPSO, and CERES. *Journal of Geophysical Research: Atmospheres*, 125(2). <https://doi.org/10.1029/2019JD031413>
- Choi, Y.-S., & Ho, C.-H. (2009). Validation of cloud property retrievals from MTSAT-1R imagery using MODIS observations. *International Journal of Remote Sensing*, 30(22), 5935–5958. <https://doi.org/10.1080/01431160902791887>
- Choi, Y.-S., & Song, H.-J. (2012). On the numerical integration of a randomly forced system: variation and feedback estimation. *Theoretical and Applied Climatology*, 110(1–2), 97–101. <https://doi.org/10.1007/s00704-012-0612-3>
- Choi, Y.-S., Ho, C.-H., & Sui, C.-H. (2005). Different optical properties of high cloud in GMS and MODIS observations. *Geophysical Research Letters*, 32(23), 1–4. <https://doi.org/10.1029/2005GL024616>

- Choi, Y.-S., Lindzen, R. S., Ho, C.-H., & Kim, J. (2010). Space observations of cold-cloud phase change. *Proceedings of the National Academy of Sciences of the United States of America*, 107(25), 11211–11216. <https://doi.org/10.1073/pnas.1006241107>
- Choi, Y.-S., Cho, H., Ho, C.-H., Lindzen, R. S., Park, S. K., & Yu, X. (2014). Influence of non-feedback variations of radiation on the determination of climate feedback. *Theoretical and Applied Climatology*, 115(1–2), 355–364. <https://doi.org/10.1007/s00704-013-0998-6>
- Chou, M.-D., Suarez, M. J., Ho, C.-H., Yan, M. M.-H., & Lee, K.-T. (1998). Parameterizations for cloud overlapping and shortwave single-scattering properties for use in general circulation and cloud ensemble models. *Journal of Climate*, 11, 202–214. [https://doi.org/10.1175/1520-0442\(1998\)011<0202:PFCOAS>2.0.CO;2](https://doi.org/10.1175/1520-0442(1998)011<0202:PFCOAS>2.0.CO;2)
- Chung, E.-S., Soden, B. J., & Sohn, B.-J. (2010). Revisiting the determination of climate sensitivity from relationships between surface temperature and radiative fluxes. *Geophysical Research Letters*, 37(10). <https://doi.org/10.1029/2010GL043051>
- Cohen, J. (2016). An observational analysis: Tropical relative to Arctic influence on midlatitude weather in the era of Arctic amplification. *Geophysical Research Letters*, 43(10), 5287–5294. <https://doi.org/10.1002/2016GL069102>
- Cohen, J., Screen, J. a., Furtado, J. C., Barlow, M., Whittleston, D., Coumou, D., et al. (2014). Recent Arctic amplification and extreme mid-latitude weather. *Nature Geoscience*, 7(August), 627–637. <https://doi.org/10.1038/ngeo2234>
- Colman, R. (2003). A comparison of climate feedbacks in general circulation models. *Climate Dynamics*, 20, 865–873. <https://doi.org/10.1007/s00382-003-0310-z>
- Comiso, J. C. (2006). Abrupt decline in the Arctic winter sea ice cover. *Geophysical Research Letters*, 33, L18504. <https://doi.org/10.1029/2006GL027341>
- Comiso, J. C. (2012). Large decadal decline of the arctic multiyear ice cover. *Journal of Climate*, 25(4), 1176–1193. <https://doi.org/10.1175/JCLI-D-11-00113.1>
- Comiso, J. C., Parkinson, C. L., Gersten, R., & Stock, L. (2008). Accelerated decline in the Arctic sea ice cover. *Geophysical Research Letters*, 35(1), 1–6. <https://doi.org/10.1029/2007GL031972>

- Curry, J. A., Schramm, J. L., Rossow, W. B., & Randall, D. (1996). Overview of Arctic cloud and radiation characteristics. *Journal of Climate*, 9, 1731–1764. [https://doi.org/10.1175/1520-0442\(1996\)009<1731:OOACAR>2.0.CO;2](https://doi.org/10.1175/1520-0442(1996)009<1731:OOACAR>2.0.CO;2)
- Delanoë, J., & Hogan, R. J. (2008). A variational scheme for retrieving ice cloud properties from combined radar, lidar, and infrared radiometer. *Journal of Geophysical Research*, 113, D07204. <https://doi.org/10.1029/2007JD009000>
- Delanoë, J., & Hogan, R. J. (2010). Combined CloudSat-CALIPSO-MODIS retrievals of the properties of ice clouds. *Journal of Geophysical Research*, 115, D00H29. <https://doi.org/10.1029/2009JD012346>
- Dessler, A. E. (2011). Cloud variations and the Earth's energy budget. *Geophysical Research Letters*, 38(August), 10–12. <https://doi.org/10.1029/2011GL049236>
- Dessler, A. E., Mauritsen, T., & Stevens, B. (2018). The influence of internal variability on Earth's energy balance framework and implications for estimating climate sensitivity. *Atmospheric Chemistry and Physics*, 18(7), 5147–5155. <https://doi.org/10.5194/acp-18-5147-2018>
- Díaz, J. P., González, A., Expósito, F. J., Pérez, J. C., Fernández, J., García-Díez, M., & Taima, D. (2015). WRF multi-physics simulation of clouds in the African region. *Quarterly Journal of the Royal Meteorological Society*, 141(692), 2737–2749. <https://doi.org/10.1002/qj.2560>
- Driemel, A., Augustine, J., Behrens, K., Colle, S., Cox, C., Cuevas-Agulló, E., et al. (2018). Baseline Surface Radiation Network (BSRN): structure and data description (1992–2017). *Earth System Science Data*, 10, 1491–1501. <https://doi.org/10.5194/essd-10-1491-2018>
- Forster, P. M. F., & Gregory, J. M. (2006). The climate sensitivity and its components diagnosed from Earth radiation budget data. *Journal of Climate*, 19(1), 39–52. <https://doi.org/10.1175/JCLI3611.1>
- Francis, J. A., & Hunter, E. (2007). Drivers of declining sea ice in the Arctic winter: A tale of two seas. *Geophysical Research Letters*, 34, L17503. <https://doi.org/10.1029/2007GL030995>
- Frankignoul, C. (1999). A Cautionary Note on the Use of Statistical Atmospheric Models in the Middle Latitudes: Comments on “Decadal Variability in the North Pacific as Simulated by a Hybrid Coupled Model.” *Journal of Climate*, 1871–1872.

- Frankignoul, C., Czaja, A., & L'Heveder, B. (1998). Air–Sea Feedback in the North Atlantic and Surface Boundary Conditions for Ocean Models. *Journal of Climate*, 11(9), 2310–2324.
[https://doi.org/10.1175/1520-0442\(1998\)011<2310:ASFITN>2.0.CO;2](https://doi.org/10.1175/1520-0442(1998)011<2310:ASFITN>2.0.CO;2)
- Goosse, H., Kay, J. E., Armour, K. C., Bodas-Salcedo, A., Chepfer, H., Docquier, D., et al. (2018). Quantifying climate feedbacks in polar regions. *Nature Communications*, 9, 1919.
<https://doi.org/10.1038/s41467-018-04173-0>
- Graversen, R. G., Mauritsen, T., Tjernström, M., Källén, E., & Svensson, G. (2008). Vertical structure of recent Arctic warming. *Nature*, 451, 53–56. <https://doi.org/10.1038/nature06502>
- Gregory, J. M., & Webb, M. (2008). Tropospheric Adjustment Induces a Cloud Component in CO₂ Forcing. *Journal of Climate*, 21(1), 58–71. <https://doi.org/10.1175/2007JCLI1834.1>
- Gregory, J. M., Andrews, T., Good, P., Mauritsen, T., & Forster, P. M. (2016). Small global-mean cooling due to volcanic radiative forcing. *Climate Dynamics*, 47(12), 3979–3991.
<https://doi.org/10.1007/s00382-016-3055-1>
- Grell, G. A., & Dévényi, D. (2002). A generalized approach to parameterizing convection combining ensemble and data assimilation techniques. *Geophysical Research Letters*, 29(14).
<https://doi.org/10.1029/2002GL015311>
- Harrison, E. F., Minnis, P., Barkstrom, B. R., Ramanathan, V., Cess, R. D., & Gibson, G. G. (1990). Seasonal variation of cloud radiative forcing derived from the Earth Radiation Budget Experiment. *Journal of Geophysical Research*, 95(D11), 18687–18703.
<https://doi.org/10.1029/JD095iD11p18687>
- Hartmann, D. L., & Larson, K. (2002). An important constraint on tropical cloud-climate feedback. *Geophysical Research Letters*, 29(20), 10–13. <https://doi.org/10.1029/2002GL015835>
- Haynes, J. M., Marchand, R. T., Luo, Z., Bodas-Salcedo, A., & Stephens, G. L. (2007). A multipurpose radar simulation package: QuickBeam. *Bulletin of the American Meteorological Society*, 88(11), 1723–1728. <https://doi.org/10.1175/BAMS-88-11-1723>
- Hines, K. M., & Bromwich, D. H. (2017). Simulation of late summer Arctic clouds during ASCOS with Polar WRF. *Monthly Weather Review*, 145, 521–541. <https://doi.org/10.1175/MWR-D-16-0079.1>

- Hong, S.-Y., Dudhia, J., & Chen, S.-H. (2004). A revised approach to ice microphysical processes for the bulk parameterization of clouds and precipitation. *Monthly Weather Review*, 132, 103–120.
[https://doi.org/10.1175/1520-0493\(2004\)132<0103:ARATIM>2.0.CO;2](https://doi.org/10.1175/1520-0493(2004)132<0103:ARATIM>2.0.CO;2)
- Hong, S.-Y., & Lim, J.-O. J. (2006). The WRF single-moment 6-class microphysics scheme (WSM6). *Journal of the Korean Meteorological Society*, 42(2), 129–151.
- Horváth, Á., & Soden, B. J. (2008). Lagrangian Diagnostics of Tropical Deep Convection and Its Effect upon Upper-Tropospheric Humidity. *Journal of Climate*, 21(5), 1013–1028.
<https://doi.org/10.1175/2007JCLI1786.1>
- Intergovernmental Panel on Climate Change (2007) Climate Change 2007: The Physical Science Basis. Contribution of Working Group I to the Fourth Assessment Report of the Intergovernmental Panel on Climate Change. Cambridge Univ Press, Cambridge, U. K.
- Intergovernmental Panel on Climate Change (2013). Evaluation of Climate Models. In T. F. Stocker et al. (Eds.), *Climate Change 2013: The Physical Science Basis. Contribution of Working Group I to the Fifth Assessment Report of the Intergovernmental Panel on Climate Change* (pp. 741–866). Cambridge, UK, & New York, NY: Cambridge University Press. doi:10.1017/CBO9781107415324.020
- Janjić, Z. I. (1994). The step-mountain eta coordinate model: Further developments of the convection, viscous sublayer, and turbulence closure schemes. *Monthly Weather Review*, 122(5), 927–945.
[https://doi.org/10.1175/1520-0493\(1994\)122<0927:TSMECM>2.0.CO;2](https://doi.org/10.1175/1520-0493(1994)122<0927:TSMECM>2.0.CO;2)
- Jun, S.-Y., Ho, C.-H., Jeong, J.-H., Choi, Y.-S., & Kim, B.-M. (2016). Recent changes in winter Arctic clouds and their relationships with sea ice and atmospheric conditions. *Tellus A: Dynamic Meteorology and Oceanography*, 68, 29130.
<https://doi.org/10.3402/tellusa.v68.29130>
- Jung, T., Gulev, S. K., Rudeva, I., & Soloviov, V. (2006). Sensitivity of extratropical cyclone characteristics to horizontal resolution in the ECMWF model. *Quarterly Journal of the Royal Meteorological Society*, 132, 1839–1857. <https://doi.org/10.1256/qj.05.212>
- Karlsson, J., & Svensson, G. (2011). The simulation of Arctic clouds and their influence on the winter surface temperature in present-day climate in the CMIP3 multi-model dataset. *Climate Dynamics*, 36, 623–635. <https://doi.org/10.1007/s00382-010-0758-6>

- Karlsson, J., & Svensson, G. (2013). Consequences of poor representation of Arctic sea-ice albedo and cloud-radiation interactions in the CMIP5 model ensemble. *Geophysical Research Letters*, 40, 4374–4379. <https://doi.org/10.1002/grl.50768>
- Kay, J. E., L'Ecuyer, T., Chepfer, H., Loeb, N., Morrison, A., & Cesana, G. (2016). Recent advances in Arctic cloud and climate research. *Current Climate Change Reports*, 2, 159–169. <https://doi.org/10.1007/s40641-016-0051-9>
- Kim, B.-M., Son, S.-W., Min, S.-K., Jeong, J.-H., Kim, S.-J., Zhang, X., et al. (2014). Weakening of the stratospheric polar vortex by Arctic sea-ice loss. *Nature Communications*, 5(1), 4646. <https://doi.org/10.1038/ncomms5646>
- Kim, B.-M., Hong, J., Jun, S.-Y., Zhang, X., Kwon, H., Kim, S.-J., et al. (2017). Major cause of unprecedented Arctic warming in January 2016: Critical role of an Atlantic windstorm. *Scientific Reports*, 7, 40051. <https://doi.org/10.1038/srep40051>
- Kim, K.-Y., Kim, J.-Y., Kim, J., Yeo, S., Na, H., Hamlington, B. D., & Leben, R. R. (2019). Vertical Feedback Mechanism of Winter Arctic Amplification and Sea Ice Loss. *Scientific Reports*, 9(1), 1–10. <https://doi.org/10.1038/s41598-018-38109-x>
- Klaus, D., Dethloff, K., Dorn, W., Rinke, A., & Wu, D. L. (2016). New insight of Arctic cloud parameterization from regional climate model simulations, satellite-based, and drifting station data. *Geophysical Research Letters*, 43, 5450–5459. <https://doi.org/10.1002/2015GL067530>
- Kratz, D. P., Gupta, S. K., Wilber, A. C., & Sothcott, V. E. (2010). Validation of the CERES Edition 2B surface-only flux algorithms. *Journal of Applied Meteorology and Climatology*, 49, 164–180. <https://doi.org/10.1175/2009JAMC2246.1>
- Kug, J.-S., Jeong, J.-H., Jang, Y.-S., Kim, B.-M., Folland, C. K., Min, S.-K., & Son, S.-W. (2015). Two distinct influences of Arctic warming on cold winters over North America and East Asia. *Nature Geoscience*, 8, 759–762. <https://doi.org/10.1038/ngeo2517>
- Lewis, N., & Curry, J. a. (2015). The implications for climate sensitivity of AR5 forcing and heat uptake estimates. *Climate Dynamics*, 45(3–4), 1009–1023. <https://doi.org/10.1007/s00382-014-2342-y>
- Lin, B., Wielicki, B., Chambers, L. H., Hu, Y., & Xu, K.-M. (2002). The iris hypothesis: A negative or positive cloud feedback? *Journal of Climate*, 15, 3–7.

- Lin, B., Min, Q., Sun, W., Hu, Y., & Fan, T. (2011). Can climate sensitivity be estimated from short-term relationships of top-of-atmosphere net radiation and surface temperature? *Journal of Quantitative Spectroscopy and Radiative Transfer*, 112(2), 177–181.
<https://doi.org/10.1016/j.jqsrt.2010.03.012>
- Lindzen, R. S., Chou, M.-D., & Hou, A. Y. (2001). Does the Earth Have an Adaptive Infrared Iris? *Bulletin of the American Meteorological Society*, 82(3), 417–432. [https://doi.org/10.1175/1520-0477\(2001\)082<0417:DTEHAA>2.3.CO;2](https://doi.org/10.1175/1520-0477(2001)082<0417:DTEHAA>2.3.CO;2)
- Lindzen, R. S., & Choi, Y.-S. (2009). On the determination of climate feedbacks from ERBE data. *Geophysical Research Letters*, 36(16), 1–6. <https://doi.org/10.1029/2009GL039628>
- Lindzen, R. S., & Choi, Y.-S. (2011). On the observational determination of climate sensitivity and its implications. *Asia-Pacific Journal of Atmospheric Sciences*, 47(4), 377–390.
<https://doi.org/10.1007/s13143-011-0023-x>
- Listowski, C., & Lachlan-Cope, T. (2017). The microphysics of clouds over the Antarctic Peninsula - Part 2: Modelling aspects within Polar WRF. *Atmospheric Chemistry and Physics*, 17(17), 10195–10221.
<https://doi.org/10.5194/acp-17-10195-2017>
- Liu, Y., Key, J. R., Francis, J. A., & Wang, X. (2007). Possible causes of decreasing cloud cover in the Arctic winter, 1982–2000. *Geophysical Research Letters*, 34, L14705.
<https://doi.org/10.1029/2007GL030042>
- Liu, Y., Key, J. R., Ackerman, S. a., Mace, G. G., & Zhang, Q. (2012). Arctic cloud macrophysical characteristics from CloudSat and CALIPSO. *Remote Sensing of Environment*, 124, 159–173.
<https://doi.org/10.1016/j.rse.2012.05.006>
- Manabe, S., Bryan, K., & Spelman, M. J. (1990). Transient Response of a Global Ocean-Atmosphere Model to a Doubling of Atmospheric Carbon Dioxide. *Journal of Physical Oceanography*, 20(5), 722–749. [https://doi.org/10.1175/1520-0485\(1990\)020<0722:TROAGO>2.0.CO;2](https://doi.org/10.1175/1520-0485(1990)020<0722:TROAGO>2.0.CO;2)
- McCarthy, M., Spillane, S., Walsh, S., & Kendon, M. (2016). The meteorology of the exceptional winter of 2015/2016 across the UK and Ireland. *Weather*, 71(12), 305–313.
<https://doi.org/10.1002/wea.2823>
- McFarquhar, G. M., Zhang, G., Poellot, M. R., Kok, G. L., McCoy, R., Tooman, T., et al. (2007). Ice properties of single-layer stratocumulus during the Mixed-Phase Arctic Cloud Experiment: 1.

- Observations. *Journal of Geophysical Research*, 112, D24201.
<https://doi.org/10.1029/2007JD008633>
- Mlawer, E. J., Taubman, S. J., Brown, P. D., Iacono, M. J., & Clough, S. A. (1997). Radiative transfer for inhomogeneous atmospheres: RRTM, a validated correlated-k model for the longwave. *Journal of Geophysical Research: Atmospheres*, 102(D14), 16663–16682.
<https://doi.org/10.1029/97JD00237>
- Morrison, H., Curry, J. A., & Khvorostyanov, V. I. (2005). A new double-moment microphysics parameterization for application in cloud and climate models. Part I: Description. *Journal of the Atmospheric Sciences*, 62, 1665–1677. <https://doi.org/10.1175/JAS3446.1>
- Morrison, H., Shupe, M. D., & Curry, J. A. (2003). Modeling clouds observed at SHEBA using a bulk microphysics parameterization implemented into a single-column model. *Journal of Geophysical Research*, 108(D8), 4255. <https://doi.org/10.1029/2002JD002229>
- Murphy, D. M. (2010). Constraining climate sensitivity with linear fits to outgoing radiation. *Geophysical Research Letters*, 37(9), 1–5.
<https://doi.org/10.1029/2010GL042911>
- NCEP (2000). NCEP FNL Operational model global tropospheric analyses, continuing from July 1999. Research Data Archive at the National Center for Atmospheric Research, Computational and Information Systems Laboratory, Boulder, CO,
<https://doi.org/10.5065/D6M043C6>
- Ohring, G., Gruber, A., & Ellingson, R. G. (1984). Satellite determinations of the relationship between total longwave radiation flux and infrared window radiance. *Journal of Climate and Applied Meteorology*, 23, 416–425.
- Ohring, G., Wielicki, B., Spencer, R., Emery, B., & Datla, R. (2005). Satellite Instrument Calibration for Measuring Global Climate Change: Report of a Workshop. *Bulletin of the American Meteorological Society*, 86(9), 1303–1314.
<https://doi.org/10.1175/BAMS-86-9-1303>
- Oreopoulos, L., Cho, N., & Lee, D. (2017). New insights about cloud vertical structure from CloudSat and CALIPSO observations. *Journal of Geophysical Research: Atmospheres*, 122, 9280–9300.
<https://doi.org/10.1002/2017JD026629>
- Overland, J. E., Dethloff, K., Francis, J. A., Hall, R. J., Hanna, E., Kim, S.-J., et al. (2016). Nonlinear response of mid-latitude weather to the changing Arctic. *Nature Climate Change*, 6, 992–999.
<https://doi.org/10.1038/nclimate3121>

- Park, D.-S. R., Lee, S., & Feldstein, S. B. (2015). Attribution of the recent winter sea ice decline over the Atlantic sector of the Arctic Ocean. *Journal of Climate*, 28, 4027–4033. <https://doi.org/10.1175/JCLI-D-15-0042.1>
- Park, M., Ho, C., Cho, H., & Choi, Y. (2015). Retrieval of outgoing longwave radiation from COMS narrowband infrared imagery. *Advances in Atmospheric Sciences*, 32(3), 375–388. <https://doi.org/10.1007/s00376-014-4013-7>
- Pinto, J. O. (1998). Autumnal mixed-phase cloudy boundary layers in the Arctic. *Journal of the Atmospheric Sciences*, 55, 2016–2038. [https://doi.org/10.1175/1520-0469\(1998\)055<2016:AMPCBL>2.0.CO;2](https://doi.org/10.1175/1520-0469(1998)055<2016:AMPCBL>2.0.CO;2)
- Pope, V. D., & Stratton, R. A. (2002). The processes governing horizontal resolution sensitivity in a climate model. *Climate Dynamics*, 19, 211–236. <https://doi.org/10.1007/s00382-001-0222-8>
- Ramanathan, V., & Collins, W. (1991). Thermodynamic regulation of ocean warming by cirrus clouds deduced from observations of the 1987 El Niño. *Nature*. 351, 27–32.
- Rapp, A. D., Kummerow, C., Berg, W., & Griffith, B. (2005). An Evaluation of the Proposed Mechanism of the Adaptive Infrared Iris Hypothesis Using TRMM VIRS and PR Measurements. *Journal of Climate*, 18(20), 4185–4194. <https://doi.org/10.1175/JCLI3528.1>
- Reynolds, R., Smith, T., Liu, C., Chelton, D. B., Casey, K. S., & Schlax, M. G. (2007). Daily high-resolution-blended analyses for sea surface temperature. *Journal of Climate*, 20(22), 5473–5496. <https://doi.org/10.1175/2007JCLI1824.1>
- Ricchiazzi, P., Yang, S., Gautier, C., & Sowle, D. (1998). SBDART: A Research and Teaching Software Tool for Plane-Parallel Radiative Transfer in the Earth's Atmosphere. *Bulletin of the American Meteorological Society*, 79(10), 2101–2114. [https://doi.org/10.1175/1520-0477\(1998\)079<2101:SARATS>2.0.CO;2](https://doi.org/10.1175/1520-0477(1998)079<2101:SARATS>2.0.CO;2)
- Roe, G. H., & Baker, M. B. (2007). Why is climate sensitivity so unpredictable? *Science*, 318(5850), 629–32. <https://doi.org/10.1126/science.1144735>
- Roe, G. H., Feldl, N., Armour, K. C., Hwang, Y.-T., & Frierson, D. M. W. (2015). The remote impacts of climate feedbacks on regional climate predictability. *Nature Geoscience*. <https://doi.org/10.1038/ngeo2346>

- Rondanelli, R., & Lindzen, R. S. (2008). Observed variations in convective precipitation fraction and stratiform area with sea surface temperature. *Journal of Geophysical Research*, 113(D16), 1–17. <https://doi.org/10.1029/2008JD010064>
- Rossow, W. B., & Garder, L. C. (1993). Cloud Detection Using Satellite Measurements of Infrared and Visible Radiances for ISCCP. *Journal of Climate*, 6(12), 2341–2369. [https://doi.org/10.1175/1520-0442\(1993\)006<2341:CDUSMO>2.0.CO;2](https://doi.org/10.1175/1520-0442(1993)006<2341:CDUSMO>2.0.CO;2)
- Schwartz, S. E. (2007). Heat capacity, time constant, and sensitivity of Earth's climate system. *Journal of Geophysical Research*, 112(D24), 1–12. <https://doi.org/10.1029/2007JD008746>
- Serreze, M. C., & Barry, R. G. (2011). Processes and impacts of Arctic amplification: A research synthesis. *Global and Planetary Change*, 77(1–2), 85–96. <https://doi.org/10.1016/j.gloplacha.2011.03.004>
- Serreze, M. C., Barrett, A. P., Stroeve, J. C., Kindig, D. N., & Holland, M. M. (2009). The emergence of surface-based Arctic amplification. *The Cryosphere*, 3(1), 11–19. <https://doi.org/10.5194/tc-3-11-2009>
- Sherwood, S. C., Bony, S., & Dufresne, J.-L. (2014). Spread in model climate sensitivity traced to atmospheric convective mixing. *Nature*, 505(7481), 37–42. <https://doi.org/10.1038/nature12829>
- Shupe, M. D., Matrosov, S. Y., & Uttal, T. (2006). Arctic mixed-phase cloud properties derived from surface-based sensors at SHEBA. *Journal of the Atmospheric Sciences*, 63, 697–711. <https://doi.org/10.1175/JAS3659.1>
- Skamarock, W. C., Klemp, J. B., Dudhia, J., Gill, D. O., Barker, D. M., Duda, M. G., et al. (2008). A Description of the Advanced Research WRF Version 3. In *NCAR Technical Note* (NCAR/TN-4751STR, pp. 113). <http://dx.doi.org/10.5065/D68S4MVH>
- Smith, R. J. (2009). Use and misuse of the reduced major axis for line-fitting. *American Journal of Physical Anthropology*, 140(3), 476–486. <https://doi.org/10.1002/ajpa.21090>
- Soden, B. J., & Held, I. M. (2006). An assessment of climate feedbacks in coupled ocean–atmosphere models. *Journal of Climate*, 19, 3354–3360. <https://doi.org/10.1175/JCLI3799.1>
- Spencer, R. W., & Braswell, W. D. (2008). Potential Biases in Feedback Diagnosis from Observational Data: A Simple Model Demonstration. *Journal of Climate*, 21(21), 5624–5628. <https://doi.org/10.1175/2008JCLI2253.1>

- Spencer, R. W., & Braswell, W. D. (2010). On the diagnosis of radiative feedback in the presence of unknown radiative forcing. *Journal of Geophysical Research*, 115(D16), 1–13.
<https://doi.org/10.1029/2009JD013371>
- Spencer, R. W., & Braswell, W. D. (2011). On the Misdiagnosis of Surface Temperature Feedbacks from Variations in Earth's Radiant Energy Balance. *Remote Sensing*, 3(8), 1603–1613.
<https://doi.org/10.3390/rs3081603>
- Stephens, G. L. (2005). Cloud Feedbacks in the Climate System: A Critical Review. *Journal of Climate*, 18(2), 237–273.
<https://doi.org/10.1175/JCLI-3243.1>
- Stephens, G. L., Vane, D. G., Boain, R. J., Mace, G. G., Sassen, K., Wang, Z., et al. (2002). The CloudSat mission and the A-Train: A new dimension of space-based observations of clouds and precipitation. *Bulletin of the American Meteorological Society*, 83, 1771–1790.
<https://doi.org/10.1175/BAMS-83-12-1771>
- Tewari, M., Chen, F., Wang, W., Dudhia, J., LeMone, M. A., Mitchell, K., et al. (2004). *Implementation and verification of the unified Noah land-surface model in the WRF model*. Paper presented in 20th Conference on Weather Analysis and Forecasting/16th Conference on Numerical Weather Prediction, American Meteorological Society, Seattle, WA.
- Thiébaux, J., Rogers, E., Wang, W., & Katz, B. (2003). A new high-resolution blended real-time global sea surface temperature analysis. *Bulletin of the American Meteorological Society*, 84(5), 645–656.
<https://doi.org/10.1175/BAMS-84-5-645>
- Trenberth, K. E., Fasullo, J. T., O'Dell, C., & Wong, T. (2010). Relationships between tropical sea surface temperature and top-of-atmosphere radiation. *Geophysical Research Letters*, 37(3), 1–5.
<https://doi.org/10.1029/2009GL042314>
- Van Weverberg, K., Vogelmann, A. M., Lin, W., Luke, E. P., Cialella, A., Minnis, P., et al. (2013). The role of cloud microphysics parameterization in the simulation of mesoscale convective system clouds and precipitation in the tropical western Pacific. *Journal of the Atmospheric Sciences*, 70, 1104–1128.
<https://doi.org/10.1175/JAS-D-12-0104.1>
- Webb, M. J., Senior, C. A., Sexton, D. M. H., Ingram, W. J., Williams, K. D., Ringer, M. A., et al. (2006). On the contribution of local feedback mechanisms to the range of climate sensitivity in two

- GCM ensembles. *Climate Dynamics*, 27, 17–38.
<https://doi.org/10.1007/s00382-006-0111-2>
- Wielicki, B. A., Barkstrom, B. R., Harrison, E. F., Lee, R. B., Louis Smith, G., & Cooper, J. E. (1996). Clouds and the Earth's Radiant Energy System (CERES): An Earth Observing System experiment. *Bulletin of the American Meteorological Society*, 77, 853–868.
[https://doi.org/10.1175/1520-0477\(1996\)077<0853:CATERE>2.0.CO;2](https://doi.org/10.1175/1520-0477(1996)077<0853:CATERE>2.0.CO;2)
- Wilson, A. B., Bromwich, D. H., & Hines, K. M. (2012). Evaluation of Polar WRF forecasts on the Arctic System Reanalysis domain: 2. Atmospheric hydrologic cycle. *Journal of Geophysical Research: Atmospheres*, 117, D04107. <https://doi.org/10.1029/2011JD016765>
- Winker, D. M., Vaughan, M. A., Omar, A., Hu, Y., Powell, K. A., Liu, Z., et al. (2009). Overview of the CALIPSO mission and CALIOP data processing algorithms. *Journal of Atmospheric and Oceanic Technology*, 26, 2310–2323.
<https://doi.org/10.1175/2009JTECHA1281.1>
- Zelinka, M. D., & Hartmann, D. L. (2010). Why is longwave cloud feedback positive? *Journal of Geophysical Research*, 115(D16), 1–16. <https://doi.org/10.1029/2010JD013817>
- Zhang, C. (1993). Large-Scale Variability of Atmospheric Deep Convection in Relation to Sea Surface Temperature in the Tropics. *Journal of Climate*, 6(10), 1898–1913. [https://doi.org/10.1175/1520-0442\(1993\)006<1898:LSVODA>2.0.CO;2](https://doi.org/10.1175/1520-0442(1993)006<1898:LSVODA>2.0.CO;2)
- Zhang, G. J., Ramanathan, V., & McPhaden, M. J. (1995). Convection-Evaporation Feedback in the Equatorial pacific. *Journal of Climate*, 8(12), 3040–3051. [https://doi.org/10.1175/1520-0442\(1995\)008<3040:CEFITE>2.0.CO;2](https://doi.org/10.1175/1520-0442(1995)008<3040:CEFITE>2.0.CO;2)

국문 초록

구름은 대기 상부와 지구 표면에서의 복사량을 조절하여 지구의 온도를 크게 변화시킬 수 있다. 지구가 온난화를 겪는 과정에서 구름이 어떤 식으로 변화하고 있는지를 아는 것은 미래 기후 예측에 매우 중요하지만, 관측 자료 및 수치 모델링을 통해 이를 파악하기에는 어려움이 있다. 구름 되먹임으로 일컬어지는 이 물리 과정은 관측 자료를 통해 그것의 정량적 규모를 판단하기가 쉽지 않다. 이 학위 논문에서는 대기 상부 복사량의 위성 관측 자료를 이용하여 이러한 되먹임 작용의 규모를 추정할 수 있는지를 살펴보았다. 되먹임 지수는 지구 평균 기온의 변화에 대한 대기 상부 복사량의 반응으로 정의되는데, 대기 상부 복사량의 시간적 변화 속에는 이러한 되먹임 작용으로 인한 반응 뿐 아니라 잡음 역시 포함되어 있다. 다양한 조건에서의 개념 모델 실험 결과, 복사량 시계열에서의 잡음 비율이 표준편차 기준으로 약 5% 미만이라면 시계열 분석을 통한 되먹임 지수의 정량 추정이 가능하다고 여겨진다. 하지만 위성 관측에서 나타난 전지구 평균 대기 상부 복사량의 시계열에서 잡음 비율은 약 13%를 상회하는 것으로 드러났다. 반면 전지구 평균이 아니라 북위 20도와 남위 20도 사이의 열대

지역의 복사량, 특히 지구가 방출하는 장파복사량의 시계열을 사용하는 경우에는 되먹임값 정량 추정의 가능성을 보였으며 그 값은 $3.9 \text{ W m}^{-2} \text{ K}^{-1}$ 으로 추정되었다. 이는 대기의 연직 대류 활동이 매우 활발한 열대 지역에서는 해수면 온도의 변화가 구름 및 수증기의 변화를 유도하여 해당 지역에서의 복사량 반응을 끌어낼 수 있음을 의미한다. 또한 태양광의 반사에 해당하는 단파복사에 비해 지구가 방출하는 장파복사의 경우, 되먹임 작용의 신호 대 잡음비가 커서 복사 되먹임 작용의 정량 추정 가능성이 높음을 의미한다. 이러한 이해를 바탕으로, 구름의 장파복사 되먹임을 정량 진단할 수 있을 것으로 기대되는 두 가지 지역 기후를 대상으로 연구를 진행하였다. 첫 번째는 열대 서태평양(20°N – 20°S , 130°E – 170°W)으로, 구름이 해수면 온도의 변화에 가장 민감한 것으로 알려진 지역이다. 두 번째는 겨울철의 북극해 지역인데, 이때는 태양 광이 존재하지 않는 극야 기간이므로 구름의 복사 효과가 장파복사 효과 만을 가질 수 있다. 열대 서태평양의 구름 장파복사 되먹임을 진단하기 위해 정지궤도위성의 관측자료를 이용하였는데, 정지궤도위성은 높은 시간 및 공간 분해능의 관측을 제공하므로 열대 지역 대기의 대류 활동을 관측하기에 적합하다. 결과적으로 이 지역 구름의 장파복사 되먹임 지수는 $15.72 \text{ W m}^{-2} \text{ K}^{-1}$ 으로 추정되었

는데, 이는 해수면 온도가 증가/감소할 때 구름을 통한 장파복사 방출이 큰 폭으로 증가/감소되어 본래의 온도 평형 상태를 빠르게 회복하려는 효과가 존재함을 의미한다. 이러한 효과는 해수면 온도가 증가할 때 구름의 수평 면적이 감소하고, 해수면 온도가 감소할 때 구름의 수평 면적이 증가하는 과정을 통해 ($-14.4\% \text{ K}^{-1}$) 이루어지고 있음을 확인할 수 있었다.

최근 북극 및 주변 지역의 겨울철 운량은 증가하는 추세인데 지난 몇 세기 동안의 북극해 해빙 감소가 이에 영향을 끼쳤을 수 있다. 만약 그렇다면, 증가한 운량은 지면으로의 장파복사를 강하게 하여 해빙을 더욱 감소시키는 양의 되먹임 효과를 가진다. 그러나 해빙 면적 뿐 아니라 해수면 온도 및 대기 순환의 변화 역시 운량에 영향을 줄 수 있으므로, 해빙의 변화가 구름에 끼치는 영향 만을 분리하기 위해서는 수치 모델 실험이 필요하다. 이 학위 연구에서는 보다 현실에 가까운 구름을 모의하기 위해 중규모 모델을 이용하였고, 위성 구름 관측과의 비교를 통해 이 모델이 북극의 겨울철 구름을 잘 모의하고 있는지를 우선 검증하였다. 다른 모든 조건을 동일하게 하고 해빙 면적 만을 감소시켰을 때, 북극해의 운량 및 구름의 질량은 해빙이 줄어든 영역을 중심으로 증가하였는데, 재분석 자료에서 나타난 지난 40년 간의 구름 변화와 유사

성을 보이고 있어서, 이 변화의 많은 부분을 해빙 감소로 설명할 수 있음을 시사한다. 특히 30% 이상의 겨울철 해빙 감소를 보이는 바렌츠해의 경우, 구름의 질량이 15%, 지구표면 하향 복사량이 10 W m^{-2} 증가하는 실험 결과를 보임으로써 최근 수 세기 동안의 북극해 지역의 겨울철 운량 증가에 해빙의 변화가 결정적 역할을 하였음을, 또한 구름의 되먹임 작용이 해빙 변화의 중요한 요소임을 알 수 있다.

이 학위 연구는 관측을 통해 지구 규모의 구름 되먹임 작용을 진단할 때 생기는 불확실성의 원인을 밝히는 동시에 지역 규모에서 구름 장파복사 되먹임 작용의 진단 가능성을 시사한다. 결과적으로 구름은 장파복사 효과를 통해 열대 지역의 온난화를 완화하고, 겨울철 북극해 지역의 온난화를 강화하고 있음이 밝혀졌다. 구름 되먹임 작용에 대한 이러한 이해가 미래 기후의 변화 양상을 예측하는데 도움을 줄 것으로 기대한다.